ELECTRONIC STRUCTURE STUDIES OF THE SI(100) SURFACE AND CO_2 INTERACTING WITH TIO_2 SURFACE CLUSTER MODELS

by

Wendy Marie Lampart

B. S. Chemistry, University of Pittsburgh, 2003

Submitted to the Graduate Faculty of the

Kenneth P. Dietrich School of Arts and Sciences in partial fulfillment

of the requirements for the degree of

Doctor of Philosophy

University of Pittsburgh

2014

UNIVERSITY OF PITTSBURGH

DIETRICH SCHOOL OF ARTS AND SCIENCES

This dissertation was presented

by

Wendy Marie Lampart

It was defended on

April 11, 2014

and approved by

Prof. J. Karl Johnson, William Kepler Whiteford Professor, Department of Chemical and Petroleum Engineering

Prof. Geoffrey Hutchison, Assistant Professor, Department of Chemistry

Prof. Daniel S. Lambrecht, Assistant Professor, Department of Chemistry

Dissertation Advisor: Kenneth Jordan, Distinguished Professor of Computational Chemistry, Department of Chemistry

.

ELECTRONIC STRUCTURE STUDIES OF THE SI(100) SURFACE AND CO2 INTERACTING WITH TIO2 SURFACE CLUSTER MODELS

Wendy Marie Lampart, PhD

University of Pittsburgh, 2014

This thesis focuses on testing models and methods for studying the interaction between titanium dioxide and CO_2, the structure of the Si(100) surface, and the effect of partial hydrogen passivation on the structure of bare dimers on the Si(100) surface.

Section one explores the applicability of multiple approximations to the Schrödinger equation and uses minimalistic models to determine which levels of theory and models are appropriate for capturing the structure of the surface. The Si(100) is the most important surface for semiconductor devices. It has a complex electronic structure with a small energy barrier between the ground state and two nearby local minima. Levels of theory that do not adequately include static electron correlation, find the incorrect ground state, while theories that neglect

electron correlation or only include dynamic electron correlation, give an artificially high favorability to the ground state.

It is also important to determine what size models capture enough to the surface to replicate its correct characteristics. High order electronic structure methods necessary for capturing the physics of the surface can only be done on small models.

As electronic devices become smaller, an atomic level understanding is increasingly. Fabrication of electronic devices involves passivating the surface with hydrogen. The work done in this thesis uses density functional theory to explore the effect adsorbed hydrogen has on the surface structure of Si(100)

Increased atmospheric levels in greenhouse gases, such as CO_2, are putting a continued strain on our climate. Levels of CO_2 are 40% higher than they were during preindustrial times. To mitigate the effects of climate change we must make a sustained effort to limit CO_2 levels in the atmosphere. Photocatalytic reduction of CO_2 on TiO_2 surfaces to form renewable carbon feedstocks, harnesses solar energy and reduces the consumption of fuels. To design TiO_2 catalysts we need a thorough understanding of interactions between CO_2 and the surface. This work uses electron structure theory to study the interaction between CO_2 and cluster models of anatase and rutile titanium dioxide, to assess which methods are suitable for studying this interaction and to understand the interaction itself.

TABLE OF CONTENTS

List of Tables

List of Figures

Preface

I would like thank my advisor, Dr. Ken Jordan, for his guidance, wisdom, patience, advice, and puns. With Ken as my advisor, I have had a learning, life, and research experience that I cherish.

I would like to thank the Jordan Group: Eric, Togo, Kaye, Vamsee, Mike, Tijo, Anshuman, Zach, Sefa, Meysam, Ozan, and Xun; for making me laugh and sharing their knowledge and time.

I would like to thank my family and friends for their endless support, their constant belief in me, and their love.

1. CHAPTER ONE: Introduction to Surfaces

1.1 Introduction to Surfaces

Surfaces provide the interface on which many chemical and physical processes occur. The interface is a key element in a solid's interaction with the outside world. That being said, surfaces have different properties than the bulk. When a bulk substrate is "cut" creating a surface, physical changes occur in the top surface layers. A frequently occurring change is the relaxation of the surface, where the first several layers of the surface contract closer to the bulk.[3-4] Their interlayer spacing reduces, while these surface atoms retain the translational periodicity of the bulk. A surface atom feels forces asymmetrically, like an atom in a diatomic molecule. The bond a surface atom forms is similar to that of an atom in the bulk solid (feeling forces more evenly) and to that of an atom in a diatomic molecule (feeling forces from only one side), with a bond length somewhat in between the two systems.[3-4]

Another commonly occurring surface phenomenon is reconstruction, where the atoms in the top surface layers change registry from that of the bulk.[3-4] Reconstruction usually occurs in covalent and ionic solids,[4] and often driving force is the reduction in the number of dangling bonds. Creating surfaces by cleaving the top layers from the bulk can break valance bonds, forming dangling bonds, db, that is unsaturated valance "bonds" in space.[3] These db are a highly

reactive and highly energetic state. Reconstruction eliminates dangling bonds, moving the surface to an energetically more favorable state.[3-4]

There are two common types of surface reconstructions. The first type is exhibited by GaAs(110). In the GaAs (110) surface, a dangling bond is eliminated via an electron transfer from Gallium to Arsenic, driving a surface rotation.[3-4] That is, the surface changes registry from the bulk but retains the same type of translational symmetry.[3-4] The other common type of surface reconstruction occurs on the Si(100) surface. In these surfaces, atoms lower their energy by bonding or grouping with each other in rows and clusters alternately spaced with distances larger and smaller than in the bulk.

1.2 The Si(100) Surface and Dimer formation

The primary reconstruction of the Si(100) surface, occurs when two neighboring atoms, each with two dangling bonds, form a dimer, eliminating a dangling bond on each atom. These dimers form rows on the Si(100) surface as shown in Figure 1. The distance between two atoms in the same dimer is ~2.35 Å. The distance between the two adjacent dimer rows is greater than 5Å for the c(4x2) structure.

Bulk silicon has a tetravalent diamond type lattice.[4-5] As previously mentioned, cleaving bulk silicon along the 100 plane severs two bonds on each surface silicon atom, creating two dangling bonds. This high energy, highly reactive surface state reconstructs to form parallel rows of Si dimers. The dimers form a surface superstructure on the bulk.[4, 6] This dimerization eliminates one of the dangling bonds on each atom, leaving only one highly energetic and highly reactive dangling bond on each atom.[4, 6]

The silicon dimers form a weak π and π* bonding between the two atoms. There is a small gap between the π and π* bonds, giving the dimer its biradical nature. Much of The chemistry and behavior of the Si(100) surface is controlled by dangling bonds, dimer-dimer interactions[7], and electron correlation.[8]

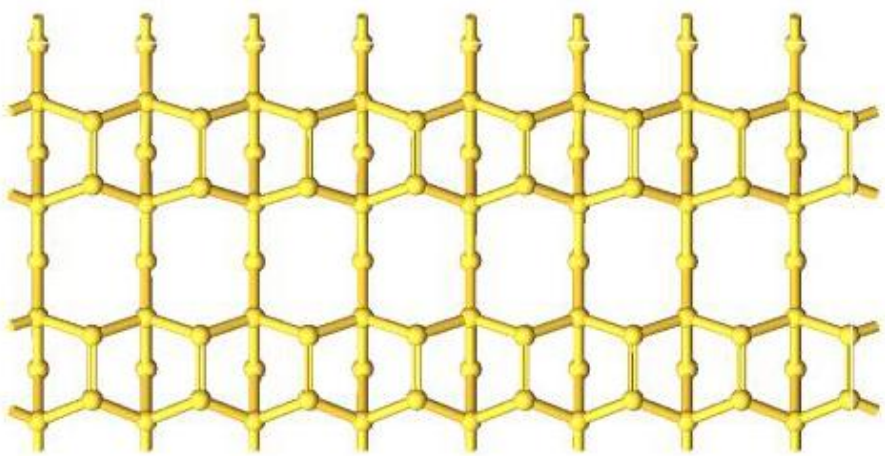

Figure 1: The top two layers of a Si(100) surface, showing the reconstruction of rows of dimers in the top layer.

1.3 Secondary Reconstructions: c(4x2), p(2x1), p(2x2)

The dimer reconstruction eliminates one dangling bond from each atom, leaving one remaining dangling bond per atom. The surface further lowers its energy by undergoing a secondary reconstruction when dimers align in c(4x2), p(2x2) or p(2x1) patterns as shown in Figure 2

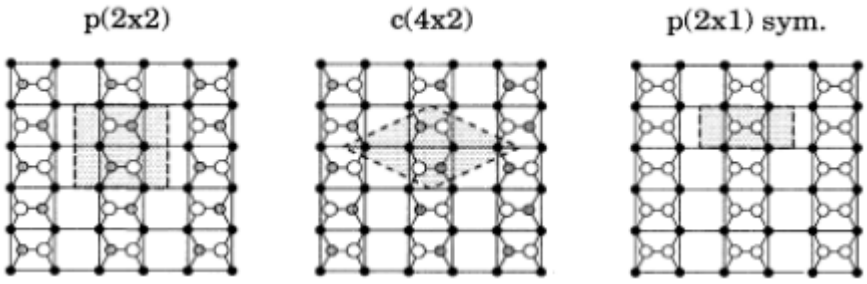

Figure 2: Top view of the p(2x2), the c(4x2) buckled and the symmetric (2x1) Si(100) surface. The top layer of dimers is the largest with white circles representing Silicon atoms higher than the lower grey colored silicon atoms. The small dark circles represent atoms in the layer below; the remaining layers are not shown. The dark shaded parallelograms represent the surface unit cell (Figure from ref 9).

1.4 The Importance of Understanding Si(100)

There are multiple reasons to study the Si(100) surface. For one it is a useful model to improve our understanding of covalently bonded systems and reactions on covalently bonded and semiconductor surfaces. A second reason is the frequently use of Si(100) in common electronic devices, including: computers, electronic scanners at stores, signal transmitters and receivers in cell phone communication, and others. Improving our understanding of this surface will bring insights into making more controlled, specialized and energy efficient devices.

Some of the recent work on the Si(100) surface, has focused on the interaction between the surface and aromatic hydrocarbon in an effort to move towards molecular control of electronic devices.[10] Other work has looked at multi-reference methods to study the Si(100) for larger systems,[11] as it is believed that the Si(100) will play a role in future nano-electronics and as a support structure for organic functionalization.[12-13] While other recent work, similar to ours,

looked at the role higher order electron correlation effects play in the surface structure and the suitability of various methods for studying it.[14]

1.5 The Importance of Understanding Hydrogen Adsorbed on Silicon Surfaces

The use of Si(100) in electronic devices, leads to the importance of the H/Si(100) system. A crucial step in the manufacture of electronic devices involves passivation of the highly reactive dangling bonds, which is often done using hydrogen.[5] When hydrogen binds to the surface, it eliminates the remaining dangling bond on that atom. Since the addition and removal of hydrogen has technological importance, it important to understand the effect hydrogen has on the silicon surface. Hydrogen is also used to control the morphology of silicon during low temperature epitaxy.[15] This leads to the motivation for our current work. That is, can we use DFT with PBC to understand the interplay between hydrogen and silicon to give insight into the extent H influences the surface morphology? Also as previous mentioned, functionalizing the silicon surface is important for working towards molecular control of electronic devices; can we gain insight from the simple adsorbate, hydrogen, on the surface and apply this to understanding other adsorbents?

Below are configurations on hydrogen on the Si(100) that were used in this work. Figure 3 shows a 2H*Si(100) monohydride structure with both hydrogen atoms adsorbed on the same dimer, while Figure 4 shows four different configurations of hydrogen atoms on the surface.

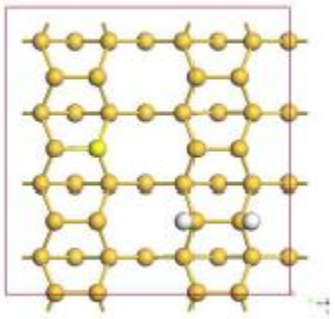

Figure 3: Top view of a 2H*Si(100) monohydride structure with both hydrogen atoms adsorbed on the same dimer. This picture shows three layers of silicon.

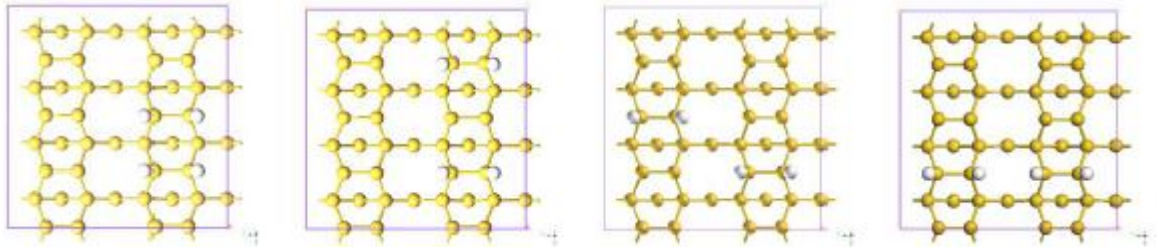

Figure 4: The four different adsorbate configurations of hydrogen on the silicon surface in a periodic cell. Clockwise from top left, four hydrogen atoms on neighboring dimers in the same row, four hydrogen atoms in the same row on alternating dimers, four hydrogen atoms on neighboring dimers in different rows, and in the bottom left four H atoms in opposite rows on next nearest neighbor dimers.

1.6 Introduction to Titanium Dioxide

Titanium dioxide is a wide band gap semiconductor. It occurs in three common forms: rutile, anatase and brookite. The anatase and brookite forms are metastable and convert to rutile upon heating to between 550 and 1000^{o}C[16]. While the rutile form is most stable, the anatase structure is more photoactive.[17] Titanium dioxide has several commercial applications, including use as a pigment in cosmetics, food, and paints; use in sunscreen and in other UV blocking coatings; use

as a medium for electronic data storage and use as a photo-catalyst.[18] As a photo-catalyst, TiO_2 is active in the ultra-violet range and can be doped to be active in both the visible and uv ranges. The TiO_2 surface catalyzes hydrolysis of water into hydrogen and oxygen and reduction of CO_2 into methanol, formaldehyde, and other carbon containing compounds.[19] TiO_2 is inexpensive, stable and non-toxic, it is active under sunlight and in ambient conditions. The above factors contribute to our desire to understand photocatalysis on its surface.

1.7 Lattice Structure of Titanium Dioxide

The two most common forms of TiO_2, rutile and anatase, are distorted octahedrons.[20] Rutile has a tetragonal primitive unit cell and with 4/m 2/m 2/m symmetry.[17] The bulk titanium atoms in rutile are coordinated with six oxygen atoms while each oxygen atom is coordinated to three titanium atoms, as shown in Figure 5.

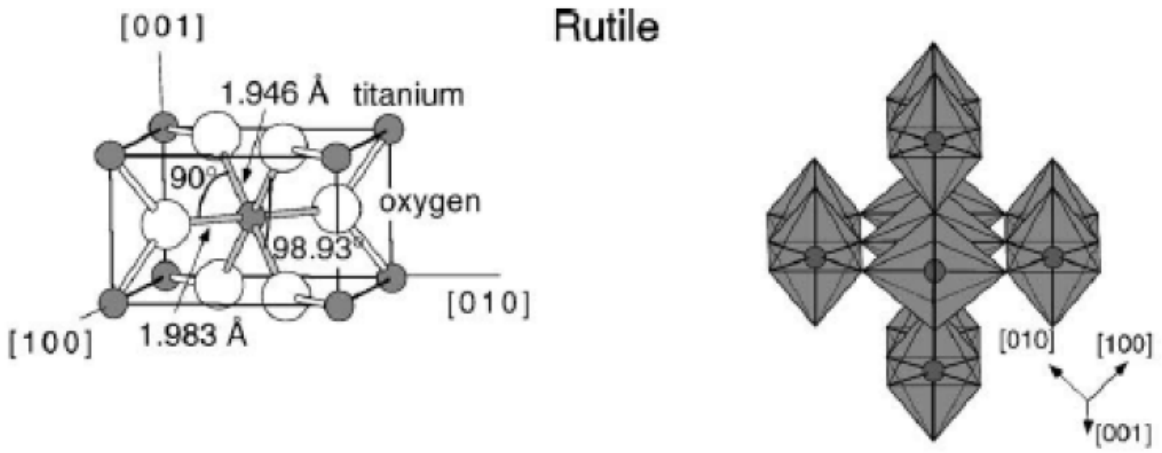

Figure 5: The rutile primitive unit cell and bulk structure are shown above, with bond lengths in Angstroms and the angles in degrees. Figure from reference (16).

The anatase unit cell, shown in Figure 6, is a tetragonal, 4/m 2/m 2/m. It is has lower symmetry than rutile.

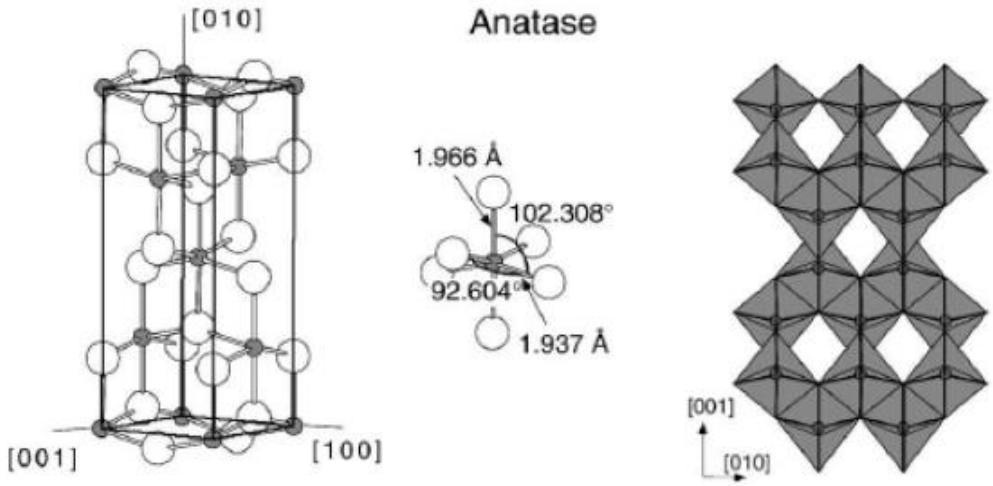

.

Figure 6: The anatase unit cell bulk structure. The bond lengths are in Angstroms and the angles are in degrees. Figure from reference (16).

1.8 Surface and Electronic Structure of Rutile (110)

Cleaving rutile along the 110 plane creates four distinct types of atoms on the surface, illustrated in Figure 7. Titanium atoms coordinated to six oxygen atoms, Ti-6c; titanium atoms coordinated to five oxygen atoms, Ti-5c; in-plane oxygen atoms coordinated to three titanium atoms, two Ti-5c and one Ti-6c atoms; and bridging oxygen atoms, O_{Br}, coordinated to two Ti-6c atoms. The bridging oxygen atoms form parallel rows along the [001] direction.

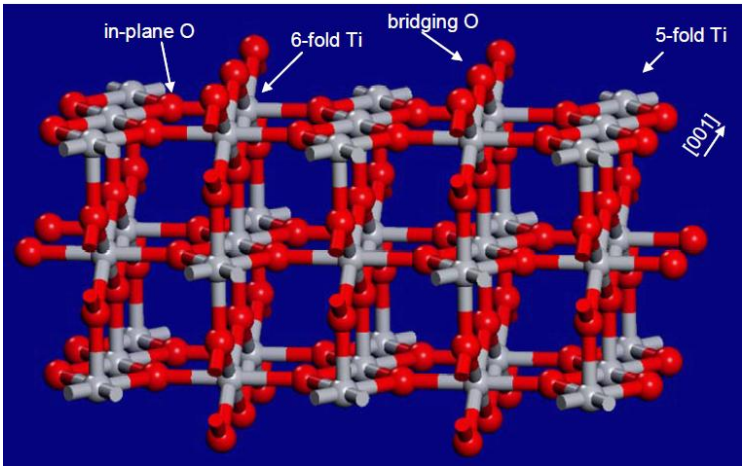

Figure 7: Rutile (110) surface showing Ti-5c, Ti-6c, OBr, and in-plane oxygen atoms [Figure from [21]].

The photoactivity of the TiO_2(110) rutile surface increases when bridging oxygen vacancies (V_O) are present, as the presence of V_O changes the electronic structure of the surface creating an inter-band donor state at 0.8 eV.[21] This inter-band state comes from vacant 3d orbitals on Ti atoms.[22] At room temperature and higher, O_2 will absorb on the surface, eliminating the inter-band donor Ti 3d state.[23] CO_2 adsorbs on the Ti^{4+} surface sites on the regular stoichiometric rutile (110) surface[24]. In the presence of bridging oxygen defects, CO_2 adsorbs in the vacancies over the Ti^{4+} sites[23]. The desorption energy for CO_2 at the bridging oxygen vacancy sites is 0.56 eV using TBD[25] and 0.5 eV using TDS [F]. The desorption energy at Ti^{4+} sites is measured with TPD to be 0.50 eV,[25] and with TDS to be 0.37eV.[26]

1.9 Surface and Electronic Structures of Anatase (001), (101), (010), and (110) Surfaces

Like rutile, the photoactivity of anatase surfaces increases when defects are present,[27] however V_O defects are less stable on the anatase surface, as they lead to the creation of a less stable Ti-4c site on anatase compared to the more stable Ti-5c site on rutile.[28-29] Also even the most stable

anatase surface (101) is less stable than rutile(110). Since anatase is less stable, it is more difficult to make suitable samples that can be used to experimentally determine the CO_2 binding energy and binding sites on the surface. TPD experiments suggest that on the perfect surface CO_2 binds to Ti^{4+} atoms,[27] and at defect sites to Ti^{3+} atoms.[27]

Different surfaces of anatase have different structures, leading to higher and lower coordination numbers and different surface electronic structure. Recent work by Cheng, Lu, and Liu suggest that the interplay between coordination and electronic structure determine the relative activities of the different surfaces making the (010) the most photo-active, followed by the (101) and the (001).[30]

1.10 Photoexcitation of Titanium Dioxide

TiO_2 is a semiconductor, which have band gap widths between that of a metal and that of an insulator as shown in Figure 8. The allowed energy states below the Fermi level are filled according to the Aufbau Principle, Hunds Rule and the Pauli Exclusion Principal. The conduction band, which is similar to a LUMO in a diatomic molecule, for TiO_2 has character of empty Ti 3d orbitals. The valance band, which is similar to the HOMO in a diatomic molecule, is composed mainly of O 2p orbitals. The Fermi level at zero Kelvin is half way in between the conduction and valance bands. The location of the Fermi level is governed by the Fermi-Dirac distribution, $f(E) = \frac{1}{1+e^{(E-E_F)/k_\beta T}}$. The energy space between the valance and conduction bands is called the band gap.

Figure 8: Semiconductors have band gap with widths between those of insulators and metals.

In photo-excited titanium dioxide, a photon with enough energy excites an electron from the valance band into the conduction band. When electrons are excited across the band gap, they leave holes in the valance band. Both the electrons and holes can serve as charge carriers. The band gap in rutile is 3.05 eV and in anatase it is 3.2 eV, thus to photo-excite rutile or anatase photons need energy greater than 3.05 or 3.2 eV. This is only a small portion of the available solar spectrum as shown in Figure 9. Considerable effort has been made to dope the semiconductors with atoms including N, S, and Transition metals; in an attempt to lower the band gap and increase the usable portion of the solar spectrum.

When an oxygen atom is removed from TiO_2, two extra electrons remain in the conduction band. These extra-unbound electrons can transfer to adsorbates such as CO_2. The extra electrons create inter-band gap donor states above the valence band and below the conduction band. The presence of these excess electrons causes the conduction band to bend towards a lower energy.

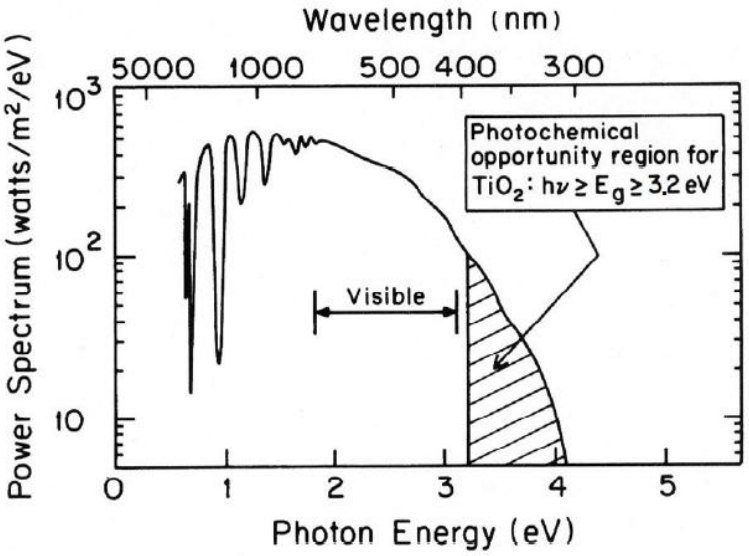

Figure 9: The solar power spectrum shows that only a small portion of photons in sunlight have enough energy to excite electrons across the band gap. Figure from reference (31).

1.11 Charge Carriers – Electron, Holes, and Recombination

When sunlight in the ultra-violet range impinges on TiO_2, it can excite an electron from the valance band to the conduction band leaving a hole in the valance band. The excited electron and the hole, with an effective positive charge, are attracted to each other. To photocatalyze a reaction involving CO_2, the sunlight must have enough energy to excite the electron and break the electron-hole pair. After the electron-hole pair has separated, the electron can transfer to CO_2 to reduce it or the oxidation of CO_2 could potentially occur where the hole is located. For TiO_2 to be a viable catalyst the electron-hole lifetime must be long enough that the photo-excited electron and/or hole can react with an adsorbate before recombining.

1.12 The Importance of Understanding Photo-Catalyzed Reactions of CO2 on TiO2 Surfaces

As we know, CO_2 is a greenhouse gas and intimately involved in climate change. The ability to take this pollutant from the atmosphere and convert it into usable compounds is preferable over producing the same compounds using methods which leave behind a large carbon footprint. Although much progress has been made in understanding the interaction between CO_2 and TiO_2, questions still arise such as guiding the reaction towards the desired product, improving the selectivity to reduce CO_2 over other molecules such as H_2O, finding ways to harness more of the photo-spectrum to name a few. The work we have done here, examining CO_2's interaction on different faces and forms of titanium dioxide and evaluating different models and levels of theory for doing so, gives insight into the initial binding of CO_2 to the surface and the flow of charge between CO_2 and TiO_2. Both of these will further our understanding of this system and effort towards solving the questions mentioned.

2. CHAPTER TWO: Theoretical Methods and Models

2.1 HARTREE-FOCK THEORY (HF)

The Hartree-Fock Theory, HF, is a mean field theory use to approximate a variational solution to the Schrödinger equation. It describes each electron as moving in a constant field of the nuclei and other electrons. The HF equations are solved with the notion that the energy derivative $\delta E = 0$, at the minima, and the orbitals always remain orthonormal. The *overlap integral*, S_{ij}, returns the likeness of $\chi_i$and χ_j, when $\chi_i$and χ_j are orthogonal $S_{ij} = 0$. The overlap integral is written as $S_{ij} = \int \chi_i \chi_j d\tau = \delta_{ij}$, where $\chi_i$and χ_j are one electron spin orbitals and δ_{ij} is the Kronecker delta. This constrained energy minimization is solved with the use of Lagrange multipliers.

$$\delta E + -2\delta \sum_i \sum_j \varepsilon_{ij} S_{ij} \ = 0 \tag{1}$$

Where E is the function to minimize, S_{ij} is the constraint and $-2\varepsilon_{ij}$ is the Lagrange multiplier, representing the single particle energies. The HF solution is the wave-function that gives the minimum energy within the constraints. This solution must include each of the electrons' motions at the same time and the coupling of these motions. That is moving an electron in a spin orbital, affects a second electron in a second spin orbital.

The Hamiltonian for the HF equations can be divided into three Hamiltonian operators: a core, a Coulomb and an exchange. The equations are then written as shown below where (1) and (2) represent electrons.[32]

$$\left[-\frac{1}{2}\nabla_i^2 - \sum_{A=1}^{M}\frac{Z_A}{r_{iA}}\right]\chi_i(1) + \sum_{j\neq i}\left[\int d\tau_2 \chi_j(2)\chi_j(2)\frac{1}{r_{12}}\right]\chi_i(1) + -\sum_{j\neq i}\left[\int d\tau_2\, \chi_j(2)\chi_i(2)\frac{1}{r_{12}}\right]\chi_i(1) = \sum_j \varepsilon_{ij}\,\chi_j(1) \quad (2)^{32}$$

In equation (2), $\hat{H}_{core} = \left[-\frac{1}{2}\nabla_i^2 - \sum_{A=1}^{M}\frac{Z_A}{r_{iA}}\right]$, the first term represents the kinetic energy of each electron, i, and the second term the attraction to the nuclei, Z_A, at distance, r, from the electrons.[32] The Coulomb operator, $\hat{J}_j = \int d\tau_2 \chi_j(2)\frac{1}{r_{12}}\chi_j(2)$, gives the average potential felt from an electron at distance, r_{ij}, in spin orbital, χ_j. The exchange operator, $\hat{K}_j(1)\chi_i(1) = \left[\int d\tau_2\, \chi_j(2)\chi_i(2)\frac{1}{r_{12}}\right]\chi_i(1)$, describes the effect of permuting electron (1) in spin orbital, χ_i, with electron (2) in spin orbital, χ_j It represents the correlation between electrons of the same spin and acts to lower the energy by spatially separating electrons with parallel spins[32]. The HF equation can be written using the one electron Fock operator, $\hat{f}$, as $\hat{f}_i\chi_i = \sum_j \varepsilon_{ij}\chi_j$, which can be transformed with the use of Lagrange multipliers to only have a non-zero value when $j = i$. This gives unique eigenvalues, ε_i, and is written as, $\hat{f}_i\chi_i = \varepsilon_i\chi_i$.

2.2 COUPLED CLUSTER THEORY (CC)

Coupled cluster theory expands on HF theory by applying a projection operator, the exponential cluster operator to the HF wave-function, or in principle any, reference wave-function.[32] The coupled cluster wave-function is written as,

$$|\Psi\rangle = e^{\hat{T}}|\psi_{HF=0}\rangle$$

where the Hartree-Fock wave function, $\psi_{HF=0}$ is the zeroth order approximation.[32] The cluster or excitation operator, $\hat{T}$ is a sum of excitation operators where $\hat{T} = \sum_{i=1}^{n} \hat{T}_i$, for the 1st, 2nd, 3rd, n^{th} excitations. The operators for the excitations are written using creation and annihilation operators. The creation operators, $\widehat{a^{\dagger}}$, add electrons to virtual orbitals $a, b, c,..$ and the annihilation operators, $\hat{a}$, remove electrons from occupied orbitals $i, j, k, .,.$ and t_{ij}^{ab} represents coupled cluster amplitudes. The first excitation operator is $\widehat{T_1} = \frac{1}{1!1!}\sum_i \sum_a t_i^a \hat{a}_a^{\dagger}\hat{a}_i$, while the second is written as $\widehat{T_2} = \frac{1}{2!2!}\sum_{i,j}\sum_{a,b} t_{ij}^{ab}\hat{a}_a^{\dagger}\hat{a}_b^{\dagger}\hat{a}_j\hat{a}_i$. The prefactor, $^1/_{(2!2!),}$ prevents the double counting of electrons. If all excitations are included in $\hat{T}$, then CC gives the results of full Configuration Interaction theory. One can truncate the excitation operator, $\hat{T}$, at any order and CC will still give physical, size extensive results. Two single excitations give a disconnected double excitation and a cubed single excitation gives a triple excitation. If $\hat{T}$ is truncated the solution very closely follows the variation principle, and is near close, but not always the upper bound to the energy. This plays a role in the calculation of excited states.

The single reference coupled cluster methods used in this research are: coupled cluster including single and double excitations, CCSD, and coupled cluster including single, double and triple excitations, CCSD(T). In CCSD(T), the triple excitations, (T), are obtained using

perturbation theory. We also used the multi-reference MR-CCSD, MR-CCSDT and MR-AQCC coupled cluster methods.

Systems far from equilibrium, with near degenerate ground states, small band gaps, and/or open shells radicals are not well described using a single Slater determinant. Such systems require multiple Slater determinants to give a good description of their wave-function. These methods are called multi-reference methods. In MRCC the wave function is written as a sum of multiple determinants accounting for different levels of active particles and active holes.[33]

The MR-AQCC and MR-ACPF methods use a CASSCF reference space. These two multireference methods are linearized forms of CC. They both also use techniques developed earlier for the MR-CI program.[33] MR-AQCC is size extensive, unlike CI. Analytical gradients are made easier in MR-AQCC because of its functional form.[33] MR-AQCC was developed by Szalay, Bartlett, and Fusti-Molnar.[34-36] The MR-ACPF method was developed by Gdanitz and Ahlrichs.[37]

2.3 MØLLER-PLESSET (MP)

The second order Rayleigh-Schrodinger perturbation theory, recovers much of the correlation energy by treating the Hamiltonian operator for the true system as a sum of a reference Hamiltonian and a perturbation. This is written as $\hat{H} = \hat{H}_0 + \hat{H}_1$, where $\hat{H}_0$ is the reference Hamiltonian operator and $\hat{H}_1$ is the perturbation.[32, 38] When the reference Hamiltonian is the Hartree-Fock Hamiltonian operator then the method becomes Second Order Møller-Plesset

Theory, MP2. That is Møller-Plesset theory, the Hamiltonian is written as a sum of a zeroth order approximation, $\hat{H}_0$, plus a multiplier, λ, times an external perturbation, $\hat{V}$, to the Hamiltonian, $\hat{H} = \hat{H}_0 + \lambda\hat{V}$.[32, 38] When used in the Schrodinger equation, MP theory takes the following form,

$$\left(\hat{H}_0 + \lambda\hat{V}\right)\left(\sum_{i=0}^{n} \lambda^i \psi^{(i)}\right) = \left(\sum_{i=0} \lambda^i E^{(i)}\right)\left(\sum_{i=0}^{n} \lambda^i \psi^{(i)}\right) \tag{3}$$

We used second order Møller-Plessent perturbation theory, MP2, in this research. MP2 tends to over-estimate the dispersion energy. The method has the advantage that it is size consistent; however, it is not variational and can give energies below the ground state. MP2 scales as N^5 with the system size.

2.4 CASSCF: COMPLETE ACTIVE SPACE SELF CONSISTENT FIELD THEORY

Complete Active Space Self Consistent Field theory, CASSCF or CAS, is a multiconfigurational SCF method. As such, the CAS wave function is composed of a linear combination of Slater determinants and is able to describe states that need more than one configuration to well define them. Some examples are excited states, ground states with near degeneracies and descriptions of bond breaking and forming. If all electrons and all orbitals are correlated in the CASSCF method, it will give the full CI theory description. Full CASSCF would capture both dynamic and static electron correlation. As usually implemented, it is able to capture mostly static electron correlation.

As CASSCF methods are usually implemented specific important configurations are correlated, that is valence electrons and molecular orbitals are specified. CASSF will use this information to describe all configuration functions that can be constructed from the given combination of active electrons and active orbitals. In a CASSCF calculation, the orbitals are considered core, active and virtual. The choice of a CASSCF active space is essential to its success. One wants to choose the electrons and orbitals hence the configurations that are most involved in the process of interest. For example, for a silicon dimer one would include the HOMO and LUMO orbitals in the CASSCF active space.

The major drawbacks of CASSCF methods are that it requires a proper selection of the active space and scales factorially as the number of electrons and orbitals correlated in the calculation increases.[39]

2.5 CASPT2, CASPT3: COMPLETE ACTIVE SPACE PERTURBATION THEORY

Complete Active Space Perturbation Theory, CASPT, is able to treat both static correlation because of its multireference approach and dynamical correlation by its perturbation component. CASPT uses a multireference function as its reference state. CASPT2 and CASPT3 use second and third order perturbation theory. CASPT partitions the Hamiltonian as is done with MP theory and implements a multidimensional reference space that spans more than one CASSCF state.[40-41]

2.6 DFT AND DFT BASED METHODS

2.6.1 Introduction to DFT

Density functional theory, DFT, provides a method to calculate the ground state electronic structure of a system as a unique functional of the ground state electron density, $n(r)$.[32, 42-43] DFT differs from Hartree-Fock type methods, which use the many electron wave-function to elucidate the electronic structure. High-level wave-function methods are more accurate than traditional DFT, although this depends on the method and choice of basis set. However, such methods become intractable as systems become larger than the $\mathcal{O}(10^3)$ atoms for MP2 and $\mathcal{O}(10^2)$ for CCSD(T).[32, 42-43] On such systems methods such as DFT are possible.[32, 43]

DFT has improved our chemical understanding of large systems such as proteins, adsorbate-surface systems and solvated molecules and ions[43]. Exploring these larger systems is unmanageable using traditional wave-function based methods, i.e. systems where the number of atoms is greater than $\sim\mathcal{O}(10^3)$.[42-43] Post-Hartree Fock and HF methods scale with the number of basis functions, which in turn scale with the number of electrons.[32, 43] For simple basis sets there can be ~10 basis functions per atom for first row elements.[32] Some examples of scaling, with B as the number of basis functions, are: HF~B^{3-4}, MP2 ~B^5, and Coupled clusters ~B^7. While methods such as coupled cluster give excellent approximations to the Schrodinger equation, they are infeasible for larger systems.[32] DFT on the other hand scales as N^{2-3}, where N is the number of atoms. This scaling can be further reduced with the use of linear scaling approaches.[32, 42] DFT is useful in that it can efficiently give us atomic level insight into large systems.[32, 42-43]

2.6.2 Understanding DFT

Understanding of DFT revolves around physical quantities.[42-43] Wave-function based methods work in truncated Hilbert Space of single particle orbitals, which for accurate calculations can utilize ~10^9 Slater determinants[43] to describe electronic states. DFT uses the three dimensional ground state electron density, n(r) in real space.[32, 42-43] Two other physical quantities of importance in DFT are the linear response function, $x(r,r';\omega)$, and the exchange correlation hole density, $n^{xc}(r,r')$.[32, 43] The exchange correlation hole density is the reduction in electron density at r' from an electron at r.[43] The linear response function, $x(r,r';\omega)$, describes the effect a perturbing potential at r' with frequency ω, has on $n(r)$ at r, [43] Mentally it is less daunting to try to understand these physical concepts than it is to comprehend truncated Hilbert Space with millions of basis functions.

The idea behind DFT is that the complete ground state electronic structure of a system can be uniquely described as a functional of the ground state electron density, $n(r)$, giving the electronic minimum energy.[32, 42-43] For systems with degenerate ground states DFT gives one of the ground states[43]. This is proven by the Rayleigh-Ritz minimization principle.[32, 42-43] For a non-degenerate ground state, with N electrons moving in the potential $v_1(r)$, with ground state electron density $n(r) = N\int\psi^*_1\psi_2 dr_1 dr_2$, and ground state energy E_1, the Kinetic energy operator is T, the electron-electron interaction operator is V_{ee}, and H_i is the Hamiltonian operator for the potential $v_i(r)$.[32, 42-43]

$$E_1 = \int v_1(r)n(r)dr + (\psi_1, (T + V_{ee})\psi_1) = (\psi_1, H_1\psi_1) \quad (4)$$

For the same system with a different potential, $v_2(r) \neq (v_1(r) + \text{a constant})$, and a different ground state wave-function $\psi_2 \neq e^{i\theta}\psi_1$ with a different electron density $n(r)$ the following equation describes the energy.[43]

$$E_2 = \int v_2(r)n(r)dr + (\psi_2, (T + V_{ee})\psi_2) = (\psi_2, H_1\psi_2) \quad (5)$$

Because of the Rayleigh-Ritz minimization principle for the unique ground state of ψ_1, E_1 must be less than E_2.

$$E_1 < \int v_2(r)n(r)dr + (\psi_2, (T + V_{ee})\psi_2) = (\psi_2, H_1\psi_2) = E_2 + \int (v_1(r) - v_2(r))n(r)dr \quad (6)$$

Also the reverse must be true, with the exception that ψ_2 is not necessarily degenerate[32, 42-43].

$$E_2 \leq (\psi_1, H_2\psi_1) = E_1 + \int (v_2(r) - v_1(r))\, n(r)dr \quad (7)$$

This leads to the conclusion that[43]

$$E_1 + E_2 < E_1 + E_2 \quad (8)$$

Hence two potentials unequal within a constant cannot produce the same ground state $n(r)$[32, 42-43]

Two key aspects of DFT are the Hohenberg-Kohn, HK, Variational Principle and the Kohn-Sham, KS, self-consistent equations[43]. The Hohenberg-Kohn variational principle, allows the calculation of the ground state energy from the Rayleigh-Ritz minimization principle as a function of a trial electron density $\check{n}(r)$; versus the traditional method using trial wave-functions, ψ_t [32, 42-43].

Given that $\check{n}(r) = N\int \psi^*_t \psi_t \, dr$ and $\psi_{\alpha\check{n}}$ is the set of trial wave-functions with a fixed $\check{n}(r)$, a constrained energy minimum can be obtained.[32, 42-43] Using the electron density instead of a sum

of single particle wave-functions, changes the problem from that of minimizing a function in $3N$ dimensional space, where N is the number of basis functions in the basis set, to one of minimizing a function of density in three dimensional space.[43] The constrained ň(r) with the constrained energy minimum is [32, 43-44]

$$E_v[\check{n}(r)] \equiv \min_{\alpha}(\psi_{\alpha\check{n}}, H\psi_{\alpha\check{n}}) \tag{9}$$

where

$$E_v\,[\check{n}(r)] \;=\; \int v(r)\check{n}(r)dr \;+\; F[\check{n}(r)] \tag{10}$$

and

$$F[\check{n}(r)] \equiv \min_{\alpha}(\psi_{\alpha\check{n}}, (T+V_{ee})\psi_{\alpha\check{n}}) \tag{11}$$

F[ň(r)] is independent of the potential v(r), it depends on the kinetic and interaction energies of ň(r). The energy is minimized with respect to ň(r), the minimum energy gives the (or a) ground state electron density for the system according to the HK theory.[32, 42-43]

$$E = \min_{\alpha} E_v[\check{n}(r)] = \min_{\alpha} \{\int v(r)\check{n}(r)dr + F[\check{n}(r)]\} \tag{12}$$

The second idea necessary to the useful implementation of DFT is the Kohn-Sham theory. The self-consistent Kohn-Sham (KS) equations involve the concept of interacting electrons moving in an effective single particle potential[32, 42-43]. The KS equations employ ideas of Euler and Lagrange so that the KS equations are minimized while conserving the number of electrons. To derive the KS equations F[ň(r)] is now written with the non-interacting electron kinetic energy functional, $T_s[\check{n}(r)]$, the coulomb electronic repulsion term, and the exchange-correlation energy functional, $E_{xc}[\check{n}(r)]$.[32, 42-43]

$$E_v[\check{n}(r)] \equiv \int v(r)\check{n}(r)dr + Ts[\check{n}(r)] + \tfrac{1}{2}\int drdr'\check{n}(r)\check{n}(r')/|r-r'| + E_{xc}[\check{n}(r)] \geq E \tag{13}$$

In the Euler-Lagrange form, with ε conserving the number of electrons,

$$\delta E_v[\check{n}(r)] = \int \check{n}(r)[v_{eff}(r) + \partial/\partial_{\check{n}(r)} T_s[\check{n}(r)]|\check{n}(r)=n(r) - \varepsilon\}dr = 0 \tag{14}$$

where,

$$v_{eff}(r) \equiv v(r) + \int dr' n(r')/|r-r'| + v_{xc}(r) \quad (15)$$

and

$$v_{xc}(r) \equiv \partial/\partial_{\check{n}(r)} E_{xc}[\check{n}(r)] \; |\check{n}(r)=n(r) \quad (16)$$

The effective potential, $v_{eff}(r)$, allows electron interaction via the exchange-correlation functional.[32, 42-43] This is reminiscent of the self-consistent Hartree equations, with v_{eff} instead of the Hartree potential, $v^H(r) = -Z/r + \int n(r')/|r-r'| \, dr'$, the single particle KS equations parameterizing the ground state n(r) as written as follows:

$$(-\tfrac{1}{2}\nabla^2 + v_{eff}(r) - \varepsilon_j)\varphi_j(r) = 0 \quad (17)$$

and

$$n(r) = \sum_{j=1\ldots N} |\varphi^j(r)|^2 \quad (18)$$

$$v_{eff}(r) = v(r) + \int dr' n(r')/|r-r'| + v_{xc}(r) \quad (19)$$

The local exchange-correlation potential is $v_{xc}(r)$, is density dependent. The KS ground state energy is written below.[43-44]

$$E = \sum_j \varepsilon_j + \int n(r)\{e_{xc}[n(r)] - v_{xc}[n(r)]\}dr - \tfrac{1}{2}\int dr dr' \check{n}(r)\check{n}(r')/|r-r'| \quad (20)$$

Where the first term, ε_j is the sum of the KS one electron energies, the rest of the terms correct for double counting.[43-44] If an exact form of the exchange correlation functional were known DFT could give the exact ground state energy of the system including exchange and correlation effects. The form of the DFT functionals allow for the solution of an interacting electronic ground state. Finally it is important to note that the KS single particle wave-functions have no physical meaning themselves only that through $n(r) = \sum_{j=1\ldots N} |\varphi^j(r)|^2$ we get the physically meaningful ground state electronic density. Interestingly the work function or ionization energy is approximately the magnitude of the highest occupied Eigenvalue relative to the vacuum. This

was demonstrated by Almbladh and U. von Barth in 1985.[45] The use of an adequate form of the exchange-correlation functional dictates the quality of DFT results.

2.6.3 The Exchange-Correlation Functional

This section is going to first briefly introduce electron exchange and correlation then move to discuss the exchange-correlation functional, and specifically the B3LYP, PBE and PW91 functionals

Electronic exchange is a quantum mechanical manifestation of the Pauli Exclusion Principle, which forbids electrons to be in the same quantum state at the same time. The electronic wave-function must be anti-symmetric with respect to the exchange of two electrons and electrons with the same spin cannot exist in the same region of space at the same time. Electronic exchange spatially separates pairs of electrons lowering the electrostatic repulsion energy between them. The avoidance electrons from each other and orthogonality constraint on different electronic states, gives rise to oscillations and nodes in the electronic wave function.

There are different ways to talk about electron correlation. It can be defined as the difference between the Hartree-Fock energy and the energy of the Schrodinger equation within the Born-Oppenheimer Approximation[32].

Electron correlation can be artificially divided into dynamic and static components. Dynamic electron correlation is due to instantaneous changes in electronic movements and positions due to the correlations in their movements. It is the fact that the movements of real electrons influence each other.[32, 42] Dynamic correlation is excitations outside the valence shell, or correlation of instantaneous repulsive electron movements.[32, 42, 44] Static electron correlation plays a large role when the ground state is composed of multiple near degenerate or degenerate

energy levels. Static electron correlation is considered electron excitations within the valence shell or correlation from approximate degeneracies in the wave function.[32, 42, 44] Methods, such as truncated CASSCF, which are composed of multiple slater determinants, can describe static electron correlation.

Correlation includes dispersion forces, the interactions of instantaneous dipoles that are continually created in interacting electron clouds. Correlation is very important for an accurate description of bond dissociation, and for systems dictated by dispersion interactions, such as a cluster of argon atoms. In the Si(100) surface there is a small energy gap between the HOMO, π, and LUMO, π^*, formed by the interaction of the dangling bonds of the surface atoms. This small gap between the ground and excited states allows the system to undergo a pseudo-Jahn-Teller distortion. This increases the importance of including effects of static electron correlation[8] to accurately model dimers. It also is a possible cause of the buckling behavior of the surface dimers. The relative flatness of Si(100)'s potential energy surface (PES)[8], linking the buckled and flat structures, indicates the need to incorporate electron correlation in Si(100) calculations.

DFT incorporates correlation and exchange through the exchange correlation functional, $E_{xc}[n(r)]$[32, 42-43]. Many early forms of $E_{xc}[n(r)]$ were based on the local density approximation (LDA) which bases the exchange correlation energy of the real system on that of a homogenous electron gas with the same electron density, n(r), as the real system at a point r. The LDA functional is:[32, 42-43]

$$E_{xc}[n(r) = \int e_{xc}(r; n(r')\ )\ n(r)dr'. \qquad (21)$$

This functional depends on the particular density at the point r and near points r'. Near is usually on the scale of the Fermi wavelength $(\lambda = 2\pi/k_f)$. It includes the exchange-correlation

energy per particle at r, $e_{xc}(r; n(r'))$,[32, 43] gives exact results for a uniform electron gas, and has given insight into the chemistry of real systems. LDA, however; has flaws.

LDA works well on systems with slowly varying electron density, but has difficulty in systems with rapid $n(r)$ fluctuations.[42] It faces trouble in high exchange energy electron systems, e.g. some types of magnetic systems.[32, 42-44] The spin order of magnetic systems is drastically unlike that of a homogeneous electron gas of the same $n(r)46$; hence LDA gives errors. LDA usually underestimates lattice parameters by a few percent.[32, 42-43, 46] Surprisingly, LDA also does well in predicting the magnetic moments of itinerant metals,[42, 44] where the non-local exchange interactions between conduction electrons are responsible for magnetic properties.[46] One hidden advantage of LDA is that its errors with exchange and correlation energies, E_x and E_c, tend to cancel. LDA over-estimates E_c, by up to twice its actual value, and underestimates E_x by ~10%. Normally $E_c << E_x$ so these errors partially cancel.[32, 42-44] A final problem of LDA, and DFT in general, is that an electron unphysically interacts with itself leading to the self-interaction error. Self-interaction corrected LDA, SIC, is one attempt to correct this.

For our calculations, we used functionals employing the Generalized Gradient Approximation, GGA. GGA functionals attempt to improve LDA's qualitatively wrong description of the exchange hole.[32, 42, 44] To better describe the exchange hole, GGA includes both $n(r)$ and its gradient with respect to position $\partial n(r)/\partial r$.[42] The GGA functional in spin dependent form is written,{Perdew, 1993 #242}

$$E_{XC\text{-}GGA}\, n(r)_\uparrow, n(r)_\downarrow \equiv \int F\, n(r)_\uparrow, n(r)_\downarrow, \nabla n(r)_\uparrow, \nabla n(r)_\downarrow \, dr \qquad (22)$$

GGA improves on LDA's calculated energies which can be off by up to 20%.[42] It also improves structural accuracy, bond dynamics, atomization energies and energy barriers.[47] GGA still fails

however in cases of high electron correlation, such as with transition metal oxides such as titanium dioxide. Another example CoO, an anti-ferromagnetic insulator, is predicted to be metallic. This is a result of GGA's and LDA's underestimation of electron correlation,[43] or more properly said, the inexact nature of traditional exchange correlation functionals.

2.6.4 B3LYP

B3LYP is a hybrid functional meaning it uses a portion of HF exact electron exchange to describe a portion of the exchange energy. The remainder of the exchange energy is taken from LDA and GGA Becke 88 functional. The correlation energy is taken from the LDA, VWN and the GGA LYP functionals. All values were parameterized to fit ionization potentials, atomization energies, proton affinities and atomic energies.[48]

2.6.5 PBE: Purdue-Burke-Ernzerhof Exchange-Correlation Functional

The Purdue-Burke-Ernzerhof Exchange-Correlation Functional, PBE, is a GGA functional that was intended to improve upon PW91. PBE implements fundamental constants in its formulation and applies techniques used in PW91. PBE was intended to give a better description of a uniform electron gas's linear response, and give a smoother potential than PW91.[42]

2.6.6 PW91

Two commonly used versions of GGA are that of Becke, Lee, Yang and Parr,[32] BLYP (the other is that of Perdew and Wang.[32] In 1986 Perdew and Wang formulated a gradient exchange functional, PW86.[49] Later in 1991 Perdew and Wang introduced a correlation component to the functional form, PW91.[50] This PW91 functional is constructed from first principles.[50] It begins by expanding the exchange-correlation hole around an electron to a second order density-gradient expansion.[7] To satisfy sum rules for an electron hole, long-range "spurious" parts are removed[7]. PW91 is analytically designed to satisfy as many physical constraints as possible.

2.6.7 Problems with DFT

DFT is an efficient method able to quickly predict structures and ground state energies, and in theory it is an exact method, [43] however, as DFT is applied approximations are used to obtain the kinetic and exchange-correlation energies.[43, 51] To calculate the kinetic energy in DFT one uses one-electron non-interacting orbitals with a density that corresponds to the actual electron density. The exchange correlation functional must describe, not only exchange and correlation, but also the difference between the approximation for the kinetic energy and the actual kinetic energy. The inexact nature of the form of the exchange correlation functional used, leads to problems in DFT.

DFT can run into problems such as neglecting dispersion energies, treating systems with low-lying unoccupied orbitals, and calculating band gaps. DFT with traditional functionals is unable to include dispersion forces. Grimme states that one of DFT's shortcomings lies in its inability to describe medium-range electron correlation.[52] The failure of DFT with chemical

reactions (hence rapidly changing electron densities and unpaired electrons) incorporating radicals, cations, and anions; has been attributed to DFT's description of exchange.[53] The MO5-2x functional, developed by Truhlar and coworkers, is able to describe the exchange component accurately enough to describe chemical reactions. Some of the current research in the area of improving the exchange component is focused on including varying amounts of HF's exact description of exchange, Fock exchange. The amounts are tailored to chemical environment and distance. Work is also focused on improving DFT's description of electron correlation with the use of df-MP2 to describe correlation coupled Fock exchange. Martin and coworkers have made one such attempt and developed functionals that are able to give correct barrier heights for reactions involving late transition metals, weak interactions, main group thermo-chemistry and thermo-chemical kinetics.[53] To further complicate the issue specific functionals are ideal for select systems, giving binding and relative energies that perform well as compared to high level ab initio methods; but removing some of the molecules in the system could change the picture. For example work by Truhlar using over 70 functionals predicts that the ωB97X-D, LC-ωPBE-D3 and M05-2x functionals give the best results for $(H_2O)_{16}$ clusters, but finds that the picture changes when looking at $(H_2O)_6$ clusters.[54]

2.6.8 Van der Waals Corrected DFT

Density Functional Theory with traditional LDA and GGA functionals does not describe dispersion effects. Van der Waals forces are weak electrostatic forces that include multipole-multipole, dipole-dipole, dipole-induced dipole, and instantaneous induced dipole-induced dipole interactions. Dispersion forces are non-bonding, non-ionic forces between molecules or between groups on a molecule and dominate when covalent and strong electrostatic interactions are

absent[55]. Van der Waals forces are responsible for such things as increases in boiling points of simple alcohols with molecular weight, the π-π stacking between aromatic rings in DNA base pairs, condensed phases of rare gases, the structure of layered solids and geckos ability to climb surfaces. Van der Waals forces become important for non-dense systems, including van der Waals complexes, in areas of low density such as occurs in chemical reactions,[2] for geckos when they do not fall off trees, and those walking underneath who could potentially have a gecko fall on their head. Dispersion corrections also help describe the properties of metallic solids, insulators, and ionic solids.[56]

2.7 QUANTUM MONTE CARLO

2.7.1 Introduction

The first molecular computer simulation used a Monte Carlo method.[32] Monte Carlo (MC) methods start with an initial configuration, in the case of Quantum Monte Carlo (QMC), an initial electron configuration, and make random changes to generate new configurations. These new configurations are accepted in a probabilistic manner based on the ratio of the two energies and a random variable. Quantum Monte Carlo is a stochastic method, able to give an approximate solution to the Schrodinger equation. It is Markovian meaning that it only depends on the previous trial configuration, and where each trial configuration is taken from a finite number or outcomes. QMC methods, if done correctly, are ergodic that is given enough time, QMC will span configuration space. QMC as applied in this research relied on the sequential

application of Variational Monte Carlo (VMC) then the more reliable Diffusion Monte Carlo (DMC) method.

What follows is are short descriptions of the Metropolis MC, VMC, and DMC methods along with some components that improve their reliability.

2.7.2 Metropolis Monte Carlo

The Metropolis Monte Carlo (MMC) method uses importance sampling, which accelerates convergence by sampling important configurations, that is configurations which the system has a higher probability of occupying.

The Metropolis technique is as follows:

1) Randomly choose an initial configuration, C_n.

2) Generate a random number, p , between zero and one. Randomly choose a trial configuration, C_t, and calculate the ratio of the probabilities of the trial and initial, $R = \frac{P(C_t)}{P(C_n)}$. If the random number is less than or equal to the ratio, accept the trial configuration as the next configuration, $C_t = C_{n+1}$. If the random number is greater than R, the initial configuration is used as the next configuration, $C_{n+1} = C_n$.

3) Replace the initial configuration, C_n, with C_{n+1} and repeat step two until the limiting distribution or equilibrium distribution is achieved. Additional moves should not move the system out of equilibrium.

A more accurate way of describing the probability of moving to the trial configuration, $P_{n\to t}$, is as follows.

$$P_{n\to t} = minimum\left[\frac{P(C_t)}{P(C_n)}, 1\right]$$

More about the MMC method will be described below.

2.7.3 Variational Monte Carlo

Variational Monte Carlo uses the Monte Carlo technique along with the variational principal to calculate the energy of a multi-particle trial wave function[57]. That is the VMC energy is the upper bound of the of the true ground state energy. The trial wave function is usually generated from a HF or DFT based electronic structure calculation. The quality of the nodes of trial wave function controls the accuracy of the VMC calculation[57]. Since Monte Carlo integration techniques cannot effectively deal with the wave-function's anti-symmetry, the nodes in the trial wave-function are fixed, and the wave-function is treated as having one symmetry.[57] While the rest of the wave-function is improved in QMC, the nodes remained fixed. Any inaccuracies in the nodes remain perpetuate throughout the calculation.

The variational theorem is,[57]

$$E_V = \frac{\int \Psi_t(R) H \Psi_t(R) dR}{\int \Psi_t^2(R) dR} \quad (23).$$

Here E_V is the variational energy, R is the vector of electronic coordinates in 3-N dimensional space, and Ψ_t denotes the trial wave function. As used in VMC, the variational theorem is rewritten as a probability distribution, $p(R) = \frac{\Psi_t^2(R)}{\int \Psi_t^2(R\prime) dR\prime}$, and a term called the local energy, $E_L(R) = \Psi_t^{-1} \hat{H} \Psi_t$.{Foulkes, 2001 #149} The variational energy is then,[57]

$$E_V = \int p(R) E_L(R) dR \quad (24)$$

The above rearrangement of the variational energy is an importance sampling transformation of equation (23).[57] Writing the variational energy in terms of a probability and a local energy makes it possible to apply the MMC method to sample the probability distribution in an efficient

manner. As the trial wave function moves towards the true wave function, the local energy moves towards the energy Eigenvalue, E_i.[57]

The acceptance criteria, A, for moving the system from configuration R' to R is written in terms of the transition probability density, T.[57]

$$A(R \leftarrow R') = min\left\{1, \frac{T(R\prime \leftarrow R)\Psi_t^2(R)}{T(R \leftarrow R\prime)\Psi_t^2(R\prime)}\right\} \quad (25)$$

The acceptance criteria satisfies the detailed balance criteria as is shown by rearranging equation (25).[57]

$$\Psi_t^2(R)T(R' \leftarrow R)A(R' \leftarrow R) = \Psi_t^2(R')T(R \leftarrow R')A(R \leftarrow R') \quad (26)$$

This method is Markovian, that is the new configuration only depends on the pervious configuration, and if the transition probability is ergodic, then the VMC algorithm will converge.[57]

In VMC the energy is calculated in terms of the number of configurations, M, generated after they system equilibrates to the limiting distribution.[57]

$$E_V \simeq \frac{1}{M}\sum_{i=1}^{M} E_L\,(R_i) \quad (27)$$

As the trial wave function moves towards the true fixed-node wave function, the number of sampling points in configuration space needed to estimate the Eigenvalue, energy decreases and the smoothness of the local energy increases.[57]

In this work, we used a Slater-Jastrow form of the trial wave function.[57]

$$\Psi_{SJ}(R) = e^{J(R)}\det\left[\psi_n\left(r_i^{\uparrow}\right)\right]det\left[\psi_n\left(r_j^{\downarrow}\right)\right] \quad (28)$$

Where the symmetric Jastrow factor includes particle correlations and enforces the nuclear cusp condition. It is written as terms that sum over particles and includes electron-electron, electron-nuclei, and electron-electron-nuclei correlations. More terms can be included. We also

experimented with adding back-flow correlation of particles, as it can improve the nodal surface,[57] but did not see enough of an energetic advantage for the time used.

Several parameters in the trial wave function were optimized to minimize the variance of the VMC energy. The variance of the VMC energy is written below, with alpha representing variable parameters.[57]

$$\sigma^2(\alpha) = \frac{\int [\psi_T^\alpha]^2 [E_L^\alpha - E_V^\alpha] dR}{\int [\psi_T^\alpha]^2 dR} \tag{29}$$

In this research, VMC was used to improve the trial wave function by optimizing parameters within it. The VMC calculations generated electronic configurations that we used in subsequent DMC calculations.

2.7.4 Diffusion Monte Carlo

Diffusion Monte Carlo, as used in this study, approximates the solution to the imaginary time Schrodinger equation. The imaginary time Schrodinger equation, in atomic units, is written below.[57]

$$-\frac{\partial}{\partial t}\Phi(R,t) = \left(\widehat{H} - E_T\right)\Phi(R,t) = \left(-\frac{1}{2}\nabla_R^2 + V(R) - E_T\right)\Phi(R,t) \tag{30}$$

In the above equation, E_T is the reference energy, an energy offset that is involved with normalizing the wave function - $\Phi(R,t)$, and controlling the configuration population[57]. The potential energy of the configuration R is $V(R)$, and $t = \frac{\tau}{i}$ tracks the propagation of trial wave function as it approaches the actual wave function in t, real time, and tau, imaginary time. [57]

Considering the DMC initial state, $\sum_i c_i \phi_i(R)$, as probability distribution, which requires the fixed-node approximation, gives insight into the DMC Hamiltonian. Note that when applying the fixed-node approximation, the wave function goes to zero at the nodes, but is an

Eigenfunction of the Hamiltonian elsewhere. Looked at in this manner, the DMC imaginary time Schrödinger equation has two parts. First, if only the potential term were present, the DMC imaginary time Schrödinger equation becomes a rate equation[57]. Second, if only the kinetic term were present, the DMC imaginary time Schrödinger equation is a diffusion equation.[57] The rate portion of the equation controls what is called branching. Branching occurs when more favorable electronic configurations replicate and less favorable configurations disappear.[57]

DMC uses a projection operator,$e^{-t\hat{H}}$, to project out the ground state solution. Which when writing the wave function as a sum of the Eigenstates, ϕ_i, illustrates how states of interest have the greatest impact.[57]

$$\Phi(R,t) = \sum_i e^{-(E_i - E_T)t} c_i \phi_i(R) \tag{31}$$

As the DMC calculation approaches the limiting distribution, the ground state wave function, ϕ_0, is projected out.[57]

$$\Phi(R, t \to \infty) \simeq e^{-(E_0 - E_T)t} c_0 \phi_0(R) \tag{32}$$

Applying importance sampling greatly improves the convergence rate of DMC. When applied, the probability of sampling from important parts of the wave function increases as the density of configurations increases in areas where the absolute value of the wave function is large[57]. In addition, the local energy, instead of the potential energy, influences branching. This is advantageous as the local energy is a smoother function facilitating the evaluation of Coulomb interactions, which helps the energy error bar to decrease more rapidly.[57] To introduce importance sampling, the Schrödinger equation is written using the mixed distribution, $f(R,\tau) = \Psi_{\mathrm{T}}(\mathrm{R})\Psi(R,\tau)$ and the drift velocity $v(R) = \Psi_T^{-1}(R)\hat{H}\Psi_T(R)$.[57]

$$-\frac{\partial f(R,\tau)}{\partial t} = -\frac{1}{2}\nabla_{\mathrm{R}}^2 f(R,\tau) + \nabla_{\mathrm{R}} \cdot [\mathrm{v}(\mathrm{R}) f(R,\tau)] + [E_L(R) - E_T] f(R,\tau) \tag{33}$$

In the above formulation of the Schrödinger equation; $\frac{1}{2}\nabla_R^2 f$, controls diffusion; $\nabla_R \cdot [vf]$, represents drift and; $[E_i - E_T]f$, governs branching[57]. Rewriting the Schrodinger equation in real time with a Greens function and the mixed distribution gives equation (34).[57]

$$f(R,\tau) = \int G_D(R \leftarrow R',\tau) G_B(R \leftarrow R',\tau) f(R',t') dR' \quad (34)$$

The Green's function is a solution to the importance sampled Schrödinger equation, with the condition that at time zero, the Green's function equal zero unless the two electronic configurations are identical. To save time the Green's function is estimated by an approximation of the function for the exact solution as the time step goes to zero. The approximation contains drift and branching components. An acceptance-rejection step is incorporated to reinforce detailed balance, which is not satisfied by the Green's function approximation.

The DMC energy is written as in equation (35).[57]

$$E_{DMC} \equiv E_0 = \frac{\iint \phi_0(R,t) H \Psi_T(R) dR dt}{\iint \phi_0(R,t) \Psi_T(R) dR dt} = \frac{\int f(R) E_L(R) dR}{\int f(R) dR} \quad (35)$$

DMC offers an accurate method able to recover 90-95% of the correlation energy, because of this it is an attractive and successful alternative to DFT and wave function based methods.

2.8 Basis Sets and Pseudopotentials

In order to approximate the Schrodinger equation, one needs to mathematically describe atomic orbitals. An excellent approximation is given by a Slater-type orbital, STOs, which have a cusp at zero distance from the nucleus. This well describs the charge and spin at zero distance.[32] STOs also have a long decaying tail so they well describe long-range interactions between

atoms.[32] However, Slater orbitals are computationally difficult to work with, so they are often replaced with linear combinations of Gaussian or Plane-Wave orbitals.

2.8.1 Gaussian Basis Sets

Gaussian orbitals have the form $x^a y^b z^c \left(e^{-\alpha r^2}\right)$ where α represents the spread of the function, r is distance and a, b, c are powers of Cartesian variables x, y and z. Basis sets with un-contracted or primitive Gaussians, allow optimization of the exponent and the coefficient, from the linear combination, during the calculation. These give good results, but are expensive to use. Minimal basis sets such as STO-3G and STO-4G, contain only enough functions to describe the filled atomic orbitals[32]. One of the problems with minimal basis sets is that they use the same number of functions for all atoms in a single row, so they give worse results for fluorine and oxygen, than they would for lithium and beryllium.[32] The limited number of functions prevents minimal basis sets from describing anisotropy in the electron density.[32] For example in second row elements the $2p_x$, $2p_y$, and $2p_z$ must have the same radial components in a minimal basis set. A final problem with minimal basis sets is they contain only one contraction per atomic orbital so that the functions cannot expand or contract to describe its environment.[32] No minimal basis sets were employed in this work. However, a minimal basis set was used with earlier work involving TiO_2-CO_2.

Double Zeta, DZ, basis sets are an improvement over minimal basis sets as DZs have twice the number of basis functions.[32] DZ basis sets use linear combinations of contracted and diffuse Gaussians where the coefficients on each are optimized.[32] DZ basis sets are able to predict anisotropies. A combination between minimal and DZ, split-valance, SV, basis sets use

two Gaussians for valence orbitals, which are most active in chemical reactions, and one Gaussian for core orbitals.[32]

Polarizations functions are able to give a more accurate picture of anisotropy than DZ and SV.[32] Some examples are s and p-orbitals forming an 'sp' type and a vacancy in a d-orbital changing the symmetry of p-orbitals. Polarization functions include higher angular momentum functions, such as a p type functions on helium atoms and d type functions on beryllium atoms.[32]

2.8.2 Diffuse Functions

Diffuse functions become important in cases involving significant electron density far from the nucleus such as in ions, lone pairs, and reactions.[32] We used diffuse functions for exploring CO_2-TiO_2 interactions since the interaction shifts electron density away from the nuclei.

2.8.3 Density Fitting

Density fitting basis sets greatly reduce the I/O and storage requirements needed to perform a calculation.[32] This method uses linearly scaling auxiliary basis sets and applies least-squares fitting to multi-index, (four index) electron repulsion integrals.[58]. Density fitting, DF, estimates two electron integrals by approximating the two electron density with a summation.[58] For example, a two-electron integral describing electron repulsion using orbitals is shown below.

$$(pq|rs) = \int dr_1 \int dr_2 \phi_p(r_1)\phi_q(r_2)\frac{1}{r_{12}}\phi_r(r_1)\phi_s(r_2)$$

This equation can be rewritten using the two electron density, $\rho_{ab}(r) = \phi_a(r_1)\phi_{bq}(r_2)$, to give the equation below.[58]

$$(pq|rs) = \int dr_1 \int dr_2 \rho_{pq}(r_1) \frac{1}{r_{12}} \rho_{rs}(r_2)$$

The density is then described using an auxiliary basis set with fitting coefficients d_P^{pq}.

$$\bar{\rho}_{pq}(r) = \sum_{P}^{N_{fit}} d_P^{pq} \chi_P(r)$$

This introduces a very small error, but gives a very large computational savings. The auxiliary basis sets used are most often atom centered Gaussians, three to four times larger than a standard basis set.[58]

Density fitting basis sets are formulated slightly differently for different methods. Density fitting sets for evaluating the Coulomb integrals, Coulomb fitting sets, work well with HF and DFT, while larger DF sets that fit exchange integrals, JK-fit, do a nice job of fitting the DFT exchange integral. These JK-fit sets perform poorly with HF. MP2 and coupled cluster method have their own special DF sets for use with correlation-consistent basis sets.[59]

Two approximations that are similar to density fitting are the pseudo-spectral approximation and the Cholesky decomposition. The pseudo-spectral approximation uses real space grids in its auxiliary set, which replaces the atom centered Gaussians.[59] The Cholesky decomposition, like DF techniques, simplifies four index electron repulsion integrals with sums and products of three index electron repulsion integrals, however, it does this by applying a slightly different technique.[59]

Density fitting is also called Resolution of the Identify, as DF looks similar to the mathematical RI procedure, but there are slight differences.

2.8.4 Plane-Wave Basis Sets and Pseudopotentials

One method to describe the electronic wave function in a periodic system is to use plane waves and pseudopotentials. Plane waves describe the natural movement of a free electron, they are easy for humans to understand and implement into codes well. For example in a periodic system described by Bloch's Theorem the single particle wave function, φ_k, is written as:

$$\varphi_k(\mathbf{r}+\mathbf{R}) = e^{i\mathbf{kR}}\varphi_k(\mathbf{r}).$$

Where the position is **r** and the real lattice vector is **R**. The quantum number, **k**, is directly related to the crystal momentum $p=\hbar k$, and gives the boundary conditions for the single particle wave function. The Bloch wave function leads us to the solution of the single particle wave function for a constant potential lattice,[32, 60] (this constant potential can be chosen to equal zero.)

$$\varphi_k = e^{i\mathbf{kr}} \sum_G C_G(\mathbf{k}) e^{i\mathbf{Gr}} \tag{36}$$

$$\varphi_k = e^{i\mathbf{kr}}\, \omega(\mathbf{k},\mathbf{r}).$$

The sum in equation (36) is a Fourier series over all reciprocal lattice vectors, G.[60] Plane waves are the natural language of a Fourier series; they are also Eigenfunctions of the momentum operator, p, and all powers of p. Hence, plane waves are natural Eigenfunctions of the kinetic energy operator, i.e. they describe the motion of free electron.[32, 60]

Considering a constant potential lattice, $V\equiv 0$, with the wave function, $\varphi = Ne^{i(k+G)r}$, where N is a normalization constant. Using plane-waves, the Rydberg band energies are simply $E_{band} = (k+G)^2$. Next, moving to the Nearly Free Electron model, that is adding a small perturbing periodic potential, ΔV, to the system, the wave functions become a mix of plane waves. That is the bands are slightly perturbed and mix with other bands. The largest contributing factor to the band mixing comes from bands of similar energy.

The use of plane-waves changes again with their application to the electronic structure of solids. Solids have a strong perturbing potential, electrons and ions strongly interact with each other through a Coulombic interaction. This strong perturbing potential should lead to significant band mixing, requiring each wave function to be a complicated mix of plane waves. However, the Thomas-Fermi Liquid Theory, FLT, of metals simplifies this picture.[42] The FLT says that near the Fermi level, electronic excitations act as independent quasiparticles.[42] That is they have renormalized intensities and masses, and most importantly behave in as non-interacting particles at low energies. The FLT provides a basis for plane wave implementation to describe the electronic structure of metals. FLT, tells us that Coulomb interactions of the valance electrons are weaker than thought. That is the exchange, correlation and Hartree potentials are weaker than a simply Coulombic energy, and that perhaps the valence electronic interactions are small enough to use a NFE approximation.[32, 60]

After the FLT guides us to plane wave description of valence electrons, we are left with the problems of describing core electrons and valence electrons near the ions. Near the nuclei, there is a strong Coulombic interaction between electrons and the ions. Because of the need to maintain orthogonality between electronic states and the strong coulombic force, electrons are rapidly oscillating and moving with high kinetic energy. These rapid oscillations would make the use of plane wave near the nuclei difficult. This leads to the use of pseudopotentials. The pseudopotential approximation is based on the idea that near the nucleus electrons are tightly bound and little affected by events outside of the core region. These core electrons are viewed as almost constant. In this region, the strong Coulombic potential is replaced by a weaker pseudopotential. The idea is that the pseudopotential reproduces the exact potential felt by electrons outside the core and the actual wave function outside of the designated core region,

while giving a weaker potential and a node-less wave function within the core. Thus, pseudopotentials facilitate the plane wave description of electronic structure in solids.[32, 60]

Unfortunately, like all approximations, pseudopotentials have drawbacks. The "Frozen Core Approximation," is not always applicable to elements with extended core states, such as transition metals. While implementing pseudopotentials can give a fast, simple and effective description of electronic structure, the generation of the pseudopotential itself is computationally time consuming.[32, 60]

The calculations for some of this work were done using the Ultra-Soft Pseudopotentials, US-PP, developed by Vanderbilt and coworkers.[61-62] The US-PPs have the property that the pseudo-wave function matches the actual wave function outside the "core" radius, r_c, however; for radii less than the core radius, the two wave functions do not match. In the core region of Vanderbilt's US-PP, the pseudopotential, V_{ps}, is constructed to be as soft as possible. This softness means that less plane waves are required in the expansion to construct the valence-pseudo-wave function.[32, 60]

As compared to the often-used Norm-Conservation Pseudopotentials, NC-PP, the US-PPs differ in their treatment of the core region. In the core, the $\varphi_{ps} \neq \varphi_{actual}$, with NC-PP the norm of the wave function is set to match the norm of the actual wave function. That is,

$$\int_{0\rightarrow rc} dr\, r_2 \varphi^{*ps}(r)\varphi^{ps}(r) = \int_{0\rightarrow r^c} dr\, r_2 \varphi^{*}(r)\varphi(r) \qquad (37)$$

The use of norm conservation helps to reproduce the correct charge density, it also improves the transferability of the pseudopotential.[60] Remember, pseudopotentials are generated for atomic reference states and that the environment of the atomic reference state is quite different from that of the solid crystal.[60] Pseudopotentials with high enough transferability can accurately model the behavior of electrons in solids. The Vanderbilt US-PPs lose some transferability due to lack of

norm conservation. However, the Vanderbilt US-PPs were developed for use in large-scale calculations, where the computational cost of developing a pseudopotential is much smaller than the cost of the calculation itself.[60] Because they are ultra-soft and the condition of norm conservation is relaxed, the generation of a Vanderbilt US-PP is computationally less demanding than that of a NC-PP to develop, and the US-PP can easily be recalculated as the calculation progresses and the local environment changes.[60]

The US-PPs do not have norm conservation, as is true with NC-PP.

$$n(r) \neq \sum \varphi^{*ps}\varphi^{ps} \tag{38}$$

To reproduce the electron density with US-PP an augmentation charge must be added to the equation.

$$n(r) = \sum \varphi^{*ps}\varphi^{ps} + \sum_{mn} Q_{nm}(r)\langle\varphi^{j}|\beta^{n}\rangle\langle\beta^{m}|\varphi^{j}\rangle \tag{39}$$

In the second term, the augmentation, Q(r) is a local function given in the pseudopotentials generation and β is an angular expansion containing a spherical harmonic and a radial function. The augmentation term goes to zero if $r > r_c$, it only exists inside the core radius, as outside this region, the pseudo-wave function matches the real wave function. [60]

For the Vanderbilt US-PP, total energy is written as,

$$E_{Tot} = \sum_{occ}\langle \varphi^{j}| T+V^{NL} |\varphi^{j}\rangle + \int d^3r\, V^{L}(r)n(r) + \tfrac{1}{2}\int d^3r d^3r' n(r)n(r') /|r-r'| + E_{xc}\, n(r) + E_{RR} \tag{40}$$

Here V^{NL} is the non-local Vanderbilt ultra-soft pseudopotential. Non-local implies that it contains angular momentum and magnetic moment terms. The term V^{L} is the local component of the pseudopotential, the φ^{j} is the pseudo-wave function, T represents the kinetic energy operator, the third term is the Hartree potential, V^{H}, the exchange-correlation functional is E_{xc} n(r), and the final term represents the nuclear-nuclear repulsion. The non-local potential is defined with spherical harmonics and radial functions,

$$V^{NL} = \sum_{mn} D_{(0)nm} |\beta^n\rangle\langle\beta^m| \quad (41).$$

Where $D_{(0)nm}$, are coefficients, and as state earlier β^n, are a radial and angular momentum dependent angular expansion functions.[60]

After the previous discussion, we are in position to discuss the implementation of US-PPs. The Kohn-Sham secular equation, solvable with the variational principle is

$$H|\varphi_j\rangle = \varepsilon i S|\varphi^j\rangle \quad (42).$$

Where the Vanderbilt Hamiltonian is written as follows,

$$H = T + V^{xc}(r) + V^{H}(r) + V^{L} + \sum_{mn} D_{nm} |\beta^n\rangle\langle\beta^m| \quad (43)^{60, 62}$$

Here T, is the kinetic energy operator, $V^{xc}(r)$ is the exchange correlation potential, $V^{H}(r)$ is the Hartree potential, V^{L} is the local part of the pseudopotential, and D_{nm} is $D_{(0)nm}$ with an additional screening term.[60, 62] This term includes the local potential, and components of the exchange correlation, and Hartree potentials. Back to the secular equation, (42), the overlap matrix, S, is as follows, where q_{nm} is an integral over the core sphere

$$S = I + \sum_{mn} q_{nm} |\beta^n\rangle\langle\beta^m| \quad (44)$$

$$q_{nm} = \int_{0 \ldots rc} d^3 r Q_{nm}(r) \quad (45).$$

In the above equation, (45), Q_{nm}, is the difference between the actually charge density and the pseudo-charge density. Of course the two charge densities are equal for $r > r_c$, as the wave functions match outside the core region. Finally, with Vanderbilt US-PPs, the pseudopotential can evolve as the self-consistent solution progresses. That is the augmenting charge evolves as a portion of the potential used to solve the Kohn-Sham equations. This improves the accuracy of the US-PPs and allows them to be ultra-soft: giving smoother wave functions while, using less plane-waves then earlier pseudopotentials.[60, 62]

2.8.5 Pseudopotentials with the QMC Framework

In QMC calculations it is common to implement the pseudopotential approximation to make it feasible to simulate structures with heavier atoms, as the computational cost for DMC increases rapidly with atomic number (Z), around $Z^{5.5}$.[63-64] The fixed-node approximation makes the use of non-local pseudopotential difficult as the non-local part influences both sides of the nodes. We used the locality approximaton[65] to circumvent this issue. In the locality approximation the non-local portion of the pseudopotential acts on the trial wave function instead of the DMC wave function.[65] This creates an error whose largest order portion is proportional to the square of the difference between the trial wave function and the true ground state wave function, within the fixed node approximation.[65]

3. CHAPTER THREE: PW91 Studies of Hydrogen's Effect of the Surface Structure of Si(100)

3.1 Introduction

The purpose of this project is to theoretically investigate how hydrogen adsorption in the monohydride phase on the Si(100) surface, influences the buckling of neighboring dimers. The calculations are performed using DFT[66-67]-PW91[50, 68] with slab models and period boundary conditions as implemented in VASP.[69-72] This work is motivated by the experimental works of Buehler and Boland[7] and of Dürr, Hu, Biedermann, Höfer and Heinz.[73]

We are addressing the question of whether the adsorption of two hydrogen atoms on a silicon dimer, in the monohydride phase, induces a measurable elastic strain field un-tilting neighboring dimers in the same row. This has been reported by Buehler & Boland.[7] That is can the adsorption of hydrogen onto the bare Si(100) surface create a measurable strain field altering the buckling of the p(2x2) and c(4x2) surfaces into that of the symmetric (2x1) phase? At low temperatures the c(4x2) structure is considered the most stable[5] , while the p(2x2) surface is only a few meVs higher in energy per dimer. In these surfaces, interaction between dimers lifts the degeneracy of the dangling bonds, creating π and π^* states with a small energy gap between them[9]. The intra-dimer interaction of these states, leads to a pseudo-Jahn-Teller effect. This, combined with the relatively flat potential energy surface, allows dimers to undergo rapid room

temperature vibrational buckling behavior. The normal modes and mixing between near degenerate states creates an unfavorable interaction at the higher symmetry. Experimental work,[5, 7, 74] suggests that the dangling bond ordering is long range, extending over many dimers on the bare surface. The same works also suggest that defects[5] and hydrogen adsorption,[7, 74] on the surface interrupts the dimer interactions altering the dimers phase. We are trying to theoretically reproduce hydrogen's interruption, or strain on the dimers. To do this we are using DFT-PW91 to examine the Si(100) surface with different coverages and locations of the hydrogen adsorbates. We are running calculations on the c(4x2), and p(2x2) surface structures (Figure 10). For the bare Si(100) surface, a surface with one silicon dimer passivated, 2H*Si(100) (Figure 11), and different configurations of 4H*Si(100) surfaces with two dimers passivated (Figure 12).

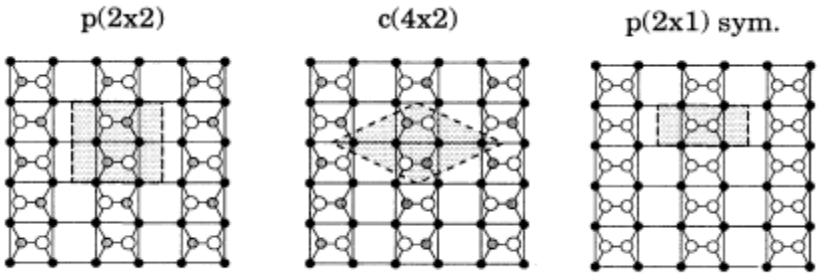

Figure 10: Dimer reconstructions, from [75], showing the top view of the p(2x2), c(4x2) buckled and symmetric (2x1) surfaces. The white and grey circles represent the top layer of dimers, with circles being 'up' and the grey circles as 'down.' Small dark circles represent atoms in the next layer, the remaining layers are not shown. The dark shaded parallelograms represent the surface unit cell.

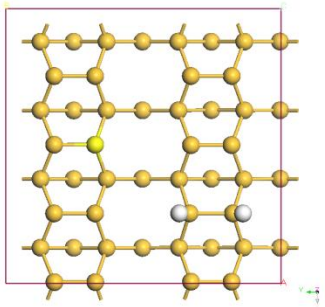

Figure 11 : Top view of the 2H*Si(100) monohydride structure with two hydrogen atoms adsorbed on the same dimer. This picture shows three layers of silicon atoms (gold). The hydrogen atoms (white) are located on the same dimer on the two surfaces considered p(2x2) and the c(4x2)

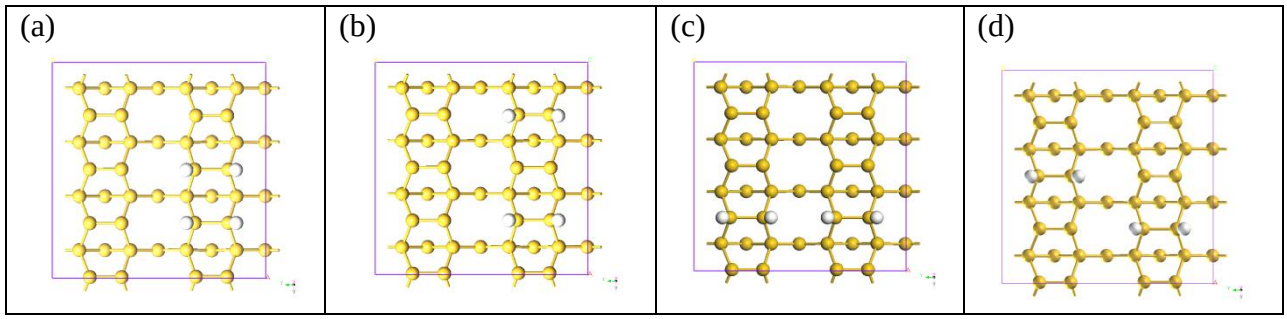

Figure 12: different adsorbate configurations of hydrogen on Si(100). (a) H atoms on neighboring dimers in the same row, (b) H atoms in the same row on alternating dimers,(c) H atoms on neighboring dimers in different rows, and (4) H atoms in opposite rows on next nearest neighbor dimers.

If hydrogen adsorption induces a strain field altering the dimer surface phase, we should observe bond lengthening [7], and buckling angle reduction[7] for dimers in the same row.

As previously mentioned, the chemistry and behavior of the Si(100) surface is controlled by dangling bonds, dimer-dimer interactions,[5, 7] and electron correlation[8] Cleaving bulk silicon, forming the Si(100) surface creates two dangling bonds per surface atom. The dimer reconstruction eliminates one dangling bond from each atom, leaving one remaining dangling bond per atom. As stated above it is the interaction of these dangling bonds that stabilizes the c(4x2) and p(2x2) bare surfaces more than the symmetric (2x1). This view is altered with the

addition of hydrogen adsorbates. Each hydrogen atom binds to a silicon atom on a dimer, eliminating the remaining dangling bond on that silicon atom, leaving the number of dangling bonds on the other atoms unchanged. In this work, we examine how the adsorption of hydrogen changes the interactions of the dangling bond network and therefore the dimer structure.

In our work, we used the VASP software package,[69-72] the DFT -PW91 level of theory and Vanderbilt's ultra-soft pseudopotentials. Our plane wave basis sets explicitly include waves with kinetic energies less than 300 eV, 250 eV or 200 eV. For k-space sampling we used the method of Monkhorst and Pack, with 1x1x1, 3x3x1, 4x4x1, 5x5x1 grids, giving 1, 5, 8, and 13 irreducible k-pts in the 1st Brillouin Zone. Our Silicon models contain two rows of four dimers or two rows of eight dimers, five layers of silicon atoms to give the desired fractional coverages and a 16 Å vacuum layer. We performed convergence tests regarding the thickness of the vacuum layer.

3.2 Theoretical Methods

Density functional theory, DFT, with the slab model and periodic boundary conditions was used to perform all calculations of the Si(100) and H*Si(100) surfaces. The periodic boundary conditions give an infinite surface, eliminating edge effects so we could better understand manifestations of the surface itself as opposed to the surface's reaction to truncation. The models used all have a 16 Å vacuum layer, five layers of silicon atoms with hydrogen capping the fixed bottom layer. We used two different size slabs. The smaller model, Figure 13(a), has two dimer rows with four dimers in each row. It contains 80 silicon atoms with 32 hydrogen atoms capping the bottom layer. The larger model, Figure 13(b), has two rows of dimers, with

eight dimers in each row. It has 160 silicon atoms with 64 hydrogen atoms capping the bottom layer. We ran calculations on these slabs with two different phases of silicon dimer reconstructions with different monohydride configurations on the surfaces. The purpose of this was to observe the effect hydrogen has on the surface geometry.

(a) (b)

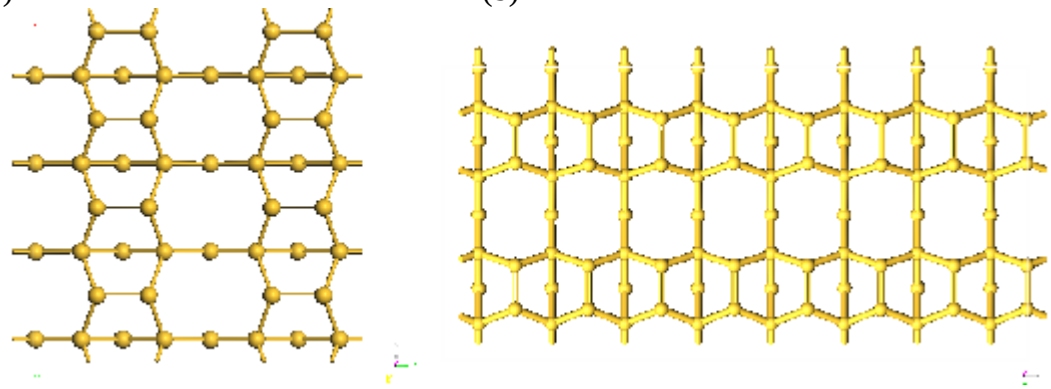

Figure 13: Base models to which hydrogen was added. (a) The four dimer Si(100) model and (b) the eight dimer Si(100) model. Both slabs show only the top three silicon layers for clarity.

Looking at the smaller eighty atom Si(100) model, for the clean Si(100) surface two different surface phases were used p(2x2)and c(4x2).

For the H*Si(100) surface, models were constructed with varying hydrogen concentrations. Calculations for each of the H*Si(100) surface reconstructions were run with two hydrogen atoms bonded to different Si atoms on the same dimer in a di-mono-hydride dimer configuration, and four hydrogen atoms bonded in the di-mono-hydride configuration to two different dimers. The configurations of the four dimer models are shown in Figure 14. Calculations for these models were run with both spin unrestricted and spin restricted DFT-PW91.

(a) (b)

(c) (d)

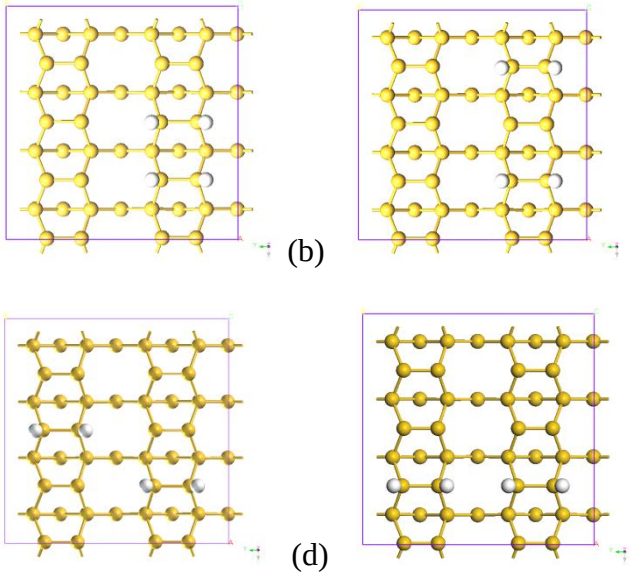

Figure 14: Adsorbate configurations of hydrogen on the Si(100): (a) four H atoms on neighboring dimers in the same row, (b) H atoms in the same row on alternating dimers, (c) four H atoms in opposite rows on next nearest neighbor dimers and (d) four H atoms on neighboring dimers in different rows.

Higher hydrogen coverages were run for the c(4x2) eight silicon dimer models, Figure 15. These contained eight hydrogen atoms on four dimers completely saturating one row, six hydrogen atoms on three dimers in one row, leaving one dimer in the slab bare, and two configurations involving six and eight hydrogen atoms on alternating rows shown in Figure 15(d). Calculations were performed using DFT-GGA (PW91). We performed spin restricted calculations on all models. Additionally, for the models with three di-mono-hydrogen passivated dimers, we performed spin-unrestricted calculations.

(a) 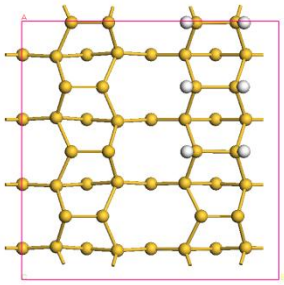 (b) 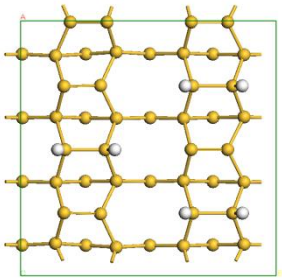

(c) 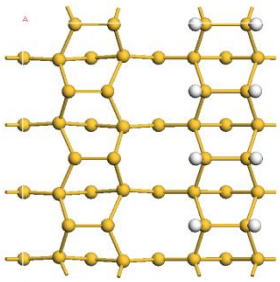 (d) 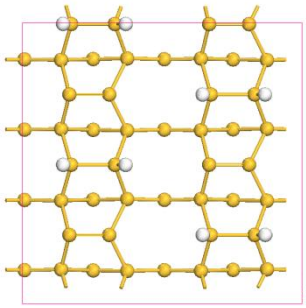

Figure 15: Higher hydrogen surface coverages: (a) three passivated silicon dimers in the same row, (b) two passivated dimers in one row and one in the second row, (c) four passivated dimers in the same row, (d) four passivated dimers in alternating dimers.

For the larger models, the 160 silicon atom slabs, calculations were run on Si(100)-c(4x2) and p(2x2) surface configurations. The purpose of using the larger cell was to observe long-range effects, extending over several dimers, in the structure. Calculations were done with minimal hydrogen coverage on all surfaces and for higher hydrogen coverages on the c(4x2) surface. The minimal hydrogen coverages included four hydrogen atoms giving two di-mono-hydrides dimers, shown in Figure 16.

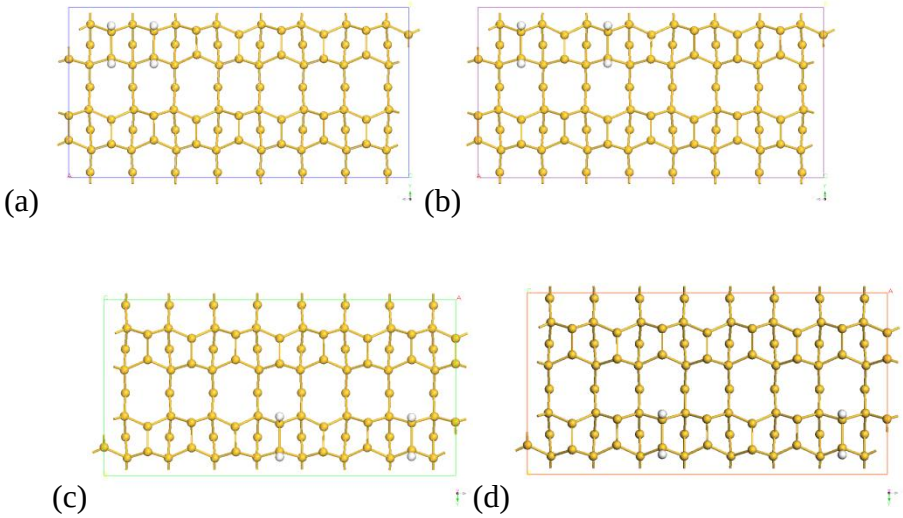

Figure 16: Hydrogen surface configurations on the larger 160 Si atom slab models: (a) two passivated dimers in the same row, (b) two next nearest neighbor passivated dimers in the same row, (c) two alternating passivated and bare dimers (d) two passivated dimers with three bare dimers between them.

For the higher hydrogen surface coverages, we performed calculations on two different di-mono hydride dimer arrangements. These are shown in Figure 17

.

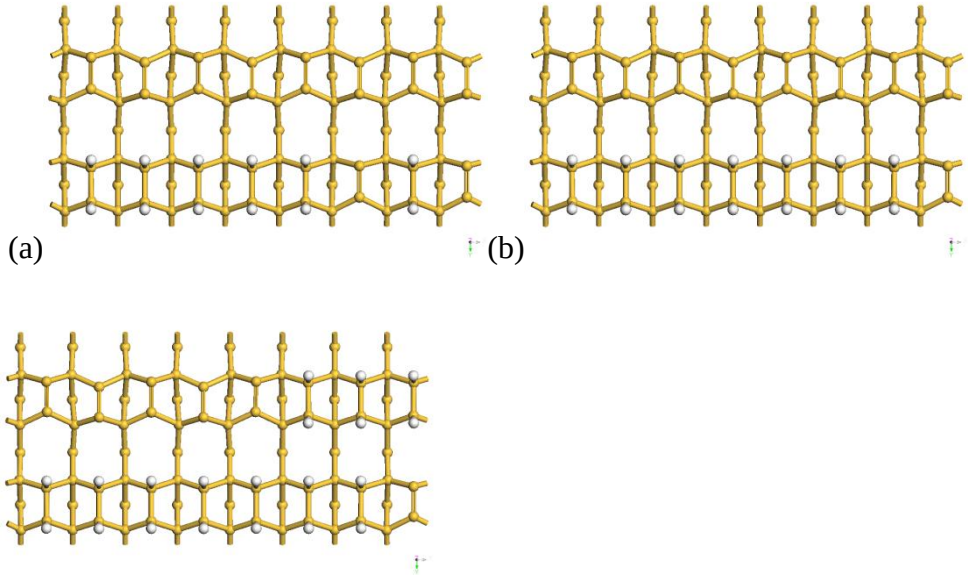

Figure 17: Hydrogen surface coverages for models with: (a) six passivated dimes (b) seven passivated dimers and (c) ten passivated dimers.

All calculations were run in the VASP software package, using DFT, a plane wave basis set, the Vanderbilt ultra-soft pseudopotentials,[62] US-PP and the PW91 approximation to the exchange-correlation functional. The conjugate gradient algorithm was used to optimize the ionic steps. For the smaller models, calculations were run with 200eV, 250eV and 300 eV cut off energies for the US-PP. The larger models were run with a 250 eV cut off energy.

We performed calculations for bulk silicon to converge the DFT-PW91 lattice parameter. These were performed with multiple k-point meshes and pseudopotential energy cutoffs to test the convergence of both parameters. Next, the optimized unit cell and lattice parameter were used to construct the Si(100) unreconstructed surface with five layers and a hydrogen layer capping the bottom silicon row. The surface was reconstructed to form dimers and calculations were rerun to optimize the various surface dimer configurations, c(4x2) and p(2x2). Next, surfaces with the different di-mono-hydride dimer configurations were optimized.

3.3 Results and Discussion

It is difficult to compare our results with those of Buehler and Boland[7]. The phases of the silicon surface are a continuum and even adding a small amount of energy will shift the dimers to a different configuration. When is the buckling angle small enough that it is no longer consider buckled and considered symmetric? Experimental buckling angles are approximately 20° for the c(4x2)[76] somewhat less for theoretical results.[76] They are similar for the p(2x2) phase, and 0° in the symmetric dimer. When are the buckling angle and dimer configuration close enough to the symmetric phase that one observes changes in the chemical and physical behavior of the Si(100) surface?

It has been observed, especially in the presence of hydrogen bonded to neighboring dimers, that the reactivity of symmetric dimers is greater than that of buckled towards hydrogen adsorption.[7, 77-78] It has also been observed that the sticking probability of hydrogen increases at higher surface temperatures.[79] At room temperature the dimers are dynamically flipping between the c(4x2), p(2x2) and (2x1) phases,[7] causing the position of the dimers to average and appear symmetric. We first present our results for the bare surface for two phases of Si(100): c(4x2) and p(2x2) , and then present results for calculations performed with hydrogen saturating dimers in the monohydride phase.

For the bare p(2x2) and c(4x2) surfaces the DFT average dimer bond length, $r^{Si\text{-}Si}$, and buckling angle, $\langle\theta_{bulk}\rangle$, are shown in Table 1.

Table 1: Average dimer bond length (Å) and buckling angle in degrees for the bare Si(100) surface in the c(4x2) and p(2x2) phases.

	$r^{Si\text{-}Si}$	$\langle\theta_{bulk}\rangle$
c(4x2)	2.347	13.18
p(2x2)	2.349	13.11

The results in angle and dimer bond length for the p(2x2) and c(4x2) bare surfaces are virtually identical. No change was observed for the buckled structures when spin was included.

For the dimer slabs with two hydrogen atoms passivating one dimer and four hydrogen atoms passivating two dimers, the bond angle, length changes are in Table 2.

Table 2: For the c(4x2) and p(2x2) phases with two hydrogen atoms on one dimer and four hydrogen atoms on two dimers dimers, the range of bond lengths for the bare dimers (r^{Si-Si}), the average bond lengths for the saturated dimers ($r^{HSi-SiH}$), the angle for bare dimers adjacent to saturated dimers (θ_a), the angle for a bare dimer farther away from the saturated dimer (θ_{bulk}), and the percent difference between the buckling angles ($\%\Delta\theta$).

	r^{Si-Si}	$r^{HSi-SiH}$	θ_a	θ_{bulk}	$\%\Delta\theta$
c(4x2) 2H	2.32 – 2.35	2.38	11.75	13.49	12.88
c(4x2) 4H	2.33 - 3.35	2.41	13.01	13.14	1.04
p(2x2) 2H	2.32 - 2.35	2.41	12.28	13.08	6.09
p(2x2) 4H	2.33 - 2.35	2.403	12.12	13.17	7.94

The angle changes were reduced by 6% to 8% for the p(2x2) phase and by 13% and 1% for c(4x2) phase. For the c(4x2) eight dimer slab, the results with four higher hydrogen coverages are listed in,

Table 3.

Table 3: Eight dimer c(4x2) slabs with three and four saturated dimers. The columns are the average bond length between bare dimers, the average bond length for the saturated dimers, the minimum buckling angle, all adjacent to saturated dimers, the average buckling angle for the bare surface from Table 1, and the maximum percentage difference. All bonds are in angstroms and all angles in degrees.

	$r^{Si\text{-}Si}$	$r^{HSi\text{-}SiH}$	θ_a	$\langle\theta_{bulk}\rangle$	$\%\Delta\theta$
3 filled dimers alternating rows	2.30	2.41	11.69	13.18	11.3
3 filled dimers in the same row	2.30-2.35	2.41	11.53	13.18	12.5
4 filled dimers alternating rows	2.31	2.41	11.4	13.18	13.5
4 filled dimers in the same row	2.35	2.40	13.18	13.18	-0.04

For the three di-mono-hydride dimers in the same row and in alternating rows, the maximum bond angle change was 11.3% and 12.5% for each surface respectively. For the c(4x2) slabs with four dimers saturated with eight hydrogen atoms, the dimer angle change was13.5% between the alternating passivated dimer configuration and the bare surface. When each of the dimers in one row was passivated hydrogen atoms, there was negligible change in θ between the bare dimers in the adjacent row and θ in the bulk.

For the larger sixteen dimer c(4x2) model, there was a slight increase in θ for dimers furthest away from the di-mono-hydride dimers, while the adjacent dimers had a 7% to 17% decrease in buckling.

Table 4: Results for the sixteen dimer slab in the c(4x2) configuration with ten saturated dimers, six saturated dimers, seven saturated dimers and four models with two saturated dimers. The first column is the minimum buckling angle, the next the maximum buckling angle, and the last is the percent difference. All angles are in degrees.

	θ_a	$\langle\theta_{bulk}\rangle$	$\%\Delta\theta$	θ_{away}
20H & 6 bare dimers	11.75	13.18	10.85	13.44
12H & 10 bare dimers	11.82	13.18	10.32	13.25
14H & 9 bare dimers	11.81	13.18	10.39	13.24
skip0 4H &14 bare dimers	12.36	13.18	6.22	13.42
skip1 4H & 14 bare dimers	10.94	13.18	17.00	13.25
skip2 4H & 14 bare dimers	12.10	13.18	8.19	13.29
skip3 4H & 14 bare dimers	12.28	13.18	6.83	13.20

In all cases, the smallest buckling angle was located adjacent to saturated dimer(s).

3.4 Conclusion

Are these results significant? That answer lies in the chemistry of the surface and how it changes with angle and phase. If so the hydrogen passivation would need to disrupt the dangling bond network enough that the energy for of planer p(2x1) configuration decreases relative to the buckled configurations, perhaps even making in the ground state configuration. Also, since surface phonons facilitate reactions by bringing a surface geometry to a higher energy more reactive state, it is possible that the hydrogen passivation could alter the phonon frequency enough to change the reactivity of the surface. These two possibilities could easily be studied by looking at the symmetric (2x1) configuration and using a method such as the nudged elastic band method to calculate the change in energy barrier between the bare and partially passivated surface.

Also, the energetic favorability of buckling is overestimated with DFT. The Si(100) dimerized surface is a biradical system. Each atom has one dangling bond. Because of its biradical character a single reference wave function does not give a complete description the silicon surface. A method such as MRMP2[80] which includes both static and dynamic correlation is needed to accurately describe the biradical Si(100) dimer phase. Using higher levels of theory often require cluster models, which introduce edge effects. It would be interesting to calculate the energetics using both cluster and slab models, and to parameterize and account for the effects of truncations introduced with the cluster models. This could effectively give us corrections to the models, to better understand what is occurring on the H*Si(100) surface.

4. CHAPTER FOUR: Silicon One and Two Dimer Model Systems for Exploring Electron Correlation Effects in the Buckling of SiSi Dimers on the Si(100) Surface

4.1 Introduction

The structure of the Si(100) surface has been the subject of numerous theoretical and experimental studies[8-9, 81-103] Since the LEED study of Schliar and Farnsworth,[97] it has been known that the surface reconstructs to give rows of silicon dimers.[86, 97] The prevailing view is that, in the minimum energy configuration, the dimers are buckled, with one atom of each dimer pair being displaced 'up' and the other 'down' and with the buckling of adjacent dimers alternating along a dimer row. [9, 81, 99-100] STM studies carried out in the early 2000s appeared to indicate that the dimers are unbuckled at low temperatures and in the absence of defects.[90, 103] However, subsequent studies established that the observation of unbuckled dimers in the low-temperature STM measurements was a consequence of tip-surface interactions,[83, 92, 96] and, at present, the consensus is that experimental data is consistent with a buckled surface at low temperature.[75, 101]

The situation on the theoretical front, however, is still not completely resolved. While most Hartree-Fock and density functional theory (DFT) calculations favor buckled structures for the reconstructed Si(100) surface, [82, 84, 88-89, 93, 104] complete active-space SCF (CASSCF)[105] and multi-reference MP2 (MRMP2)[80, 106] calculations favor unbuckled structures.[8, 82, 85, 89] Diffusion

Monte Carlo calculations (DMC)[57] have also been found to favor buckled structures, but with a smaller energy separation between buckled and unbuckled structures than found from the Hartree-Fock or DFT calculations.[87] The above-mentioned CASSCF, MRMP2, and DMC calculations have been performed using cluster models, whereas the DFT calculations have been carried out using both cluster and slab models with periodic boundary conditions. The DFT calculations show that even cluster models containing as few as three dimers give buckling energies per dimer close to the slab model results, when using the same functional.[94, 107]

What makes dimer buckling a challenging electron correlation problem is the fact that each surface dimer has a weak π bond and, as a result, has a small HOMO(π)/LUMO(π*) gap, which imparts diradical character to the surface dimers.[87, 89, 108] (Due to the pyramidalization of the surface dimer, the so-called π and π* orbitals actually contain some σ or σ* character.) From this perspective, the 'minimal' wave-function for describing the electronic structure of a SiSi dimer in its singlet ground state is of the form $c_1\pi^2 + c_2\pi^{*2}$. The degree of diradical character or, equivalently, the relative importance of the c_2 term in the wave-function, decreases as a dimer buckles. It is precisely this aspect of the electronic structure of the surface dimers which has led Gordon and coworkers to question the applicability of DFT to this problem.[85, 89, 98]

A second intriguing aspect of the surface dimer problem is the role played by the coupling between dimers. Several theoretical studies have shown that the interactions between dimers increases the tendency toward buckling.[82, 87, 89] For example, Healy et al. have reported that the buckling stabilization increases from 0.7 kcal mol^{-1} per dimer to 2.5 kcal mol^{-1} per dimer in going from a two- to a three-dimer model.[87] The coupling between adjacent dimers is generally discussed in terms of a through-space mechanism.[109] Interestingly, Hartree-Fock calculations on a two-dimer, $Si_{15}H_{16}$ cluster model show that through-bond[109] interactions are

actually more important than the through-space interactions since the π_- orbital is more stable than the π_+ orbital and the π^*_- orbital is more stable than the π^*_+ orbital, where, neglecting overlap, $\pi_+ = 1/\sqrt{2}(\pi_1 + \pi_2)$, $\pi_- = 1/\sqrt{2}(\pi_1 - \pi_2)$, $\pi^*_+ = 1/\sqrt{2}(\pi^*_1 + \pi^*_2)$, and $\pi^*_- = 1/\sqrt{2}(\pi^*_1 - \pi^*_2)$ refer to localized $\pi(\pi^*)$ orbitals on the two dimers.

Whereas DFT and single-reference MP2 methods are best suited for describing dynamical electron correlation effects, the CASSCF method, with the active spaces generally employed, is most appropriate for dealing with non-dynamical correlation effects arising from near degeneracies. The MRMP2 and loosely related CASPT2[110] methods, which describe both types of electron correlation effects, would appear to be ideal approaches for addressing the dimer buckling problem. However, the fact that DMC calculations favor buckled structures suggests that correlation effects not recovered in multi-reference MP2 calculations play an important role in the buckling. One cannot conclude this definitively, since the DMC calculations made use of the fixed-node approximation and a long time step.[111]

The goal of the present study is not to 'solve' the problem of buckled vs. flat structures for the Si(100) surface, but rather to present 'minimalist' cluster models for testing various electronic structure methods for treating such problems. The two models considered, Si_2H_4 and Si_7H_8, are shown in Figure 18 and have one and two 'surface' dimers, respectively. For these two models, the energies of the buckled and unbuckled structures are calculated using the Hartree-Fock, MP2, CCSD,[112] CCSD(T),[113] CASSCF, CASPT2, CASPT3,[110] multi-reference-averaged-coupled-pair functional (MR-ACPF),[36-37, 114] multi-reference averaged quadratic coupled cluster (MR-AQCC),[36] and multi-reference coupled cluster (MR-CC)[115] wave-function based methods, the PW91[68, 116] and Becke3LYP[117-119] density functional methods, and the diffusion Monte Carlo method. The CASPT2, CASPT3, MR-ACPF, and MR-AQCC methods

all employ CASSCF reference spaces. The MR-CC method is a multi-reference coupled-cluster method, where the multiple references are generated from a single configurational wave-function. The MR-CC and DMC approaches are expected to be the most reliable for predicting relative energies of the buckled and unbuckled structures.

4.2 Theoretical Methods

The geometries of the Si_2H_4 (one dimer) and Si_7H_8 (two dimers) cluster models, shown in Figure 18, were generated from optimized structures from slab-model calculations on the unbuckled and buckled species as described using the PW91 density functional[68, 120] and carried out with the VASP program.[69-70, 72] The slab-model calculations employed five silicon layers, terminated on the bottom with H atoms as described in Ref. [6], and were carried out using periodic boundary conditions, with a planewave basis set with a 250 eV energy cutoff, and Vanderbilt ultra-soft pseudopotentials[62].

In generating the cluster models, the positions of the Si atoms were taken from the slab-model calculations, and the subsurface dangling bonds were terminated with H atoms. The SiH bond lengths were chosen to be 1.54Å and the bond angles and dihedral angles involving the H atoms were chosen to be the same as those for the corresponding Si atoms in the slab models. Exploratory calculations revealed that the energy differences between the planar and buckled structures are roughly the same with the small models employed here as for the larger Si_9H_{12} and $S_{15}H_{16}$ models that have been used in several earlier theoretical studies.[6, 82, 87, 98] The main

advantage of the smaller Si_2H_4 and Si_7H_8 cluster models is that they can be studied with high-level electronic structure methods that would not be feasible for the larger cluster models.

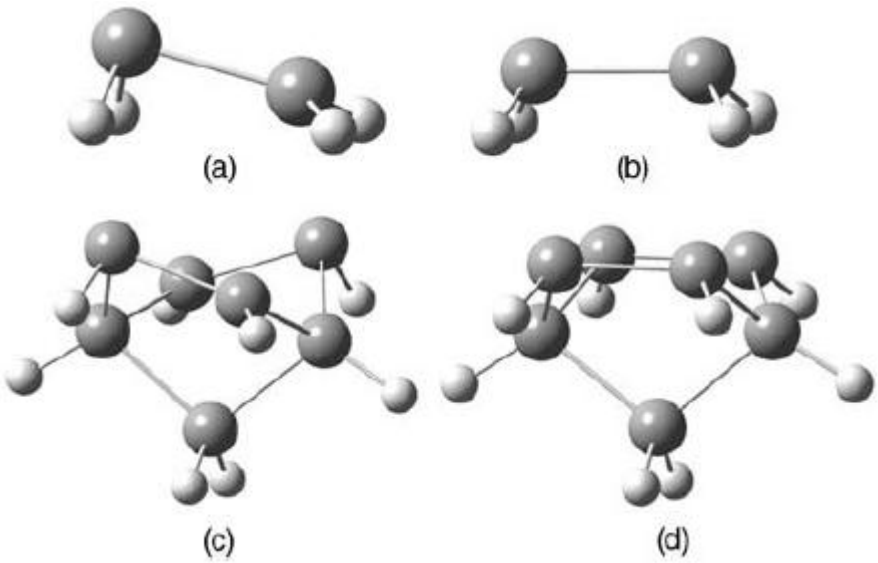

Figure 18: Cluster models employed in this study: (a) and (b), buckled and unbuckled structures for Si_2H_4; (c) and (d), buckled and unbuckled structures for Si_7H_8.

All-electron DMC calculations on the Si_2H_4 and Si_7H_8 clusters would be computationally prohibitive, especially with the need to reduce the statistical errors in the total energies to below 0.5 kcal mol^{-1}. For this reason, we have adopted the AREP pseudopotential[121-122] to model the 1s, 2s, and 2p core electrons of the Si atoms. The multi-reference calculations were also performed with the AREP pseudopotential on the Si atoms to facilitate comparison with the DMC results. The use of the pseudopotential does not significantly impact the relative energies of the planar and buckled species, as established by comparison with the results of all-electron calculations.

The active spaces for the CASSCF calculations included the π and π^* orbitals, leading to CAS(2, 2) and CAS(4, 4) spaces for the Si_2H_4 and Si_7H_8 clusters, respectively. These active

spaces were employed in the CASPT2, CASPT3, MR-ACPF, and MR-AQCC calculations, and the resulting orbitals were also employed in the MR-CC calculations.

Three different Gaussian-type orbital basis sets were used. The smallest of these, designated A, employed a 2s2p1d Gaussian-type basis set for the Si atoms,[123] and the 2s 6-31G basis set[124] for the H atoms. The intermediate basis set, designated B, employed 3s3p2d and 3s1p basis sets on the Si and H atoms, respectively. The Si atom portion of basis B was generated by adding to basis set A diffuse s and p functions with exponents of 0.0334 and 0.0230, respectively, and by replacing the single d function of exponent 0.40 with two d functions with exponents of 0.6 and 0.2. The H atom portion of basis set B was taken to be the 6-311G(d, p) basis set.[104] The largest basis set, C, was formed by adding to basis set B an f function with an exponent of 0.336 on each Si atom and is taken from the cc-pVTZ basis set.[125] The DFT calculations were carried out with the Gaussian 03 program,[126] and the HF, MP2, CCSD, CCSD(T), CASSCF, CASPT2, CASPT3, MR-ACPF, and MR-AQCC calculations were carried out using MOLPRO.[127] The MR-CC calculations were carried out using the MRCC code,[33, 115] interfaced with the MOLPRO program. The calculations with basis set C were carried out only for the single-reference methods.

The quantum Monte Carlo calculations were carried out using both Hartree-Fock and CASSCF trial functions, in both cases using basis set A. In this case, the Hartree-Fock and CASSCF calculations were carried out using the Gaussian 03 program. The trial functions were combined with four-parameter Jastrow factors of the form given by Drummond et al.[128] to deal with the electron-nuclear and electron-electron cusps. The parameters in the Jastrow factors were optimized using a variance-minimization variational Monte Carlo method. DMC calculations using the fixed-node approximation and the Slater-Jastrow trial wave-functions were

run sufficiently long to ensure that the uncertainties in the relative energies were less that ±0.8 kcal mol^{-1}. For Si_2H_4 the DMC calculations employed 4800 walkers and were run between $9x10^4$ and $3.1x10^5$ steps, and for Si_7H_8 the calculations employed 12,800 walkers and were run between $4x10^4$ and $2x10^5$ steps. Time steps ranging from 0.0015 to 0.0040 a.u. were used, and the resulting energies and error bars were extrapolated to zero time step. The fixed-node approximation was employed in the DMC calculations. The quantum Monte Carlo calculations were carried out using the CASINO program.[129]

4.3 Results

The relative energies per dimer from the various calculations are summarized in Table 5. We consider the results for the Si_2H_4 model first. With basis set A, the Hartree-Fock, B3LYP, and PW91 calculations predict the buckled species to be more stable than the planar species by 11.0, 5.8, and 4.6 kcal mol^{-1}, respectively. In contrast, with the CAS(2,2) method, the unbuckled structure is calculated to be 8.6 kcal mol^{-1} more stable than the buckled structure. As one progresses along the CASPT2, CASPT3, AQCF, and MR-ACPF sequence of methods, the energy separation between the unbuckled and buckled structures decreases, the unbuckled structure being preferred by only 2.7 kcal mol^{-1} with the MR-ACPF method. The MRCCSD calculations with basis set A also predict the unbuckled structure for Si_2H_4 to be 2.8 kcal mol^{-1} more stable than the buckled structure, with the energy difference decreasing slightly to 2.4 kcal mol^{-1} upon the inclusion of triple excitations (MRCCSDT level). For the various multi-reference methods, the unbuckled structure is stabilized relative to the buckled structure of Si_2H_4 by 1.4-1.7 kcal mol^{-1} in going from basis set A to basis set B, with the unbuckled structure being

calculated to be only 0.85 kcal mol^{-1} more stable than the buckled structure with the MRCCSDT approach. The Hartree-Fock, CCSD, and CCSD(T) relative energies are nearly the same with basis sets B and C, indicating that f functions do not play an important role for the relative energies.

For the Si_7H_8 cluster and for all three basis sets, the Hartree-Fock method favors the buckled structure over the unbuckled structure by nearly the same energy (per dimer) as found for Si_2H_4. With basis set A, dynamical correlation corrections to the CASSCF energies are found to stabilize the buckled structure relative to the unbuckled structure even more than found for Si_2H_4, with the CASPT3, MR-AQCC, and MR-ACPF calculations predicting the unbuckled structure of Si_7H_8 to be 1.4-2.0 kcal mol^{-1} per dimer more stable than the buckled structure. With basis set B, the CASPT3, MR-AQCC, and MR-ACPF calculations all predict the buckled form of Si_7H_8 to be more stable than the unbuckled form, by 0.9-1.4 kcal mol^{-1} per dimer. The MRCC calculations were not feasible for the Si_7H_8 cluster model. Again, the tests with basis set C reveal that f basis functions are not important for the relative energies.

Table 5: Relative energies (kcal/mol) per dimer for the buckled and unbuckled forms of the Si_2H_4 and Si_7H_8 clusters [a,b]

Method	Si_2H_4			Si_7H_8		
	Basis A	Basis B	Basis C	Basis A	Basis B	Basis C
RHF	-11.04	-11.41	-11.40	-10.35	-11.37	-11.10
MP2	-0.96	-2.12	-1.75	-1.03	-2.90	-2.80
CCSD	0.24	-2.27	-2.22	-1.95	-4.97	-4.92
CCSD(T)	2.15	0.31	0.39	0.25	-2.57	-2.57
B3LYP	-5.78	-6.17		-6.71	-7.64	
PW91	-4.62	-5.02		-6.69	-7.61	
CAS	8.56	7.19		6.69	3.74	
CASPT2	4.67	3.22		3.69	1.16	
CASPT3	3.51	1.79		2.00	-1.04	
AQCC	3.04	1.55		1.85	-0.95	
ACPF	2.70	1.13		1.44	-1.36	
MRCCSD	2.78	1.39		1.39		
MRCCSDT	2.43	0.85				
DMC/HF		-1.6±0.7			-2.2±0.4	
DMC/CAS		1.1±0.7			-2.2±0.4	

[a] Results obtained using the AREP pseudopotential for Si [51,52].
[b] A positive value of the relative energy refers to the situation where the unbuckled structure is more stable than the buckled structure

We now turn to the results of the DMC calculations. With the Hartree-Fock trial function, the DMC calculations predict the buckled form of Si_2H4 to be favored over the unbuckled form by 1.6±0.7 kcal mol^{-1}, but for the CAS(2,2) trial function, the order switches, and the unbuckled structure is calculated to be 1.1±0.7 kcal mol^{-1} more stable than the buckled structure. For the Si_7H_8 cluster model, the DMC calculations predict the buckled structure to be favored by 2.2±0.4 kcal mol^{-1} per dimer with both the Hartree-Fock and CAS(4,4) trial functions. At first sight, it is surprising that the relative stabilities of the buckled and unbuckled forms of Si_2H_4 obtained from the DMC/HF and DMC/CAS calculations differ appreciably, while the two approaches give the same relative energy for the two Si_7H_8 species. We believe that this is a consequence of the fact that the relative energy of the buckled and unbuckled structures as calculated with the CAS method is appreciably smaller (by 1.9-3.5 kcal mol^{-1}, depending on the basis set) for Si_7H_8 than for Si_2H_4.

The DMC/CAS calculations on the Si_7H_8 cluster model favor the buckled structure by 0.8-1.2 kcal mol^{-1} more per dimer than do CASPT3, AQCC, or the ACPF calculations with basis set B. While part of this discrepancy could be due to errors resulting from the use of the fixed-node approximation in the DMC calculations, we believe that much of the discrepancy is due to the limitations of the CASPT3, AQCC, and ACPF calculations for describing the Si_7H_8 model system. These are limitations such as the size of the active space and basis set that one can use within the computational restraints.

We note also that our DMC calculations favor the buckled structure by appreciably more than did the earlier DMC calculations of Healy et al.[87] Specifically, for their two-dimer model, the buckled structure was predicted to be 0.7±0.5 kcal mol^{-1} per dimer more stable than the unbuckled structure. Although part of the difference between the two sets of DMC results for the two-dimer case may be due to the different cluster models employed (Healy et al. used a

$Si_{15}H_{16}$ model), we believe that much of the difference is due to our use of smaller time steps and extrapolation to zero time step, leading to better converged energies. In DMC, the projection operator is $e^{-\tau H}$, where τ is the time step. In practice, this operator is approximated and its accuracy depends on the size of the time step, τ. In practice, several small time-steps are used. These time-steps must be small enough so that one can extrapolate tau- to zero. If τ is too large, the extrapolation is poor, creating an error and if the time steps are too small, the configurations in the DMC run become correlated. This also leads to an error. Using several small time-steps, helps to minimize this 'time-step error.'

4.4 Conclusion

Si_2H_4 and Si_7H_8 cluster models of the Si(100) surface have been introduced and used to calculate the relative stabilities of buckled and unbuckled structures using a wide range of electronic structure methods. In agreement with earlier studies, the CASPT2 method favors the unbuckled structure, for both the one- and two dimer models but with the buckled-unbuckled energy difference being smaller for the two-dimer model. Correlation effects beyond those recovered in the CASPT2 method stabilize the buckled structures relative to the unbuckled structures, with these high-order corrections proving to be more important for the Si_7H_8 cluster than for the Si_2H_4 cluster. For Si_2H_4, the CASPT3, MR-AQCC, and MR-ACPF calculations using the larger basis set favor the unbuckled structure by 1.0-1.8 kcal mol^{-1}, consistent with the DMC/CAS calculations which favor the unbuckled structure by 1.1±0.7 kcal mol^{-1}. For the two-dimer Si_7H_8 model, the CASPT3, MR-AQCC, MR-ACPF, DMC/CAS calculations with basis set B favor the buckled structure by 1.1-1.4 kcal mol^{-1} per dimer, whereas the DMC/CAS calculations favor the

buckled structure by 2.2±0.4 kcal mol^{-1} per dimer. These results demonstrate that dynamical correlation effects missing in the CASPT2 (and MRMP2) approaches are important in addressing the issue of the relative energies of unbuckled and buckled SiSi dimers in models of the Si(100) surface. Much of the contribution of the higher-order correlation effects is already recovered at the CASPT3 level of theory, as it shows the importance of dimer-dimer interactions in favoring the buckled structure and gives a reasonable energy difference between the buckled and flat two dimer structures. We suggest that this approach would be well suited for use in calculations employing larger, more realistic, cluster models of the buckling of the dimers on the Si(100) surface.

5. CHAPTER FIVE: Theoretical Studies of a Three Dimer $Si_{13}H_{12}$ Model of The Si(100) Surface

5.1 Introduction

Due to its importance in electronic devices, including microchips and solar cells the Si(100) surface has been the subject of numerous theoretical and experimental studies. In the late 1950's Schliar and Farnsworth[97] using LEED, found that the silicon (100) surface, generated by cleaving the crystal lattice, reconstructs to form rows of dimers. When silicon is cleaved along the (100) plane each surface atom is left in a high energy state with two dangling, or unfilled bonds. The surface reconstruction forms dimers, which eliminates a highly reactive dangling bond on each atom. Since Chadi's 1979 work suggesting that silicon dimers buckle, forming a c(4x2) surface reconstruction,[9] researchers have striven to better understand the Si(100) surface structure.

There is experimental evidence that at temperatures below ~120 K the dimers buckle in rows with either c(4x2) or p(2x2) surface periodicity.[130] Above ~120 K the dimers are flipping so as to appear in a symmetric p(2x1) reconstruction. As the dimers move from the p(2x1) structure into the buckled c(4x2) pattern, the electrons associated with the dangling bonds localize on the "up" atom, leaving an empty dangling bond on the "down" atom. The surface

buckling increases the distance between the occupied dangling bonds minimizing the surface energy.[7]

The Si(100) dimer structure has proven to be a major challenge for theory. DFT calculations, on both slab and cluster models, predict that it is energetically favorable for the surface dimers to buckle. Given the diradical character of the surface dimers, one might question the reliability of DFT for addressing the buckling problem. Indeed cluster models using CASSCF and multireference MP2 (MR-MP2) methods predict unbuckled structures.[131] Diffusion Monte Carlo(DMC) calculations on small cluster models predict buckled structures, with the energy difference between the planar and buckled structures being about half that found in the GGA DFT calculations.[87, 131]

A second interesting question, is which types of models are viable, capturing enough of the true nature of the surface to give useful information. Several studies with differing numbers of dimers and differing layers of silicon, using both periodic slab and cluster models have looked at this problem.[8, 82, 84-85, 87-89, 91, 93-95] These studies reveal that one needs methods that include both static and dynamic electron correlation, and models that capture intra-row dimer interactions. In this work, we present ROHF, CASSCF, and Quantum Monte Carlo studies of a three dimer $Si_{13}H_{12}$ model. We use this model to examine dimer-dimer interactions, electron correlation effects, and basis set effects

5.2 Theoretical Methods

To generate the three dimer $Si_{13}H_{12}$ models (Figure 19 and Figure 20), we first performed DFT(PW91) slab model optimizations employing periodic boundary conditions using the VASP

code.[69-70, 72, 132] The slab model employed five silicon layers, and eight dimers in two rows with four dimers. The bottom silicon layer was terminated with hydrogen atoms to eliminate subsurface dangling bonds. During optimization, the bottom silicon layer was fixed as were the terminating hydrogen atoms. We employed Vanderbilt's' ultra-soft pseudopotentials[62] with a plane-wave basis set with a 250 eV cutoff energy to optimize the buckled c(4x2) and flat or "symmetric", p(2x1) surface structures. We constructed the $Si_{13}H_{12}$ models, shown in Figure 19 and Figure 20, from the optimized slab structures. These three dimer clusters were used to explore the role of dimer-dimer interactions and electronic correlation in establishing the relative stability of the two structures.

Figure 19: The three dimer $Si_{13}H_{12}$ surface model cut from the optimized p(2x1) flat surface. The side view is on the left and the top view is on the right.

Figure 20: The three dimer $Si_{13}H_{12}$ surface model cut from the optimized c(4x2) buckled surface. The side view is on the left and the top view is on the right.

Using these three dimer models, we performed ROHF and CAS(6,6) calculations using the Gaussian03[126] package. The CASSCF active space was chosen to contain the π and π^* dimer orbitals. For the silicon atoms, we used Trail and Needs' AREP Dirac-Fock pseudopotential[121-122], and employed two basis set. The first basis set (b1) is a contracted Gaussian-type used in the

previous section on the one and two silicon dimer models. This basis consists of 3s3p2d functions for the silicon atoms, and 3s1p for the hydrogen. Our larger basis set (b2) is a correlation consistent basis set for use with Trail and Needs' AREP Dirac Fock pseudopotential. The larger basis set contained 5s5p4d1f functions on silicon and 5s2p functions on hydrogen. For silicon the s, p, and d functions came from the cc-pV5Z-PP basis, while the f is from his cc-pVTZ-PP basis set.[133] For hydrogen the s and p functions came from the cc-pV5Z-PP basis.[133]

The $Si_{13}H_{12}$ clusters allowed us to both compare our models with larger, more traditional cluster models and to generate trial wave-functions for use in DMC calculations. We performed the Quantum Monte Carlo calculations with the CASINO[129] program. We first performed variational Monte Carlo calculations on the Slater determinant type trial wave-functions, and then added and optimized Jastrow factors, to further improve the descriptions of particles correlations in the trial wave-functions. Each of the Jastrow factors described electron-nuclear correlations, electron-electrons correlations, and enforced the Kato cusp conditions. The Jastrow factors used with Peterson's basis set also included electron-electron-nuclear correlations. The VMC calculations generated sets of configurations/walkers that served as starting points for the subsequent DMC calculations. Theoretically, DMC is able to reproduce the exact ground state energy within the limits of the fixed-node and the pseudopotential approximations.

As shown in Table 6, our $Si_{13}H_{12}$ DMC calculations using the ROHF/b1 trial wave-function, used between 19,200 and 25,600 walkers, propagated using three time steps, for between 8,400 and 180,000 moves. For the CAS(6,6)/b1 trial wave-function, we used three time steps and between 9,600 and 25,600 walkers propagating for between 8400 and 280,000 moves. For the calculations with the larger basis set, b2, we used two time steps, and between 50,000 and 100,000 walkers propagated for at least 38,000 moves.

Table 6: Number of walkers, number of moves and time-steps for DMC calculations on the $Si_{13}H_{12}$ trimer. The DMC calculations for the trimer with Basis B2 are in progress.

Trial Wave-function	Walkers	Moves	Time Steps (a.u.)
ROHF – Flat – Basis B	25600	$1.8*10^5$, $7.83*10^4$, $1.65*10^5$	0.002, 0.0025, 0.003
CASSCF(6,6) – Flat – Basis B	25600	$2.28*10^5$, $8.4*10^3$, $2.16*10^4$	0.002, 0.0025, 0.003
ROHF – Buckled – Basis B	19200	84,000; 70,500; 84,000	0.002, 0.0025, 0.003
CASSCF(6,6) – Buckled – Basis B	9600	$1.97*10^5$, $2.8*10^5$, $1.63*10^5$	0.002, 0.0025, 0.003
ROHF – Flat – Basis B2	$1.0*10^5$	56,600	0.02
CASSCF(6,6) – Flat – Basis B2	$7.5*10^4$	14,854	0.02
ROHF – Buckled – Basis B2	$5*10^4$	38,800	0.01
CASSCF(6,6) – Buckled – Basis B2	$8*10^4$	4,000	0.01

5.3 Results and Discussion

The results are summarized in Table 7 and Figure 22: The per dimer energy difference (eV/dimer) for the buckled models minus the flat models. A negative value indicated that the buckled is more favorable. With CASSCF the stability gained by buckling noticeably increases between a one and two dimer model and seems to stabilize at two dimers. While with DMC/CASSCF buckling clearly offers more stability when adding a third dimer. Comparing the $Si_{13}H_{12}$ model with our previously used two and one dimer structures, Si_7H_8 and Si_2H_4, it is clear that the method used changes the relative favorability of the buckled versus symmetric structures. The general trend, with the methods we used, is that the buckled structure becomes more favorable as the number of dimers increases. ROHF clearly favor the buckled, while CASSCF favors the symmetric structures. Performing DMC on these results reduces the energetic differences between the buckled and symmetric structures. DMC, with an exception

for the Si_2H_4 using CASSCF/DMC, weakly favors the buckled configurations. As more dimers are added to the model, the relative DMC energy difference favoring the buckled increases.

The DMC, ROHF, PBE and B3LYP methods favor the buckled structure over the flat. One possible explanation is illustrated with a Walsh Diagram of the HOMO(π) and LUMO(π^*) orbitals of the flat and buckled dimers. Walsh demonstrated that most stable molecular geometry is the geometry that allows the occupied orbitals to have the lowest energy. In the case of the silicon trimer, when the molecule goes from flat to bent, the HOMO, HOMO-1 and HOMO-2 all move to lower energy, while the LUMO, LUMO+1, and LUMO+3 shift to higher energy. The bent configuration stabilizes the energy of the highest occupied frontier orbitals as shown in Figure 21. This implies that changes in the atomic orbitals' overlap when going from the planer to bent configuration lowering the energy of occupied orbitals helps to stabilize the buckled structure.

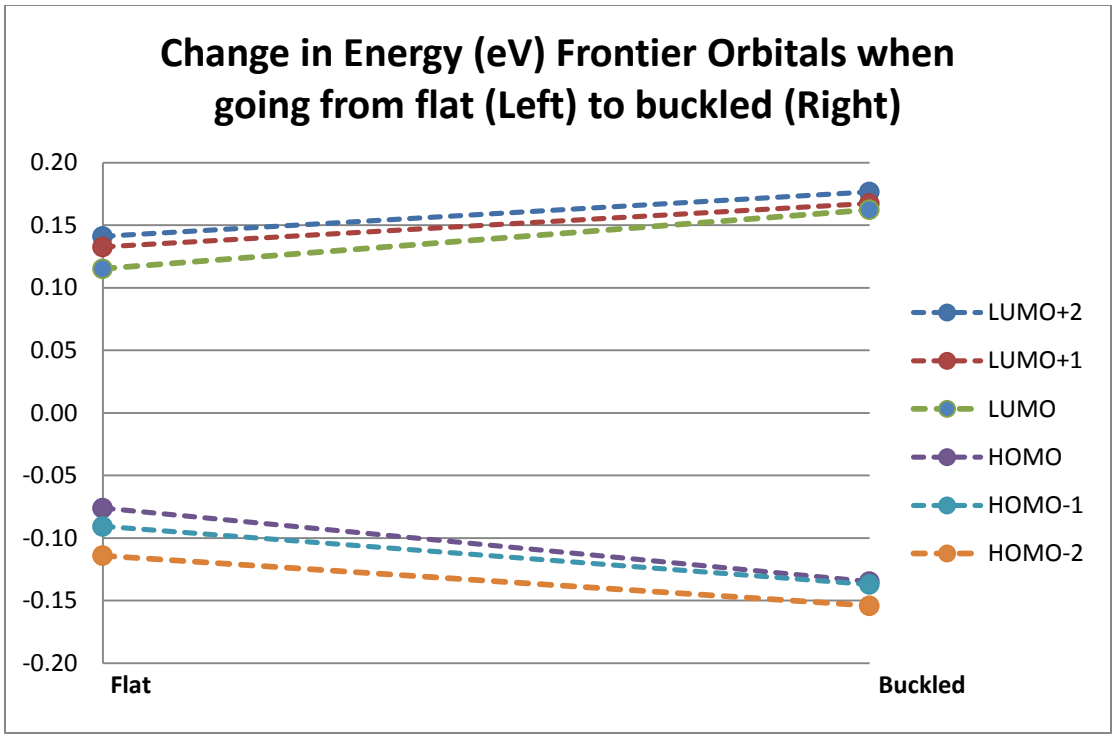

Figure 21 : Walsh diagram showing the change in energy of the frontier orbitals of $Si_{13}H_{12}$ when going from the planer to the buckled structure. The dashed lines are a guide to the eye.

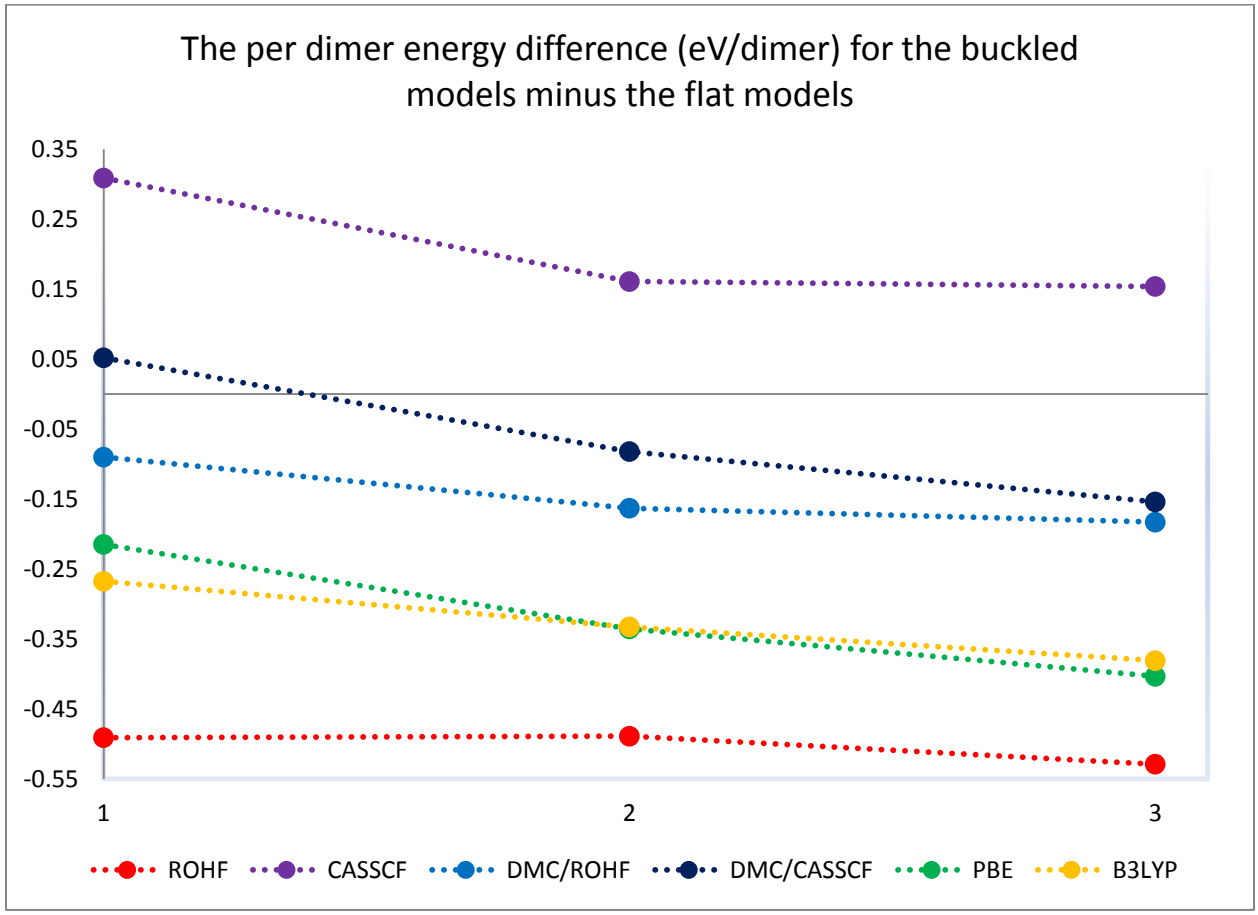

Figure 22: The per dimer energy difference (eV/dimer) for the buckled models minus the flat models. A negative value indicated that the buckled is more favorable. With CASSCF the stability gained by buckling noticeably increases between a one and two dimer model and seems to stabilize at two dimers. While with DMC/CASSCF buckling clearly offers more stability when adding a third dimer. The dashed lines are a guide for the eye.

Focusing on the $Si_{13}H_{12}$ models using basis 'b1', the ROHF method favors the buckled structure by −0.529 eV/dimer. This energy difference is more favorable than that of the DFT and DMC methods. ROHF/b1 includes as part of the exchange energy, Fermi correlation, which prevents electrons of the same spin from getting too close to each other. Since ROHF contains no static correlation and a limited description of electron correlation, it is not surprising that ROHF favors the buckled dimers the most. Nor is it surprising that that each size cluster favors

the buckled dimer by similar amounts per dimer. Looking at the CASSCF results for the $Si_{13}H_{12}$ cluster, the active space includes the π and π* orbitals of each dimer. The results with both basis sets favor the flat structure. CASSCF captures the static electron correlation needed to describe the biradical nature of the flat dimers, but with the active space used does not include dynamic electron correlation. As with earlier work using CASSCF, the flat three dimer model is negligibly less favored than the flat two dimer model[131]. Adding a second dimer substantially reduces the favorability of the symmetric structure, but adding a third has little effect on the per dimer energy difference.

Moving to the DMC results, with the ROHF/b1 trial wave function the buckled structures for the three dimer and two dimer models are −0.183 and −0.163 eV/dimer lower in energy than the flat structure. With basis 'b1' there is a substantial gain in energy when moving from the one-dimer to the two dimer model.

For the results of DMC with CASSCF trial wave-functions for the $Si_{13}H_{12}$ clusters the stability gained by buckling is greater than with the smaller Si_7H_8 and Si_2H_4 clusters. The CASSCF trial wave-function fully correlates the π and π* orbitals capturing static electron correlation, while the DMC calculation recovers energy from dynamic electron correlation that helps to stabilize the buckled structure. The DMC/CASSCF results also show probable energy trends that occur as dimer interactions increase. The intra-row dimer interactions on Si(100) appear to play an important role in stabilizing the buckled structure. Buckling maximizes the distance between areas of charge density localization on the dimers. For the DMC/CASSCF/b1 results, adding a second dimer causes the buckled structure to be favored over the symmetric and changes the per dimer energy difference by about 0.13 eV/dimer.

Table 7: Energy differences (eV/dimer) between the buckled and unbuckled Si2H4, Si7H8 and Si13H12 models with basis b1, and the larger basis b2 for Si13H12. A negative value indicates that buckled structure is more stable

Model	ROHF	CASSCF	DMC/ROHF	DMC/CASSCF	PBE	B3LYP
Si_2H_4	-0.491	0.309	-0.090	0.052	-0.215	-0.267
Si_7H_8	-0.489	0.161	-0.163	-0.082	-0.336	-0.333
$Si_{13}H_{12}$	-0.529	0.154	-0.183	-0.154	-0.403	-0.381
$Si_{13}H_{12}$ (Basis Set B2)	-1.833	0.143	-0.805			

These results parallel what is expected from results on slab calculations, and highlight the importance of adequate inclusion of electron correlation. They also stress the importance of a high quality nodal surface used for DMC trial wave-functions. The quality of the nodal surface is improved both by the choice of the electronic structure method and basis set used to generate the trial wave-function. Comparing the results from the ROHF, CASSCF, DMC/ROHF, and DMC/CASSCF for the $Si_{13}H_{12}$ cluster, it appears that basis set 'b2' allows each method to capture more of the electronic wave-function, within the limits of the method, than basis 'b1' captures. ROHF with only the electron correlation present in exchange, favors the buckled structure. Including static electron correlation in the CASSCF calculations favors the flat. The multi-determinant nature of CASSCF allows it to effectively capture the near degeneracies in the low-lying orbitals, the static electron correlation needed to stabilize the biradicaloid dimer. The DMC calculations including both static and dynamic correlation needed to accurately portray

both the buckled and flat structures; confirm the importance of including both aspects of electron correlation when comparing the ground state energy of the dimers. It is interesting to note that in the CASSCF results, there is a pair wise interaction between two adjacent dimers, that adds relative stability to the buckled structure and that this interaction converges with two dimers. Adding a third dimer has little effect on the relative stability of the structures. It is also interesting that the ROHF relative per dimer energy favoring the buckled over the flat, decreases or stays the same when adding a second dimer, and then increases when adding a third dimer to the models.

5.4 Conclusion

We have performed ROHF, B3LYP, PBE, CASSCF, and QMC calculations using both ROHF and CASSCF trial wave-functions and two different sized basis sets on a three dimer $Si_{13}H_{12}$ model. We confirm that dimer-dimer interactions play an important role in stabilizing the buckled dimer structure over the flat and that adding a third dimer provides additional stability to the buckled structure. Although, for CASSCF, which stresses static electron correlation, the impact of adding a third dimer on the relative favorability of either configuration is minimal. This is expected as methods stressing only static electron correlation favor symmetric dimers. Energy differences in CASSCF converged with two dimers; while QMC continues to make energetic gains favoring the buckled structure as a third dimer is added.

Our results show that a three dimer model can be used to model the silicon (100), and they hint that the more accurate the wave-function and method used to study the dimers, the more important multi-dimer surface models become.

6. CHAPTER SIX: Theoretical Methods for Exploring the Interaction of CO_2 with Rutile and Anatase Cluster Models

6.1 Introduction

There is much interest in the photocatalytic properties of the rutile and anatase forms of titanium dioxide, TiO_2. Reactions using CO_2 as a reactant are of commercial and ecological importance as they remove this greenhouse gas from the atmosphere and convert it to useful products such as methane, methanol, formaldehyde, and formic acid.[134-140] Even though the solar catalyzed reduction of CO_2 facilitates its reaction with H_2O and O_2 into commercially useful products, the reaction is inefficient and incompletely understood.[2, 17] It is believed that when sunlight in the long *UV* range strikes TiO_2 it can photoexcite electrons from the valance band to the conduction band, creating photo-excited electron/hole pairs.[2, 17] The holes are then able to accept electrons from molecules such as H_2O or O_2, while the photo-excited electrons can transfer from the TiO_2 catalyst to adsorbates, such as CO_2.[2, 17] Multi-step reactions, such as this, that involve electron and proton transfer, breaking C—O bonds and storing chemical energy in C—H and other bonds[51] are complex and difficult to study. An important step towards understanding these reactions is improving our knowledge of the nature of the interaction between CO_2 and TiO_2. To understand this interaction we must first know which methods are appropriate for studying it and how to construct models that give us reliable results. In this paper, we evaluate multiple

theoretical methods and different size clusters to determine which methods and model designs give us reliable results.

We explore the changes in this interaction energy for different surface planes, cluster sizes, binding sites, and surface in the presence of a bridging oxygen defect. We performed ground state studies using RHF, CCSD,[112] CCSD(T),[113] df-MP2,[38, 141] B3LYP,[117-119, 142] PBE,[47] and have van der Waals corrected PBE,[143] RPA,[144-145] and rPT2[146] calculations in progress to both better understand the interaction and determine which methods are suitable for studying this system. We use Absolutely Localized Molecule Orbital Energy Decomposition Analysis, ALMO-EDA,[147] to look at charge transfer (CT) between CO_2 and TiO_2. In the following sections, we first describe the methods and cluster models we used, and then proceed to discuss our results.

6.2 Theoretical Methods

6.2.1 Cluster Models

We denote our TiO_2 anatase clusters, shown Figure 23, Figure 24, and Figure 25 as: a(010)$Ti_2O_9H_{10}$, b(001)TiO_5H_6, c(101)$Ti_6O_{21}H_{18}$, d(001)$Ti_6O_{21}H_{18}$, e(010)$Ti_6O_{20}H_{18}$ and f(010)$Ti_6O_{20}H_{18}$ ('e' and 'f' are the same cluster with two different binding configurations of CO_2), g(010)$Ti_6O_{21}H_{18}$, and i(110)$Ti(OH)_4$. For our rutile cluster, we consider three different CO_2 binding geometries: h(110)$Ti_7O_{27}H_{28}$-CO_2, j(110)$Ti_7O_{27}H_{28}$-CO_2 and k(110)$Ti_7O_{27}H_{28}$-CO_2, shown in Figure 26. The anatase clusters model CO_2's interaction on unreconstructed surfaces. Clusters 'a', 'e', 'f', and 'g' model the (010) surface, cluster 'c' the (101) surface, clusters 'b'

and ‘d’ the (001) surface, and ‘i’ the (110) surface. The rutile clusters, ’h’, ’j’ and ’k’ model CO_2’s interaction with the (110) reconstructed rutile surface.

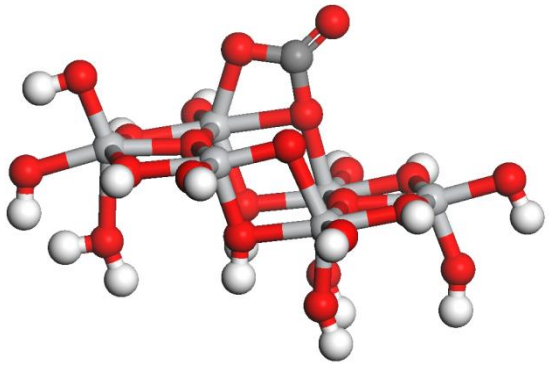

Figure 23: Anatase (101) cluster c(101)$Ti_6O_{21}H_{18}$-CO_2

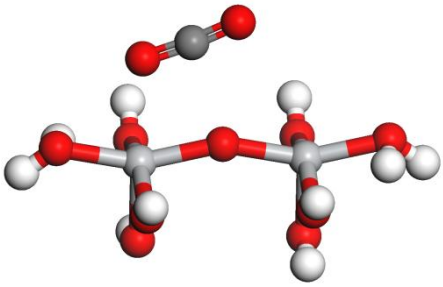

(1) a(010)$Ti_2O_9H_{10}$-CO_2

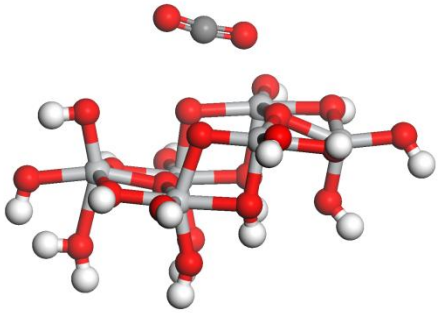

(2) g(010)$Ti_6O_{21}H_{18}$-CO_2

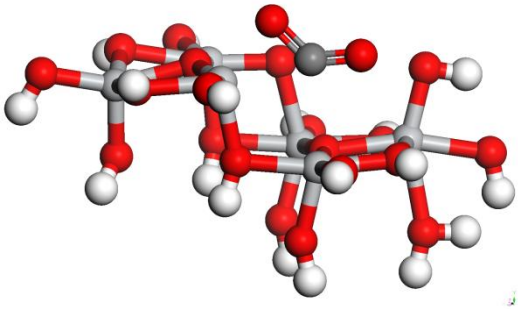

(3) e(010)Ti_6 (Vo)-5cCO_2-bent

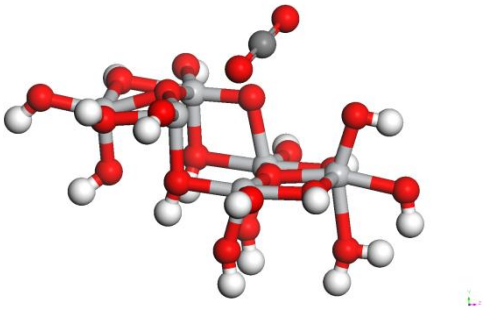

(4) f(010)Ti_6(Vo)-5cCO_2-linear

Figure 24: The three clusters modeling the (010) surface: The two stoichiometric clusters with CO_2 (1) a(010)$Ti_2O_9H_{10}$-CO_2 and (2) g(010)$Ti_6O_{21}H_{18}$-CO_2. (3) e(010)Ti_6 (Vo)-5cCO_2 and (4) f(010)Ti6(Vo)-5cCO_2 show CO_2 adsorbed with (3) bent and (4) linear geometries on a cluster with a bridging oxygen vacancy.

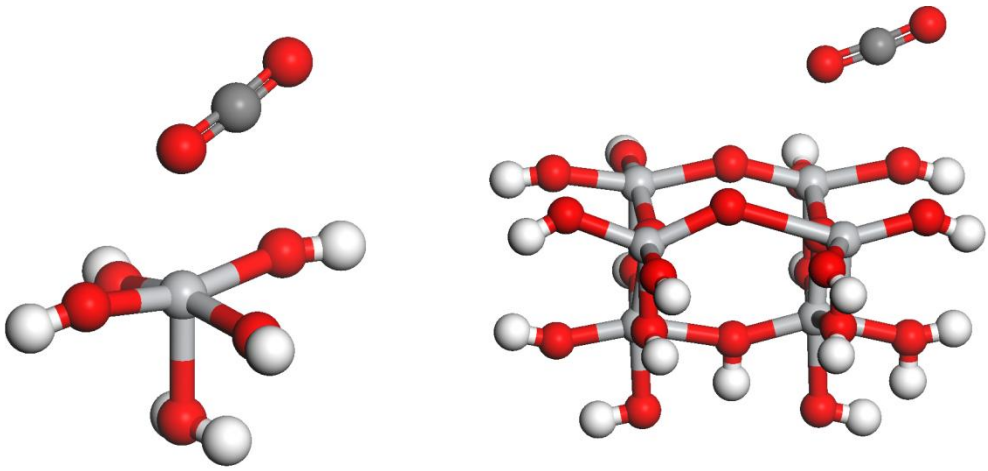

(1) b(001)TiO_5H_6-CO_2 (2) d(001)$Ti_6O_{21}H_{18}$-CO_2

Figure 25: CO_2 adsorbed on the two clusters from the (001) surface: the single Ti atom cluster (1) b(001)TiO_5H_6-CO_2 and the six Ti atom cluster (2) d(001)$Ti_6O_{21}H_{18}$-CO_2

For the most stable anatase surface, the (101) plane, we used a six Ti atom cluster, c(101)$Ti_6O_{21}H_{18}$, Figure 23: Anatase (101) cluster c(101)$Ti_6O_{21}H_{18}$-CO_2. On 'c', CO_2 bonds in a bent configuration to a Ti-5c surface atom and a two-coordinated O atom. For the (010) surface, we studied CO_2's interaction with two stoichiometric clusters: a(010)$Ti_2O_9H_{10}$, Figure 24(1); and g(010)$Ti_6O_{21}H_{18}$, shown in Figure 24(2), along with a non-stoichiometric cluster containing a bridging oxygen vacancy (V_O). We found two CO_2 binding configurations, a bent configuration, e(010)$Ti_6O_{20}H_{18}$-CO_2, Figure 24(3), and an almost linear binding configuration f(010)$Ti_6O_{20}H_{18}$-CO_2, Figure 24(4). For the (001) anatase surface, we used a single Ti atom cluster model b(001)TiO_5H_6, Figure 25(1); and a larger cluster, d(001)$Ti_6O_{21}H_{18}$, Figure 25(2). Finally we used one (110) anatase cluster model, i(110)$Ti(OH)_4$, Figure 26, in our study.

We explored (110) rutile-CO_2 interactions by looking at three different CO_2 binding sites, as shown in h(110)$Ti_7O_{27}H_{28}$-CO_2, Figure 27(1), j(110)$Ti_7O_{27}H_{28}$-CO_2, Figure 27(2) and k(110)$Ti_7O_{27}H_{28}$-CO_2, Figure 27(3). The rutile $Ti_7O_{27}H_{28}$-CO_2 complexes are from work by Falcetta and Jordan.[148] The anatase clusters and initial CO_2 locations are based on cluster used by Indrakanti, Schobert, and Kubicki.[2, 17]

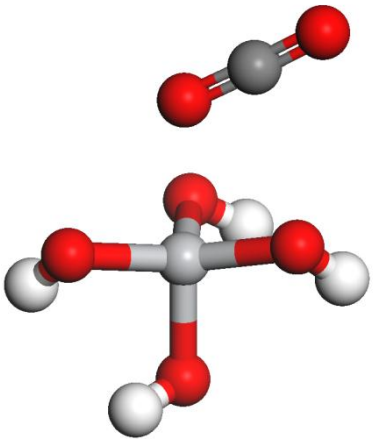

i(110)TiO4H_4-CO_2

Figure 26: Cluster i(110)TiO4H_4-CO_2 modeling the (110) anatase surface.

For anatase we froze the Ti and O atoms while optimizing the H-O bond lengths at the DFT/B3LYP[117, 119] level of theory, as implemented in Molpro 2009 and.[127, 149] For the O and H atoms we used the cc-pVDZ basis, VDZ[125, 150-151] and for the Ti atoms we used the cc-pVDZPP, basis set and effective core potential.[133] We optimized the geometry of CO_2 in Molpro 2009 using coupled cluster with single, double and perturbative triple excitations, CCSD(T),[113] and the cc-pVTZ basis set.[125, 150-151] We then used DFT/B3LYP with cc-pVDZ/cc-pVDZPP to optimize CO_2's geometry and position in the presence of the frozen surface models.

6.2.2 Ground State Methods

We calculated the interaction energies between the TiO_2 clusters and CO_2 as, $E_{int} = E_{\mathrm{TiO2CO2}} - E_{\mathrm{CO2}} - E_{\mathrm{TiO2}}$ and used the method of Boys and Bernardi [152] to obtain the counterpoise corrected binding energies, $E_{binding(cp)}$. To calculate the binding energies between CO_2 and the TiO_2 clusters, we used both DFT and wave-function based methods: RHF, df-MP2, CCSD, CCSD(T), B3LYP, and PBE in Molpro 2009, 2012. We performed PBE, dispersion corrected PBE using the method developed by Tkatchenko and Scheffler (TS-vdw-PBE)[143], RPA, and rPT2 as implemented in FHI-aims.[153] The rPT2 method is RPA plus the renormalized single excitation correction (rSE)[154-155] and the second order screened exchange correction (SOSEX).[146, 156-157] Since MP2 can run into problems, it overestimates the induction and dispersion portions of the binding energy while underestimating electron correlation, we tested the validity of MP2 for CO_2-TiO_2 complexes, by comparing results with CCSD(T) on clusters b(001)TiO_5H_6 and i(110)TiO_4H_4. We found that the MP2 energies were lower in energy than CCSD(T) by 1 meV for cluster 'b' and 23 meV for cluster 'i'.

For our RHF, df-MP2, CCSD, CCSD(T), B3LYP, and PBE calculations done in Molpro, we used the aug-cc-pVTZ and cc-pVTZ basis sets on C, O, and H atoms; and the aug-cc-pVTZPP and cc-pVTZPP basis sets and pseudopotential on Ti atoms. The combination of aug-cc-pVTZ and aug-cc-pVTZPP we abbreviate as AVTZPP, while we abbreviate the combination of the cc-pVTZ and cc-pVTZ as VTZPP. We used the 'tier 2' basis set for the PBE, TS-PBE, RPA, and rPT2 calculations. The 'tier 2' basis gives results similar in quality to a triple zeta basis set.

Our density functional based methods include B3LYP, PBE, along with the van der Waals corrected PBE using the method of Tkatchenko and Scheffler. DFT using traditional

functionals fails to include dispersion; because it incorrectly describes the long-range interactions necessary for accurate dispersion energies. Previous works[158-159] have shown that dispersion corrections are important when describing TiO_2-CO_2 interactions. Traditional functionals fail to accurately describe structure or binding in van der Waals complexes, such as noble gas clusters. TS-VdW/DFT uses Hirshfeld partitioning of the charge density to determine the C_{ij}^6 and R_i^6 terms used to correct the dispersion energy.[160] RPA is similar to couple cluster theory, and rPT2, which includes a renormalized single excitations correction to improve the description of dispersion and strong electrostatic interactions,[146] and a second order screened exchange correction to improve the description of strong electrostatic interactions.[146] The rPT2 is able to describe dispersion energy as it captures electron exchange and non-local electron correlations.[146]

6.2.3 Energy Decomposition Analysis

To understand the nature of the energetic interactions in the TiO_2-CO_2 complexes, we performed ALMO-EDA as implemented in Q-Chem[161-162] at the RHF level of theory. We used the LanL2DZ basis set and pseudopotential on Ti atoms.[163-165] We used the aug-cc-pVTZ[125, 150-151, 166] basis for the C, O, and H atoms in the one and two Ti atom complexes a(010)$Ti_2O_9H_{10}CO_2$, b(001)$TiO_5H_6CO_2$, and i(110)$Ti(OH)_4CO_2$. For the larger clusters we used aug-cc-pVDZ[125, 150-151, 166] on C and O and cc-pVDZ[125, 150-151, 166] on H atoms. Earlier work, proposed that the binding between CO_2 and TiO_2 involved the transfer of photo-excited electrons from TiO_2's valence band to CO_2's unoccupied orbitals, creating a $CO_2^{\cdot-}$radical anion.[2, 17, 167] The ALMO-EDA method separates charge transfer energy from the induction and polarization energies, allowing us to look at charge-transfer between TiO_2 and CO_2. The charge transfer energy, E_{CT} is

the lowering in energy of the system caused by the movement of electrons from an occupied orbital of one monomer to a virtual orbital of another[147]. Charge transfer is also a measure of the covalency of a chemical bond, as it does not occur in purely ionic complexes. Along with charge transfer, ALMO-EDA calculations decompose the binding energy into geometrical distortion energy, frozen density energy and polarization.[147]

$$E_{bind} = E_{\mathrm{GD}} + E_{\mathrm{FRZ}} + E_{\mathrm{POL}} + E_{CT} \quad (46)$$

The geometrical distortion energy, E_{GD}, is the energetic penalty for geometrically distorting CO_2 and TiO_2 from their low-energy free geometries into the geometries they assume in the complex.[147] The frozen density term, E_{FRZ}, arises from the interaction of the unrelaxed electron densities on the isolated individual monomers, CO_2 and TiO_2,[147] in their bound complex geometries. That is the electron densities match those of free CO_2 and TiO_2. The polarization energy, E_{POL}, is the energy lowering due to intra-molecular relaxation of the molecular orbitals on CO_2 and TiO_2 in the presence of each other's electric field.[147] The ALMO-EDA and other variational energy decomposition schemes calculate the E_{POL} differently than perturbation schemes such as SAPT.[147] Charge transfer is accompanied by a decrease in energy, this is described by a Roothaan Step correction to the converged ALMO results[147]. That is it describes the contribution from the occupied orbitals of monomer one (two) to the virtual orbitals of monomer two (one), $E_{1\to2}^{RS}$ ($E_{2\to1}^{RS}$).[147] While a third higher order term describing the induction effects associated with charge transfer is denoted as E^{HO}.[146] In this work, we focus on the frozen density, polarization, and charge transfer terms.

6.3 Results and Discussion

6.3.1 Anatase CO_2 Results

The binding energies for the clusters are listed in Table 8 and Table 9 and the binding geometries for CO_2 are listed in Table 13 at the end of this section. For the Ti_6 clusters, at the df-MP2 level, the binding energy is two to three times larger when CO_2 absorbs in a bent configuration, on 'c' and 'e', compared to a linear configuration on 'd', 'f', and 'g'. For e(010)$Ti_6O_{20}H_{18}$-V_o-CO_2, the complex with the greatest df-MP2 binding energy, CO_2's carbon atom adsorbs over the nucleophillic bridging oxygen vacancy, while one of CO_2's oxygen atoms interacts with an adjacent electrophillic titanium atom. For c(101)$Ti_6O_{21}H_{18}$-CO_2, the complex with the second largest df-MP2 binding energy, CO_2 binds in a bent geometry. Its carbon atom interacts with the bridging oxygen, while one its oxygen atoms interacts with a Ti-5c atom. When CO_2 changes from a linear to a bent geometry, its orbital hybridization changes from sp^2 to sp^3. This orbital re-hybridization is accompanied by an electron transfer from TiO_2 to CO_2. The binding energy is largest when CO_2 absorbs in a bent configuration, as on e(010)$Ti_6O_{20}H_{18}$-Vo and c(101)Ti_6-5c, as measured with the methods we used. At the df-MP2 level the binding energy is 1.1 eV larger for the cluster with the V_O, e(010)$Ti_6O_{20}H_{18}$-V_o, than for c(101)$Ti_6O_{21}H_{18}$. For B3LYP, PBE, and van der Waals corrected PBE; CO_2 binds between 0.2 and 0.5 eV more strongly to 'e' than to 'c'. Indrakanti et al.,[2] also found that the bent CO_2 geometry had the largest binding energy for 'e'. Their binding energy for 'e' at the B3LYP/def2-SV(P) level is -1.275 eV {Indrakanti, 2009 #119}. Our counterpoise corrected B3LYP/AVTZPP(VTZPP) binding energy for 'e' is -1.823 eV (1.784 eV). We attribute this difference to our use of a more complete basis set incorporating diffuse functions, which are needed to accurately model binding energies.[32] At the

df-MP2 level our binding energy for ’e’ is -2.487 eV (2.362 eV) using the AVTZPP (VTZPP) basis set and pseudopotential. This is substantially larger than their B3LYP and RHF binding energies for ‘e,’ showing the importance of using methods that treat dispersion interactions. Sorescu, Al-Saidi and Jordan, using slab models of the anatase (101) surface, also found dispersion corrections to play an important role for TiO_2-CO_2 interactions.[168] As compared to PBE, and TS-vdW/PBE, df-MP2 binding energy for ’e’ is still greater, but closer to the PBE, and TS-vdW/PBE binding energies. Taking into account, that df-MP2 tends to overestimate dispersion, the energy differences highlight the importance of an accurate description of dispersion. This hints at the importance of both method and basis set completeness when describing TiO_2-CO_2 systems. Indrakanti et.al. found a triplet ground state for ’e.’ We found the singlet to be lower in energy than the triplet state. Cheng and Selloni,[169] using DFT+U found that anatase with subsurface defects could have either an open shell singlet or triplet ground state depending on the value of the ‘U’ parameter. Give the sensitivity of the system to the value of the ‘U’ parameter, it would be interesting to look at the singlet-triplet gap for (101) defective anatase surface.

Table 8: RHF, DF-MP2, CCSD, CCSD(T), B3LYP, PBE (as implemented in Molpro), PBE (as implemented in FHI-aims), TS-vdw-PBE, and RPA counterpoise corrected binding energies in eV. For the RHF, DF-MP2, CCSD, CCSD(T), B3LYP and PBE calculations we used the aug-cc- pVTZ basis set on C, O, and H atom; and the aug-cc-pVTZ(PP) basis and ecp on Ti atoms. At the df-MP2 level, we Correlated 3s and 3p semicore Ti electrons for clusters a, b, i, h, j and k. For clusters b and i we correlated Ti's 3s and 3p electrons at the CCSD and CCSD(T) levels.

$E_{binding(cp)}$ (eV)	RHF	DF-MP2	CCSD	CCSD(T)	B3LYP	PBE
a(010)$Ti_2O_9H_{10}CO_2$	-0.403	-0.403			-0.248	-0.242
b(001)$TiO_5H_6CO_2$	-0.325	-0.409	-0.428	-0.432	-0.235	-0.244
c(101)Ti_6-5cCO_2	-2.389	-1.481			-1.645	-1.555
d(001)$Ti_6O_{21}H_{16}$	-0.151	-0.271			-0.121	-0.145
e(010)Ti_6(Vo)-5cCO_2-bent	-1.507	-2.487			-1.823	-2.068
f(010)Ti_6(Vo)-5cCO_2-linear	-0.362	-0.751			-0.488	-0.539
g(010)Ti_6-5cCO_2	-0.596	-0.730			-0.482	-0.457
i(110)Ti(OH)4CO_2	-0.144	-0.247	-0.234	-0.248	-0.105	-0.116
h(110)Rutile $Ti_7O_{27}H_{27}CO_2$	-0.022	-0.153			-0.013	-0.058
j(110)Rutile $Ti_7O_{27}H_{27}CO_2$	-0.153	-0.368			-0.110	-0.141
k(110)Rutile $Ti_7O_{27}H_{27}CO_2$	-0.159	-0.457			-0.116	-0.171

Table 9: RHF, DF-MP2, CCSD, CCSD(T), B3LYP, and PBE counterpoise corrected binding energies in eV using the cc-pVTZ basis set on C, O, and H atom; and the cc-pVTZ(PP) basis set and ECP on Ti atoms. At the df-MP2 level, we correlated 3s and 3p semi-core Ti electrons for clusters a, b, i, j, and k. For clusters 'b' and 'i' we correlated Titanium's 3s and 3p electrons at the CCSD and CCSD(T) levels.

$E_{binding(cp)}$ (eV)	RHF	DF-MP2	CCSD	CCSD(T)	B3LYP	PBE
a(010)$Ti_2O_9H_{10}CO_2$	-0.385	-0.338	-0.379		-0.257	-0.257
b(001)$TiO_5H_6CO_2$	-0.310	-0.348	-0.368	-0.360	-0.222	-0.231
c(101jjTi_6-5cCO_2	-2.351	-1.385			-1.616	-1.525
d(001)Ti_6O_{21}H16	-0.141	-0.187			-0.115	-0.138
e(010)Ti_6(Vo)-5cCO_2-bent	-1.416	-2.362			-1.784	-2.030
f(010)Ti_6(Vo)-5cCO_2-linear	-0.354	-0.692			-0.481	-0.531
g(010)Ti_6-5cCO_2	-0.708	-0.526			-0.468	-0.445
i(110)Ti(OH)4CO_2	-0.141	-0.209	-0.208	-0.215	-0.104	-0.115
h(110)Rutile $Ti_7O_{27}H_{27}CO_2$	-0.023	-0.146			-0.015	-0.059
j(110)Rutile $Ti_7O_{27}H_{27}CO_2$	-0.148	-0.330			-0.106	-0.136
k(110)Rutile $Ti_7O_{27}H_{27}CO_2$	-0.154	-0.406			-0.111	-0.168

For c(101)$Ti_6O_{21}H_{18}$, Indrakanti et al., found CO_2 linearly absorbed with a B3LYP binding energy of -0.34 eV. Our B3LYP/AVTZPP single point binding energy, -1.645 (-1.616) eV, is approximately five times larger. We believe that using the larger basis set and the small core pseudopotential, VDZPP versus 3-21G to optimize CO_2's geometry, allowed our optimization to reach a bent geometry. Ideally, due to the partial radical nature of CO_2, one would prefer to use a larger basis including diffuse functions. Other researchers also found a bent CO_2 geometry for

their anatase (101) models. Curtiss et al.,[167] found both bent and linearly absorbed CO_2 for their (101) PBE slab and B3LYP/6-31+G(2df,p) cluster models. Using a (101)$Ti_7O_{27}H_{27}$ cluster they found that the bent CO_2 is more stable than linearly absorbed CO_2, -0.41 eV verses -0.34 eV. Interestingly they found the converse true for their slab model, -0.14 compared to -0.20 eV. While they did use diffuse functions, they used a smaller basis set and did not account for basis set superposition error (BSSE). Accounting for BSSE could cause the bent geometry to become energetically more favored. Sorescu, Al-saidi, and Jordan found both linear and bent CO_2 with vdw-PBE/slab model calculations,[168] with linear geometries most stable on the oxidized surface and bent forms most stable on the defective surface.[168]

Our third largest CO_2 binding energy is that of linearly bound CO_2 on the oxygen deficient (010) cluster, f(010)$Ti_6O_{20}H_{18}$-V_O. Indrakanti et al. found this to be the second most stable complex with a B3LYP binding energy of -0.60 eV. Our B3LYP, RHF, df-MP2, and PBE AVTZPP (VTZPP) counterpoise corrected binding energies are, shown in Table 8 (Table 9). The basis set superposition error causes CO_2 to over bind by ~0.1 eV. Comparing the two basis sets, using diffuse functions captures approximately 0.06 eV of the binding energy.

Next, we discuss the effects from changing the size of anatase clusters cut from the same surface plane. Looking at the (001) clusters b(001)TiO_5H_6 and d(001)$Ti_6O_{21}H_{16}$, we see CO_2 binds with a similar geometry, but the binding energy is greater for b(001)TiO_5H_6 than for the larger six atom cluster. Therefore either CO_2 interacts with the hydrogen atom or repulsive interactions must occur between CO_2 and atoms further away in d(001)$Ti_6O_{21}H_{18}$-CO_2 Interestingly, Sorescu and coworkers found that the binding energy decreased as they added layers in their slab convergence calculations.[168]

Looking at our (010) anatase clusters 'a' and 'g', CO_2 absorbs with similar geometries on the two Ti atom cluster a(010)$Ti_2O_9H_{10}$ and six Ti atom cluster g(010)$Ti_6O_{21}H_{18}$. Its binding energy increases as the cluster size increases, the opposite trend from the (001) models. This has been attributed to CO_2 interacting with a capping H atom on the smaller cluster.[168] It is interesting and as expected to note that both the small clusters b(001)TiO_5H_6 and a(010)$Ti_2O_9H_{10}$ yield reasonably accurate CO_2 binding geometries on the anatase models, despite the discrepancy in binding energy.

6.3.2 Rutile CO_2 Results

To study CO_2 rutile interactions, we used RHF, df-MP2, B3LYP and PBE in Molpro; and are in the process of using vdw-TS-PBE and RPA from FHI-aims to explore three different binding configurations of CO_2 on our (110) rutile $Ti_7O_{27}H_{27}$ cluster. The counterpoise corrected binding energies are shown in Table 8 and Table 9. We found with all methods using the AVTPP and VTZPP basis set and pseudopotential that the binding energy is weakest for in h(110) $Ti_7O_{27}H_{27}$ CO_2, where CO_2 absorbs parallel to the cluster surface and bridging oxygen rows, with its carbon located 3.9 Å over a five coordinated Ti atom (Ti-5c), Figure 27(a). At this distance, the CO_2 is too far away from the surface and its binding energy, even with dispersion corrections, is too small to be considered 'bonded.'

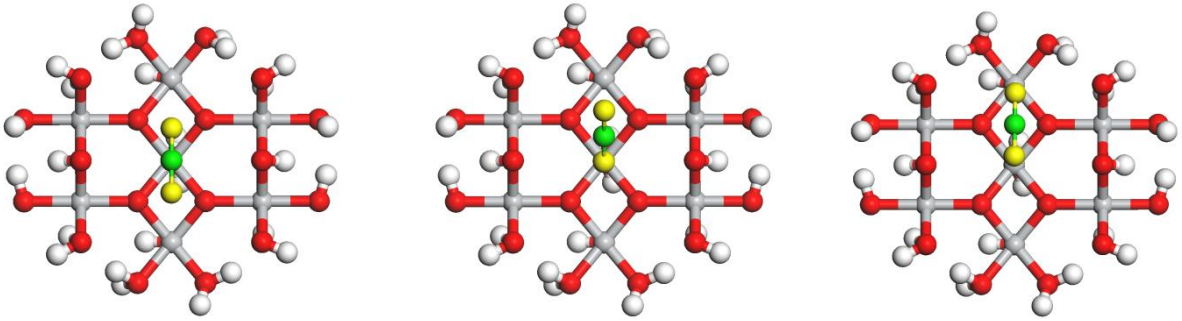

(a) h(110)Rutile $Ti_7O_{27}H_{26}$ CO_2 (b) j(110)$Ti_7O_{27}H_{26}$-CO_2 (c) k(110)$Ti_7O_{27}H_{26}$-CO_2

Figure 27 : The rutile (110) cluster with the three binding configurations (1) h(110)Rutile $Ti_7O_{27}H_{26}$ CO_2 , (2) j(110)$Ti_7O_{27}H_{26}$-CO_2 and (3) k(110)$Ti_7O_{27}H_{26}$-CO_2. The oxygen atoms on CO_2 are yellow and carbon is green.

On h(110)$Ti_7O_{27}H_{27}$ CO_2, the RHF, df-MP2, B3LYP and PBE binding energies for the AVTZPP (VTZPP) basis are -0.022 (-0.023), -0.153 (-0.146), -0.013 (-0.015), and -0.058 eV(-0.059). Wu and coworkers using Car-Parinello DFT with the PBE functional, also found a very small binding energy of -0.15 eV[170] for CO_2 on the (110) rutile surface. Temperature programmed desorption work by Thompson, Diwald and Yates found binding energies of 0.5 eV for the oxidized surface,[21] while Funk and Burghaus using Temperature desorption spectroscopy found a binding energy of 0.37 eV on the stoichiometric surface.[26]

We found that the next largest binding energy, j(110)$Ti_7O_{27}H_{27}$-CO_2, has CO_2 adsorbed in a linear angled configuration with one of its oxygen atoms tilted towards a Ti-5c atom. For the CO_2 binding configuration in j(110)Rutile $Ti_7O_{27}H_{27}$ CO_2 using the AVTZPP(VTZPP) basis and pseudopotential, the RHF, df-MP2, B3LYP, and PBE binding energies are -0.153 (-0.148), -0.368 (-0.330), -0.110 (-1.06), and -0.141 (-0.136) eV, respectively. Our angled binding configuration 'j' is similar to binding configuration angled from the surface, labeled 'I', found by Sorescu, Al-Saidi, and Jordan.[158] They found the O in CO_2 adsorbed directly over a Ti-5c atom, while ours is between two Ti-5c atoms, but clearly closer to one. They found a binding energy

of -0.44 eV using TS-vdw-PBE, and -0.39 eV using PBE-D[158] with a 15 layer slab. Our df-MP2 binding energy of -0.368 eV, is similar to theirs, while our values for RHF, B3LYP and PBE which neglect dispersion effects, are significantly smaller than their binding energies.

For the CO_2-TiO_2 complex, k(110)$Ti_7O_{27}H_{27}$-CO_2, Figure 27(c), CO_2 is parallel to the bridging oxygen rows and absorbed with an oxygen over a Ti-5c atom. Our binding configuration 'k' is very similar to one found by Sorescu, Al-Saidi, and Jordan[158], labeled 'II'. For 'k,' our RHF, df-MP2, B3LYP, and PBE binding energies with the AVTZPP (VTZPP) basis are -0.159 (-0.154), -0.457 (-0.406), -0.116 (-0.111), -0.171 (-0.168). Their binding energies, -0.39 for TS-vdw-PBE, and -0.37 using PBE-D, are in line with, but somewhat lower than our df-MP2 values.

For the weakly bound rutile complexes, it is clear that dispersion interactions, not captured with traditional DFT methods, are important for calculating the binding energy, as are basis sets augmented with diffuse functions AVTZPP versus VTZPP.

Looking at the different levels of theory in Table 8 and Table 9, it appears that electron correlation and van der Waals interactions help to stabilize CO_2 on the rutile surface. The df-MP2 binding energies for the Ti_7 clusters are approximately three and a half times greater than the DFT binding energies. Df-MP2 often overestimates dispersion, while DFT neglects it. Because of this we are performed calculations with dispersion corrected DFT, RPA and rPT2 to better represent dispersion and to see how our seven atom cluster model compared with binding energy calculated with slabs and periodic boundary conditions. It is clear that even implementing a large basis set including diffuse functions, that B3LYP and PBE cannot adequately describe the interaction between CO_2 and models of the (110) rutile.

6.3.3 Energy Decomposition Analysis Results

The ALMO-EDA results in Table 10, decompose energetic factors governing the interaction between CO_2 and the TiO_2 clusters. As previously stated, ALMO-EDA divides the interaction energy between CO_2 and the TiO_2 clusters into E_{CT}, E_{FRZ} and E_{POL} components. For E_{CT} it further estimates the direction of charge transfer. The relative values of the binding components E_{CT} , E_{FRZ} and E_{POL}, change depending on the complex. E_{POL} ranges from 61% to 77% of the favorable binding energy and the E_{CT} is approximately 25% to 40%. The linearly bound CO_2 complexes have smaller binding energies as calculated by ALMO-EDA, as with the other methods we used.

Upon decomposing the charge transfer to forward and backwards components, it is interesting to note that for the linearly bound CO_2 complexes, the net charge transfer is from CO_2 to TiO_2. The converse is true with the bent configuration c(101)$Ti_6O_{21}H_{18}CO_2$, as shown in Table 10. The latter, 'c', is the only complex with an appreciable amount of charge transfer (E_{CT} = -5.88 eV) and where electrons move from TiO_2 to CO_2 ($E^{RS}_{TiO_2 \rightarrow CO_2} = -3.331$ eV). This hints at a possible description of an initial binding site and configuration for TiO_2 catalyzed reactions of CO_2. Although charge transfer seems only appreciable with c(101)$Ti_6O_{21}H_{18}CO_2$, for the other clusters its value is comparable to the frozen density and polarization terms; all have some covalent character as expected. For our complexes, the main favorable binding contribution comes from the polarization term, the intra-molecular orbital relaxation. For all of the complexes, it is important to note several things. First, we are not considering the energetic penalty from the geometric distortion, E_{GD}. This would be substantial for complexes such as

c(101)$Ti_6O_{21}H_{18}CO_2$ where CO_2's geometry changes from linear to bent. This, along with the small basis sets used, forces us to interpret the results only as hints to the binding nature.

Table 10 : <u>ALMO-EDA</u>. For Ti we used the LanL2dz ecp and basis. We used the aug-cc-pVTZ for C, O and H atoms in the one and two Ti atom complexes.. We used the aug-cc-pVDZ for C and O atoms associated with the larger clusters and cc-pVDZ basis for the H atoms. As shown by ALMO-EDA, the charge transfer (CT) is significant for cluster c(101), to which CO_2 binds in a bent geometry.

	a(010)	b(001)	c(101)	d(001)	g(010)	i(110)	h(110)	j(110)	k(110)
	$Ti_2O_9H_{10}$	Ti-Wat	Ti_6-5c	$Ti_6O_{21}H16$	Ti_6-5c	$Ti(OH)_4$	Rutile $Ti_7O_{27}H_{27}$		
E_{FRZ}	0.14	0.11	10.35	0.10	0.245	0.04	-0.027	-0.01	0.02
E_{POL}	-0.30	-0.325	-10.28	-0.17	-0.69	-0.14	-0.03	-0.12	-0.14
E_{CT}	-0.09	-0.14	-5.88	-0.11	-0.35	-0.05	0.02	-0.027	-0.05
$E^{RS}_{CO_2 \rightarrow TiO_2}$	-0.06	-0.086	-1.16	-0.048	-0.19	-0.03	-0.004	-0.03	-0.045
$E^{RS}_{TiO_2 \rightarrow CO_2}$	-0.014	-0.023	-3.331	-0.023	-0.054	-0.007	0.004	-0.005	-0.006
E^{HO}_{CT}	-0.018	-0.035	-1.396	-0.032	-0.101	-0.01	0.016	0.006	-0.002
SCF Total	-0.251	-0.357	-5.81	-0.181	-0.801	-0.144	-0.036	-0.036	-0.178

We could only perform the ALMO energy decompositions on systems with an even number of electrons. Therefore we could not explore the TiO_2-CO_2 interaction for the complexes with the bridging oxygen vacancy, e(010)$Ti_6O_{20}H_{18}$-CO_2 and f(010)$Ti_6O_{20}H_{18}$-CO_2. Neither Sorescu's group suing Bader analysis[168] nor Intrakanti's group using NPA and Mullikan analysis found appreciable charge transfer to CO_2 without the presence of surface defects.[2, 17] While we were not able to calculate ALMO-EDA, charge transfer energy for clusters containing an oxygen vacancy, as they had an odd number of orbitals. Our results, in agreement with the above two

studies, show that charge transfer to CO_2 from the cluster can occur when CO_2 is bound in a bent configuration.

6.3.4 Counterpoise Corrections and Semi-Core Electrons

Our results also highlight the importance of counterpoise corrections at the df-MP2 and DFT levels for interactions between CO_2 and TiO_2 clusters. Considering the weak interactions, even using a large basis such as AVTZPP, basis set superposition error, BSSE, is between 31% and 8% of the df-MP2 binding energy for complexes i(110)TiO_4H_4-CO_2, and e(010)$Ti_6O_{20}H_{18}$-Vo-CO_2-bent respectively (Table 11). Complexes d(001)$Ti_6O_{21}H_{18}$-CO_2, a(010)$Ti_2O_9H_{10}CO_2$ and 'b' all have BSSE values that are more than 25% of their $E_{binding(cp)}$ energy. At the df-MP2 level, the BSSE correction switches the energetic order of clusters 'a' and 'b.'

With the rutile complexes, the counterpoise corrections were even more important. We found BSSE to be 45%, 40% and 38% of the counterpoise corrected df-MP2/AVTZPP binding energies for 'j', 'k' and 'h' respectively (Table 12). Using the less complete VTZPP basis, lacking diffuse functions, BSSE is 59% of the df-MP2 binding energy for d(001)$Ti_6O_{21}H_{18}$-CO_2, and 56% for a(010)$Ti_2O_9H_{10}CO_2$. Clusters 'e' and 'c' with the largest binding energy had the smallest BSSE effects, 13% and 25% of the df-MP2 binding energy.

Table 11: Counterpoise corrected binding energies, uncorrected binding energies, BSSE, and BSSE as a percent of the binding energy, for the anatase clusters using df-MP2/AVTZPP and df-MP2/VTZPP combinations of basis sets and pseudopotential.

	DF-MP2/AVTZPP				DF-MP2/VTZPP			
	$E_{binding(cp)}$	$E_{binding}$	BSSE	BSSE as % of $E_{binding}$	$E_{binding(cp)}$	$E_{binding}$	BSSE	BSSE as % of $E_{binding}$
i(110)$Ti(OH)_4$-CO_2	-0.247	-0.325	0.077	31.3	-0.209	-0.302	0.093	44.7
d(001)$Ti_6O_{21}H16$	-0.271	-0.343	0.072	27.4	-0.193	-0.306	0.113	58.8
a(010)$Ti_2O_9H_{10}CO_2$	-0.403	-0.517	0.114	28.4	-0.338	-0.525	0.188	55.6
b(001)Ti-WatCO_2	-0.409	-0.515	0.105	25.8	-0.348	-0.491	0.143	41.2
g(010)Ti_6-5cCO_2	-0.597	-0.697	0.101	16.9	-0.527	-0.677	0.151	28.8
f(010)Ti_6(Vo)-5cCO_2-linear	-0.750	-0.849	0.099	13.1	-0.692	-0.835	0.143	20.7
c(101)Ti_6-5cCO_2	-1.480	-1.705	0.225	15.2	-1.385	-1.731	0.346	25.0
e(010)Ti_6(Vo)-5cCO_2-bent	-2.486	-2.676	0.190	7.6	-2.362	-2.664	0.302	12.8

[a] For clusters a, b, and i, titanium's semi-core 3s and 3p electrons are fully correlated.

As expected when using DFT methods counterpoise corrections are less important but can play a major role for clusters with the smallest binding energies. With d(001)$Ti_6O_{21}H_{18}$-CO_2 using PBE and B3LYP with AVTZPP basis the BSSE is 14% and 24% of the counterpoise corrected binding energy. Counterpoise corrections are important for rutile for example for 'k.' Using PBE with AVTZPP we found BSSE to be 24% of the counterpoise corrected binding energies. Clearly when using DFT methods counterpoise corrections are required for weak interaction energies such as dispersion-dominated binding energies. Given this along with the similar binding energies between various CO_2 configurations on TiO_2 clusters, we consider

counterpoise corrections necessary when reporting the binding energy between CO_2 and TiO_2 models.

We explored the effect of correlating titanium's semi-core 3s and 3p electrons on df-MP2 binding energies for complexes 'b' and 'a'. The inclusion of semicore electrons changed the calculated band structure and gap. Using the AVTZPP basis the binding energy decreased by 6% for 'a' and 9% for 'b,' when correlating the 3s and 3p semi-core electrons on titanium. It appears that correlating the 3s and 3p electrons is not essential, doing so may help differentiate between binding sites of similar energy.

Table 12: Counterpoise corrected binding energies, uncorrected binding energies, BSSE, and BSSE as a percent of the binding energy, for the rutile complexes using df-MP2 with the AVTZPP basis set and pseudopotential

	$E_{binding(cp)}$	$E_{binding}$	BSSE	BSSE as % of $E_{binding}$
h (110) $Ti_7O_{27}H_{27}$ CO_2	-0.153	-0.212	0.059	38.3
j (110) $Ti_7O_{27}H_{27}$ CO_2	-0.368	-0.531	0.164	44.5
k (110) $Ti_7O_{27}H_{27}$ CO_2	-0.457	-0.639	0.182	39.9

[a] All energies are in eV. For clusters k and j, titanium's semi-core 3s and 3p electrons are fully correlated at the df-MP2 level.

6.4 Conclusions

In this work, we have compared different theoretical methods for understanding the interaction of CO_2 with a TiO_2 clusters modeling anatase (001), (010), (101) and rutile (110). We aimed to both further the understanding of this interaction and assess which theoretical methods are best suited for studying the CO_2 on TiO_2 interaction. It is clear that methods capable of including

weak interactions are important for studying CO_2 binding on TiO_2. Standard DFT methods insufficiently describe the binding of CO_2 on TiO_2 surfaces. DFT consistently underestimates the binding energy compared to df-MP2. We found this true even after applying dispersion corrections. Comparing our DFT and df-MP2 binding energies demonstrates that DFT functionals B3LYP and PBE can be quantitatively and qualitatively wrong and that dispersion should be accounted for.

Using ALMO-EDA we found appreciable charge transfer occurs only when CO_2 binds in a bent configuration. CO_2 is more reactive when it binds in a bent configuration. Its LUMO is lowered facilitating the possibility of electron transfer from photo-excited TiO_2 to CO_2. The electron transfer would create the radical $CO_2^{-\bullet}$, priming it for a reaction with H_2O and or O_2. We believe that the (101) stoichiometric and the (010) oxygen deficient anatase surfaces have the greatest potential for photo-exciting CO_2 and catalyzing reactions that remove it from the atmosphere

As a next step, we would like to use a quantum embedding method, to test the viability of different size cluster models and to capture a more complete view of the interaction. Secondly, it is important to further explore the electronic changes that occur when CO_2 binds in a bent geometry to both the (101) and (010) clusters with bridging oxygen vacancies.

6.5 Supplemental Table

Table 13: CO_2 adsorbed geometry on the TiO_2 clusters in Å, and degrees. For the CO_2 binding geometry, r1 and r2 are the distances between the C and the O atoms closer to and farther from the TiO_2 cluster. With the rutile cluster the distances are (O1-Ti, O2-Ti),(C-O, C-O, C-O, C-O), and (C-Ti); and CO_2 is adsorbed horizontally, hence r1 r2

DF-MP2 $E_{binding(cp)}$	r(C-O), r(C-Ti), r(C-Ti)	r(O-Ti)	Adsorbed CO_2 bond lengths and geometry			
			r1	r2	angle	shape
i(110)$Ti(OH)_4$-CO_2		2.64	1.17	1.16	177.90	flat angled
b(001)TiO_5H_6-CO_2		2.40	1.18	1.61	175.10	flat angled
d(001)$Ti_6O_{21}H_{18}$-CO_2		2.57	1.18	1.16	175.50	flat angled
c(101)$Ti_6O_{21}H_{18}$-CO_2	1.36,na,na	1.91	1.34	1.20	128.60	bent
a(010)$Ti_2O_9H_{10}$-CO_2	2.62, na, na	2.51	1.17	1.15	174.40	flat angled
g(010)$Ti_6O_{21}H_{18}$-CO_2	2.40	2.23	1.19	1.15	170.60	slight bend, angled
f(010)$Ti_6O_{20}H_{18}$-CO_2-linear		2.24	1.18	1.16	177.30	flat angled
e(010)$Ti_6O_{20}H_{18}$-CO_2-bent	na,2.18,2.59	1.88, 2.90	1.33	1.21	127.86	bent
h(110)$Ti_7O_{27}H_{26}$-CO2	(4.11,4.11, 4.11, 4.11), 3.95	(4.10,4.12)	1.17	1.17	179.30	flat, parallel
j (110) $Ti_7O_{27}H_{27}$ CO_2		2.79	1.17	1.66	179.77	flat, angled
k (110) $Ti_7O_{27}H_{27}$ CO_2	na, 2.99, 2.98	(2.97, 3.13)	1.17	1.17	178.64	flat, parallel

7. CHAPTER SEVEN: Conclusions

This thesis has focused on testing models and methods for studying the interaction between titanium dioxide and CO2, the structure of the Si(100) surface, and the effect of partial hydrogen passivation on the structure of bare dimers on the Si(100) surface.

For the surface structure of Si(100), my work suggests that methods incorporating both static and dynamic electron correlation effects are required for an accurate description of the surface structure and that small models, containing as few as seven silicon atoms, and two surface dimers, capture the key physics of the surface. CASPT3 works well for small models, while with larger models QMC with a multireference trial wave-function can give good results.

The work on the H2/Si(100) surface suggests that hydrogen bonded to dimers, at coverages as low as $\theta = 1/12$, creates a strain field causing neighboring dimers to reduce their buckling angle.

My work on CO2 interacting with the TiO2 surface demonstrates that it is necessary to use methods including dispersion interactions for accurate characterization of the energetics, and that for the anatase surface CO2 binds significantly more favorably to the (101) surface as compared to the (010), (001) and (110) surfaces.

Bibliography

1. *Working Group I Contribution to the Fifth Assessment Report of the Intergovernmental Panel on Climate Change*; IPCC, 2013.

2. Indrakanti, V. P.; Schobert, H. H.; Kubicki, J. D., Quantum mechanical modeling of CO2 interactions with irradiated stoichiometric and oxygen-deficient anatase TiO2 surfaces: implications for the photocatalytic reduction of CO2. *Energy & Fuels* **2009,** *23* (10), 5247-5256.

3. Hoffmann, R., *Solids and Surfaces: A Chemist's View of Bonding in Extended Structures*. Wiley: 1989.

4. Kittel, C., *Introduction to Solid State Physics*. Wiley: 2004.

5. Wolkow, R. A., Direct observation of an increase in buckled dimers on Si (001) at low temperature. *Physical review letters* **1992,** *68* (17), 2636.

6. Steckel, J.; Jordan, K. D., *Computational Materials Chemistry: Methods and Applications*. Kluwer Academic Publishers: Dordrecht, 2006.

7. Buehler, E. J.; Boland, J. J., Dimer Preparation That Mimics the Transition State for the Adsorption of H2 on the Si (100)-2× 1 Surface. *Science* **2000,** *290* (5491), 506-509.

8. Jung, Y.; Shao, Y.; Gordon, M. S.; Doren, D. J.; Head-Gordon, M., Are both symmetric and buckled dimers on Si(100) minima? Density functional and multireference perturbation theory calculations. *The Journal of chemical physics* **2003,** *119* (20), 10917-10923.

9. Chadi, D. J., ATOMIC AND ELECTRONIC-STRUCTURES OF RECONSTRUCTED SI(100) SURFACES. *Physical Review Letters* **1979,** *43* (1), 43-47.

10. Kim, H.-J.; Tkatchenko, A.; Cho, J.-H.; Scheffler, M., Benzene adsorbed on Si (001): The role of electron correlation and finite temperature. *Physical Review B* **2012,** *85* (4), 041403.

11. Roskop, L.; Gordon, M. S., ORMAS-SCF Study of Silicon (100) Surface Clusters†. *The Journal of Physical Chemistry A* **2010,** *114* (33), 8817-8823.

12. Albrecht, P. M.; Lyding, J. W., Lateral Manipulation of Single-Walled Carbon Nanotubes on H-Passivated Si (100) Surfaces with an Ultrahigh-Vacuum Scanning Tunneling Microscope. *Small* **2007,** *3* (1), 146-152.

13. Lopinski, G.; Wayner, D.; Wolkow, R., Self-directed growth of molecular nanostructures on silicon. *Nature* **2000,** *406* (6791), 48-51.

14. Back, S.; Schmidt, J. A.; Ji, H.; Heo, J.; Shao, Y.; Jung, Y., On the structure of Si (100) surface: Importance of higher order correlations for buckled dimer. *The Journal of chemical physics* **2013,** *138* (20), 204709.

15. Günther, V.; Mauß, F., Si (100) 2× 1 epitaxy: a kinetic Monte Carlo simulation of the surface growth. *Physics Procedia* **2013,** *40*, 56-64.

16. Greenwood, N. N.; Earnshaw, A., *Chemistry of the Elements*. Elsevier Science: 1997.

17. Indrakanti, V. P.; Kubicki, J. D.; Schobert, H. H., Photoinduced activation of CO2 on Ti-based heterogeneous catalysts: Current state, chemical physics-based insights and outlook. *Energy & Environmental Science* **2009,** *2* (7), 745-758.

18. Kurtoglu, M. E.; Longenbach, T.; Gogotsi, Y., Preventing sodium poisoning of photocatalytic TiO2 films on glass by metal doping. *International Journal of Applied Glass Science* **2011,** *2* (2), 108-116.

19. Fujishima, A., Discovery and applications of photocatalysis-Creating a comfortable future by making use of light energy. *Japan Nanonet Bulletin* **2005,** *44*, 1-3.

20. Serpone, N.; Pelizzetti, E., *Photocatalysis: fundamentals and applications*. Wiley New York: 1989.

21. Thompson, T. L.; Diwald, O.; Yates, J. T., CO2 as a Probe for Monitoring the Surface Defects on TiO2 (110) Temperature-Programmed Desorption. *The Journal of Physical Chemistry B* **2003,** *107* (42), 11700-11704.

22. Göpel, W.; Anderson, J.; Frankel, D.; Jaehnig, M.; Phillips, K.; Schäfer, J.; Rocker, G., Surface defects of TiO< sub> 2</sub>(110): A combined XPS, XAES AND ELS study. *Surface science* **1984,** *139* (2), 333-346.

23. Henderson, M. A.; Epling, W. S.; Perkins, C. L.; Peden, C. H. F.; Diebold, U., Interaction of Molecular Oxygen with the Vacuum-Annealed TiO2(110) Surface: Molecular and Dissociative Channels. *The Journal of Physical Chemistry B* **1999,** *103* (25), 5328-5337.

24. Thompson, T. L.; Yates, J. T., Surface science studies of the photoactivation of TiO2 new photochemical processes. *Chemical Reviews* **2006,** *106* (10), 4428-4453.

25. Thompson, T. L. Photocatalysis on Titanium Dioxide Surfaces. Doctoral Dissertation, University of Pittsburgh, 2006.

26. Funk, S.; Burghaus, U., Adsorption of CO2 on oxidized, defected, hydrogen and oxygen covered rutile (1 [times] 1)-TiO2(110). *Physical Chemistry Chemical Physics* **2006,** *8* (41), 4805-4813.

27. Suriye, K.; Jongsomjit, B.; Satayaprasert, C.; Praserthdam, P., Surface defect (Ti3+) controlling in the first step on the anatase TiO2 nanocrystal by using sol–gel technique. *Appl. Surf. Sci.* **2008,** *255* (5, Part 2), 2759-2766.

28. Herman, G. S.; Dohnálek, Z.; Ruzycki, N.; Diebold, U., Experimental Investigation of the Interaction of Water and Methanol with Anatase−TiO2(101). *The Journal of Physical Chemistry B* **2003,** *107* (12), 2788-2795.

29. Tilocca, A.; Selloni, A., Reaction pathway and free energy barrier for defect-induced water dissociation on the (101) surface of TiO2-anatase. *The Journal of chemical physics* **2003,** *119* (14), 7445-7450.

30. Pan, J.; Liu, G.; Lu, G. Q.; Cheng, H.-M., On the True Photoreactivity Order of {001}, {010}, and {101} Facets of Anatase TiO2 Crystals. *Angewandte Chemie International Edition* **2011,** *50* (9), 2133-2137.

31. Linsebigler, A. L.; Lu, G.; Yates Jr, J. T., Photocatalysis on TiO2 surfaces: principles, mechanisms, and selected results. *Chemical reviews* **1995,** *95* (3), 735-758.

32. Leach, A. R., *Molecular Modelling: Principles and Applications*. Prentice Hall: 2001.

33. Kállay, M.; Surján, P. R., Higher excitations in coupled-cluster theory. *The Journal of chemical physics* **2001,** *115* (7), 2945-2954.

34. Füsti-Molnár, L.; Szalay, P. G., New Versions of Approximately Extensive Corrected Multireference Configuration Interaction Methods†. *The Journal of Physical Chemistry* **1996,** *100* (15), 6288-6297.

35. Szalay, P. G., In *Modern Ideas in Coupled-Cluster Methods*, Bartlett, R. J., Ed. World Scientific: Singapore, 1997; pp 81-123.

36. Szalay, P. G.; Bartlett, R. J., Multi-reference averaged quadratic coupled-cluster method: a size-extensive modification of multi-reference CI. *Chemical Physics Letters* **1993,** *214* (5), 481-488.

37. Gdanitz, R. J.; Ahlrichs, R., The averaged coupled-pair functional (ACPF): A size-extensive modification of MR CI(SD). *Chemical Physics Letters* **1988,** *143* (5), 413-420.

38. Møller, C.; Plesset, M. S., Note on an approximation treatment for many-electron systems. *Physical Review* **1934,** *46* (7), 618.

39. Bearpark, M. J.; Ogliaro, F.; Vreven, T.; Boggio-Pasqua, M.; Frisch, M. J.; Larkin, S. M.; Morrison, M.; Robb, M. A., CASSCF calculations for photoinduced processes in large

molecules: Choosing when to use the RASSCF, ONIOM and MMVB approximations. *Journal of Photochemistry and Photobiology A: Chemistry* **2007,** *190* (2–3), 207-227.

40. Finley, J.; Malmqvist, P.-Å.; Roos, B. O.; Serrano-Andrés, L., The multi-state CASPT2 method. *Chemical Physics Letters* **1998,** *288* (2–4), 299-306.

41. Roos, B. O.; Andersson, K.; Fülscher, M. P.; Malmqvist, P.-â.; Serrano-Andrés, L.; Pierloot, K.; Merchán, M., Multiconfigurational Perturbation Theory: Applications in Electronic Spectroscopy. In *Advances in Chemical Physics*, John Wiley & Sons, Inc.: 2007; pp 219-331.

42. Dronskowski, R.; Hoffmann, R., *Computational Chemistry of Solid State Materials: A Guide for Materials Scientists, Chemists, Physicists and others*. Wiley: 2008.

43. Kohn, W. Walter Kohn - Nobel Lecture: Electronic Structure of Matter – Wave Functions and Density Functionals. <http://www.nobelprize.org/nobel_prizes/chemistry/laureates/1998/kohn-lecture.html>

44. VASP Hands-On Sessions. Vienna University.

45. Almbladh, C.-O.; Von Barth, U., Exact results for the charge and spin densities, exchange-correlation potentials, and density-functional eigenvalues. *Physical Review B* **1985,** *31* (6), 3231.

46. Ashcroft, N. W.; Mermin, N. D., *Solid state physics*. Saunders College: 1976.

47. Perdew, J. P.; Burke, K.; Ernzerhof, M., Generalized gradient approximation made simple. *Physical review letters* **1996,** *77* (18), 3865.

48. Becke, A. D., DENSITY-FUNCTIONAL THERMOCHEMISTRY .3. THE ROLE OF EXACT EXCHANGE. *J. Chem. Phys.* **1993,** *98* (7), 5648-5652.

49. Perdew, J. P.; Yue, W., Accurate and simple density functional for the electronic exchange energy: Generalized gradient approximation. *Physical Review B* **1986,** *33* (12), 8800.

50. Perdew, J. P.; Wang, Y., Accurate and simple analytic representation of the electron-gas correlation energy. *Physical Review B* **1992,** *45* (23), 13244.

51. Liao, P.; Carter, E. A., New concepts and modeling strategies to design and evaluate photo-electro-catalysts based on transition metal oxides. *Chemical Society Reviews* **2013,** *42* (6), 2401-2422.

52. Grimme, S., Seemingly simple stereoelectronic effects in alkane isomers and the implications for Kohn–Sham density functional theory. *Angewandte Chemie International Edition* **2006,** *45* (27), 4460-4464.

53. Brittain, D. R.; Lin, C. Y.; Gilbert, A. T.; Izgorodina, E. I.; Gill, P. M.; Coote, M. L., The role of exchange in systematic DFT errors for some organic reactions. *Physical Chemistry Chemical Physics* **2009,** *11* (8), 1138-1142.

54. Leverentz, H. R.; Qi, H. W.; Truhlar, D. G., Assessing the Accuracy of Density Functional and Semiempirical Wave Function Methods for Water Nanoparticles: Comparing Binding and Relative Energies of (H2O) 16 and (H2O) 17 to CCSD (T) Results. *Journal of Chemical Theory and Computation* **2013,** *9* (2), 995-1006.

55. Gerber, I.; Ángyán, J., London dispersion forces by range-separated hybrid density functional with second order perturbational corrections: The case of rare gas complexes. *The Journal of chemical physics* **2007,** *126* (4), 044103.

56. Klimeš, J.; Bowler, D. R.; Michaelides, A., Van der Waals density functionals applied to solids. *Physical Review B* **2011,** *83* (19), 195131.

57. Foulkes, W.; Mitas, L.; Needs, R.; Rajagopal, G., Quantum Monte Carlo simulations of solids. *Reviews of Modern Physics* **2001,** *73* (1), 33.

58. Parrish, R. M., PSI4 Ab Initio Quantum Chemistry. In *DF-MP2: Density-Fitted Second-Order Møller-Plesset Perturbation Theory*.

59. Sherrill, C. D., Density-Fitting Approximations to the Electron Repulsion Integrals. **2010**.

60. Singh, D. J.; Nordstrom, L., *Planewaves, Pseudopotentials, and the LAPW Method*. Springer: 2006.

61. Laasonen, K.; Car, R.; Lee, C.; Vanderbilt, D., Implementation of ultrasoft pseudopotentials in ab initio molecular dynamics. *Physical Review B* **1991,** *43* (8), 6796.

62. Vanderbilt, D., Soft self-consistent pseudopotentials in a generalized eigenvalue formalism. *Physical Review B* **1990,** *41* (11), 7892.

63. Greengard, L.; Rokhlin, V., A fast algorithm for particle simulations. *Journal of Computational Physics* **1987,** *73* (2), 325-348.

64. Grimm, R. C.; Storer, R. G., Monte-Carlo solution of Schrödinger's equation. *Journal of Computational Physics* **1971,** *7* (1), 134-156.

65. Grossman, J. C.; Mitas, L., High accuracy molecular heats of formation and reaction barriers: Essential role of electron correlation. *Physical review letters* **1997,** *79* (22), 4353.

66. Kohn, W.; Sham, L. J., Self-consistent equations including exchange and correlation effects. *Physical Review* **1965,** *140* (4A), A1133.

67. Hohenberg, P.; Kohn, W., Inhomogeneous electron gas. *Physical review* **1964,** *136* (3B), B864.

68. Perdew, J. P.; Chevary, J. A.; Vosko, S. H.; Jackson, K. A.; Pederson, M. R.; Singh, D. J.; Fiolhais, C., ATOMS, MOLECULES, SOLIDS, AND SURFACES - APPLICATIONS OF THE GENERALIZED GRADIENT APPROXIMATION FOR EXCHANGE AND CORRELATION. *Physical Review B* **1992,** *46* (11), 6671-6687.

69. Kresse, G.; Furthmüller, J., Efficient iterative schemes for ab initio total-energy calculations using a plane-wave basis set. *Physical Review B* **1996,** *54* (16), 11169.

70. Kresse, G.; Furthmüller, J., Efficiency of ab-initio total energy calculations for metals and semiconductors using a plane-wave basis set. *Comput. Mater. Sci.* **1996,** *6* (1), 15-50.

71. Kresse, G.; Hafner, J., Ab initio molecular-dynamics simulation of the liquid-metal–amorphous-semiconductor transition in germanium. *Physical Review B* **1994,** *49* (20), 14251.

72. Kresse, G.; Hafner, J., Ab initio molecular dynamics for liquid metals. *Physical Review B* **1993,** *47* (1), 558.

73. Dürr, M.; Hu, Z.; Biedermann, A.; Höfer, U.; Heinz, T., Real-space study of the pathway for dissociative adsorption of H 2 on Si (001). *Physical review letters* **2002,** *88* (4), 046104.

74. Chen, D.; Boland, J. J., Spontaneous roughening of low-coverage Si (100)-2× 1: Cl surfaces: Patch formation on submonolayer halogenated surface. *Physical Review B* **2004,** *70* (20), 205432.

75. Chadi, D., Atomic and electronic structures of reconstructed Si (100) surfaces. *Physical Review Letters* **1979,** *43*, 43-47.

76. Hull, R.; INSPEC, *Properties of Crystalline Silicon*. INSPEC, the Institution of Electrical Engineers: 1999.

77. Dürr, M.; Raschke, M.; Pehlke, E.; Höfer, U., Structure Sensitive Reaction Channels of Molecular Hydrogen on Silicon Surfaces. *Physical review letters* **2001,** *86* (1), 123.

78. Pehlke, E., *Phys. Rev. B* **2000,** *62*.

79. Bratu, P.; Brenig, W.; Gro, A.; Hartmann, M.; Höfer, U.; Kratzer, P.; Russ, R., Reaction dynamics of molecular hydrogen on silicon surfaces. *Physical Review B* **1996,** *54* (8), 5978.

80. Hirao, K., Multireference Møller—Plesset method. *Chemical physics letters* **1992,** *190* (3), 374-380.

81. Aono, M.; Hou, Y.; Oshima, C.; Ishizawa, Y., LOW-ENERGY ION-SCATTERING FROM THE SI(001) SURFACE. *Physical Review Letters* **1982,** *49* (8), 567-570.

82. Bokes, P.; Stich, I.; Mitas, L., Ground-state reconstruction of the Si(001) surface: symmetric versus buckled dimers. *Chemical Physics Letters* **2002,** *362* (5-6), 559-566.

83. Cho, K.; Joannopoulos, J. D., Flipping silicon dimers Si(100) using scanning tip microscopy: A theoretical investigation. *Physical Review B* **1996,** *53* (8), 4553-4556.

84. Dabrowski, J.; Scheffler, M., SELF-CONSISTENT STUDY OF THE ELECTRONIC AND STRUCTURAL-PROPERTIES OF THE CLEAN SI(001)(2X1) SURFACE. *Appl. Surf. Sci.* **1992,** *56-8*, 15-19.

85. Gordon, M. S.; Shoemaker, J. R.; Burggraf, L. W., Response to "Comment on 'An ab initio cluster study of the structure of the Si(001) surface' " J. Chem. Phys. 113, 9353 (2000). *J. Chem. Phys.* **2000,** *113* (20), 9355-9356.

86. Hamers, R. J.; Tromp, R. M.; Demuth, J. E., SCANNING TUNNELING MICROSCOPY OF SI(001). *Physical Review B* **1986,** *34* (8), 5343-5357.

87. Healy, S. B.; Filippi, C.; Kratzer, P.; Penev, E.; Scheffler, M., Role of electronic correlation in the Si(100) reconstruction: A quantum Monte Carlo study. *Physical Review Letters* **2001,** *87* (1), 4.

88. Inoue, K.; Morikawa, Y.; Terakura, K.; Nakayama, M., ORDER-DISORDER PHASE-TRANSITION ON THE SI(001) SURFACE - CRITICAL ROLE OF DIMER DEFECTS. *Physical Review B* **1994,** *49* (20), 14774-14777.

89. Jung, Y. S.; Akinaga, Y.; Jordan, K. D.; Gordon, M. S., An ab initio study of the structure of two-, three- and five-dimer silicon clusters: An approach to the Si(100) surface. *Theor. Chem. Acc.* **2003,** *109* (5), 268-273.

90. Kondo, Y.; Amakusa, T.; Iwatsuki, M.; Tokumoto, H., Phase transition of the Si(001) surface below 100 K. *Surface Science* **2000,** *453* (1–3), L318-L322.

91. Konecny, R.; Doren, D. J., Adsorption of BH3 on Si(100)−(2×1). *The Journal of Physical Chemistry B* **1997,** *101* (51), 10983-10985.

92. Mitsui, T.; Takayanagi, K., Extrinsic structure changes by STM at 65 K on Si(001). *Physical Review B* **2000,** *62* (24), R16251-R16254.

93. Northrup, J. E., ELECTRONIC-STRUCTURE OF SI(100)C(4X2) CALCULATED WITHIN THE GW APPROXIMATION. *Physical Review B* **1993,** *47* (15), 10032-10035.

94. Penev, E.; Kratzer, P.; Scheffler, M., Effect of the cluster size in modeling the H-2 desorption and dissociative adsorption on Si(001). *J. Chem. Phys.* **1999,** *110* (8), 3986-3994.

95. Rohlfing, M.; Krüger, P.; Pollmann, J., Metallic nature of the symmetric dimer model of Si(001)-(2×1). *Physical Review B* **1995,** *52* (19), 13753-13756.

96. Sagisaka, K.; Fujita, D.; Kido, G., Phase manipulation between c(4x2) and p(2x2) on the Si(100) surface at 4.2 K. *Physical Review Letters* **2003,** *91* (14), 4.

97. Schlier, R. E.; Farnsworth, H. E., STRUCTURE AND ADSORPTION CHARACTERISTICS OF CLEAN SURFACES OF GERMANIUM AND SILICON. *J. Chem. Phys.* **1959,** *30* (4), 917-926.

98. Shoemaker, J.; Burggraf, L. W.; Gordon, M. S., An ab initio cluster study of the structure of the Si(001) surface. *J. Chem. Phys.* **2000,** *112* (6), 2994-3005.

99. Stensgaard, I.; Feldman, L. C.; Silverman, P. J., EVIDENCE OF MULTILAYER DISTORTIONS IN THE RECONSTRUCTED SI(001) SURFACE. *Surface Science* **1981,** *102* (1), 1-6.

100. Tromp, R. M.; Smeenk, R. G.; Saris, F. W., ION-BEAM CRYSTALLOGRAPHY AT THE SI(100) SURFACE. *Physical Review Letters* **1981,** *46* (14), 939-942.

101. Uda, T.; Shigekawa, H.; Sugawara, Y.; Mizuno, S.; Tochihara, H.; Yamashita, Y.; Yoshinobu, J.; Nakatsuji, K.; Kawai, H.; Komori, F., Ground state of the Si(001) surface revisited - is seeing believing? *Progress in Surface Science* **2004,** *76* (6-8), 147-162.

102. Yang, C.; Lee, S. Y.; Kang, H. C., An embedded cluster study of dimer buckling on the Si(100) surface. *J. Chem. Phys.* **1997,** *107* (8), 3295-3299.

103. Yokoyama, T.; Takayanagi, K., Anomalous flipping motions of buckled dimers on the Si(001) surface at 5 K. *Physical Review B* **2000,** *61* (8), R5078-R5081.

104. Krishnan, R.; Binkley, J. S.; Seeger, R.; Pople, J. A., SELF-CONSISTENT MOLECULAR-ORBITAL METHODS .20. BASIS SET FOR CORRELATED WAVE-FUNCTIONS. *J. Chem. Phys.* **1980,** *72* (1), 650-654.

105. Schaefer, H. F., *Methods of Electronic Structure Theory*. Plenum Press: 1977.

106. Hirao, K., STATE-SPECIFIC MULTIREFERENCE MOLLER-PLESSET PERTURBATION TREATMENT FOR SINGLET AND TRIPLET EXCITED-STATES, IONIZED STATES AND ELECTRON ATTACHED STATES OF H2O. *Chemical Physics Letters* **1993,** *201* (1-4), 59-66.

107. Steckel, J. A.; Phung, T.; Jordan, K. D.; Nachtigall, P., Concerted use of slab and cluster models in an ab initio study of hydrogen desorption from the Si(100) surface. *J. Phys. Chem. B* **2001,** *105* (18), 4031-4038.

108. Goddard, W. A.; McGill, T. C., STUDY OF SURFACES AND INTERFACES USING QUANTUM-CHEMISTRY TECHNIQUES. *Journal of Vacuum Science & Technology* **1979,** *16* (5), 1308-1317.

109. Hoffmann, R., INTERACTION OF ORBITALS THROUGH SPACE AND THROUGH BONDS. *Accounts Chem. Res.* **1971,** *4* (1), 1-&.

110. Werner, H. J., Third-order multireference perturbation theory - The CASPT3 method. *Mol. Phys.* **1996,** *89* (2), 645-661.

111. Anderson, J. B., RANDOM-WALK SIMULATION OF SCHRODINGER EQUATION - H+3. *J. Chem. Phys.* **1975,** *63* (4), 1499-1503.

112. Purvis III, G. D.; Bartlett, R. J., A full coupled-cluster singles and doubles model: The inclusion of disconnected triples. *The Journal of chemical physics* **1982,** *76* (4), 1910-1918.

113. Pople, J. A.; Headgordon, M.; Raghavachari, K., QUADRATIC CONFIGURATION-INTERACTION - A GENERAL TECHNIQUE FOR DETERMINING ELECTRON CORRELATION ENERGIES. *J. Chem. Phys.* **1987,** *87* (10), 5968-5975.

114. Werner, H. J.; Knowles, P. J., A COMPARISON OF VARIATIONAL AND NONVARIATIONAL INTERNALLY CONTRACTED MULTICONFIGURATION-REFERENCE CONFIGURATION-INTERACTION CALCULATIONS. *Theoret. Chim. Acta* **1990,** *78* (3), 175-187.

115. Kallay, M.; Szalay, P. G.; Surjan, P. R., A general state-selective multireference coupled-cluster algorithm. *J. Chem. Phys.* **2002,** *117* (3), 980-990.

116. Ziesche, P.; Eschrig, H.; Physik, T. U. D. I. f. T.; Society, E. P., *Electronic structure of solids '91: proceedings of the 75. WE-Heraeus-Seminar and 21st Annual International Symposium on Electronic Structure of Solids held in Gaussig (Germany), March 11-15, 1991*. Akademie Verlag: 1991.

117. Becke, A. D., DENSITY-FUNCTIONAL EXCHANGE-ENERGY APPROXIMATION WITH CORRECT ASYMPTOTIC-BEHAVIOR. *Phys. Rev. A* **1988,** *38* (6), 3098-3100.

118. Becke, A. D., Density-functional thermochemistry. III. The role of exact exchange. *The Journal of chemical physics* **1993,** *98* (7), 5648-5652.

119. Lee, C. T.; Yang, W. T.; Parr, R. G., DEVELOPMENT OF THE COLLE-SALVETTI CORRELATION-ENERGY FORMULA INTO A FUNCTIONAL OF THE ELECTRON-DENSITY. *Physical Review B* **1988,** *37* (2), 785-789.

120. Perdew, J. P.; Chevary, J.; Vosko, S.; Jackson, K. A.; Pederson, M. R.; Singh, D.; Fiolhais, C., Erratum: Atoms, molecules, solids, and surfaces: Applications of the generalized gradient approximation for exchange and correlation. *Physical Review B* **1993,** *48* (7), 4978.

121. Trail, J. R.; Needs, R. J., Smooth relativistic Hartree-Fock pseudopotentials for H to Ba and Lu to Hg. *J. Chem. Phys.* **2005,** *122* (17), 10.

122. Trail, J. R.; Needs, R. J., Norm-conserving Hartree-Fock pseudopotentials and their asymptotic behavior. *J. Chem. Phys.* **2005,** *122* (1), 11.

123. Bergner, A.; Dolg, M.; Kuchle, W.; Stoll, H.; Preuss, H., AB-INITIO ENERGY-ADJUSTED PSEUDOPOTENTIALS FOR ELEMENTS OF GROUPS 13-17. *Mol. Phys.* **1993,** *80* (6), 1431-1441.

124. Hehre, W. J.; Ditchfie.R; Pople, J. A., SELF-CONSISTENT MOLECULAR-ORBITAL METHODS .12. FURTHER EXTENSIONS OF GAUSSIAN-TYPE BASIS SETS FOR USE IN MOLECULAR-ORBITAL STUDIES OF ORGANIC-MOLECULES. *J. Chem. Phys.* **1972,** *56* (5), 2257-&.

125. Woon, D. E.; Dunning, T. H., GAUSSIAN-BASIS SETS FOR USE IN CORRELATED MOLECULAR CALCULATIONS .3. THE ATOMS ALUMINUM THROUGH ARGON. *J. Chem. Phys.* **1993,** *98* (2), 1358-1371.

126. Frisch, M. J.; Trucks, G. W.; Schlegel, H. B.; Scuseria, G. E.; Robb, M. A.; Cheeseman, J. R.; Montgomery, J., J. A.; Vreven, T.; Kudin, K. N.; Burant, J. C.; Millam, J. M.; Iyengar, S. S.; Tomasi, J.; Barone, V.; Mennucci, B.; Cossi, M.; Scalmani, G.; Rega, N.; Petersson, G. A.; Nakatsuji, H.; Hada, M.; Ehara, M.; Toyota, K.; Fukuda, R.; Hasegawa, J.; Ishida, M.; Nakajima, T.; Honda, Y.; Kitao, O.; Nakai, H.; Klene, M.; Li, X.; Knox, J. E.; Hratchian, H. P.; Cross, J. B.; Bakken, V.; Adamo, C.; Jaramillo, J.; Gomperts, R.; Stratmann, R. E.; Yazyev, O.; Austin, A. J.; Cammi, R.; Pomelli, C.; Ochterski, J. W.; Ayala, P. Y.; Morokuma, K.; Voth, G. A.; Salvador, P.; Dannenberg, J. J.; Zakrzewski, V. G.; Dapprich, S.; Daniels, A. D.; Strain, M. C.; Farkas, O.; Malick, D. K.; Rabuck, A. D.; Raghavachari, K.; Foresman, J. B.; Ortiz, J. V.; Cui, Q.; Baboul, A. G.; Clifford, S.; Cioslowski, J.; Stefanov, B. B.; Liu, G.; Liashenko, A.; Piskorz, P.; Komaromi, I.; Martin, R. L.; Fox, D. J.; Keith, T.; Al-Laham, M. A.; Peng, C. Y.; Nanayakkara, A.; Challacombe, M.; Gill, P. M. W.; Johnson, B.; Chen, W.; Wong, M. W.; Gonzalez, C.; Pople, J. A. *Gaussian 03*, Revision C.02; Gaussian, Inc: Wallingford CT, 2004.

127. Werner, H. J.; J., K. P.; Lindh, R.; al., e. *MOLPRO a package of ab initio programs*, version 2006.1.

128. Drummond, N. D.; Towler, M. D.; Needs, R. J., Jastrow correlation factor for atoms, molecules, and solids. *Physical Review B* **2004,** *70* (23), 11.

129. Needs, R.; Towler, M.; Drummond, N.; López Ríos, P. *CASINO User Manual*, version 2.1.0; 2008.

130. Yokoyama, T.; Takayanagi, K., Dimer buckling induced by single-dimer vacancies on the Si (001) surface near T c. *Physical Review B* **1997,** *56* (16), 10483.

131. Lampart, W.; Schofield, D.; Christie, R.; Jordan, K. D., Model systems for exploring electron correlation effects in the buckling of SiSi dimers on the Si (100) surface. *Mol. Phys.* **2008,** *106* (12-13), 1697-1702.

132. Kresse, G.; Hafner, J., AB-INITIO MOLECULAR-DYNAMICS FOR OPEN-SHELL TRANSITION-METALS. *Physical Review B* **1993,** *48* (17), 13115-13118.

133. Peterson, K. A., Correlation Consistant Basis Sets for Use with The Dirac-Fock Pseudopotentials of Trail and Needs. Unpublished, 2013.

134. Liu, L.; Zhao, H.; Andino, J. M.; Li, Y., Photocatalytic CO2 Reduction with H2O on TiO2 Nanocrystals: Comparison of Anatase, Rutile, and Brookite Polymorphs and Exploration of Surface Chemistry. *ACS Catalysis* **2012,** *2* (8), 1817-1828.

135. Anpo, M.; Yamashita, H.; Ikeue, K.; Fujii, Y.; Zhang, S. G.; Ichihashi, Y.; Park, D. R.; Suzuki, Y.; Koyano, K.; Tatsumi, T., Photocatalytic reduction of CO2 with H2O on Ti-MCM-41 and Ti-MCM-48 mesoporous zeolite catalysts. *Catalysis Today* **1998,** *44* (1–4), 327-332.

136. Zhang, S. G.; Fujii, Y.; Yamashita, H.; Koyano, K.; Tatsumi, T.; Anpo, M., Photocatalytic Reduction of CO₂ with H₂O on Ti-MCM-41 and Ti-MCM-48 Mesoporous Zeolites at 328 K. *Chemistry Letters* **1997,** *26* (7), 659-660.

137. Rasko, J.; Solymosi, F., Infrared Spectroscopic Study of the Photoinduced Activation of CO2 on TiO2 and Rh/TiO2 Catalysts. *The Journal of Physical Chemistry* **1994,** *98* (29), 7147-7152.

138. Anpo, M.; Yamashita, H.; Ichihashi, Y.; Fujii, Y.; Honda, M., Photocatalytic Reduction of CO2 with H2O on Titanium Oxides Anchored within Micropores of Zeolites: Effects of the Structure of the Active Sites and the Addition of Pt. *The Journal of Physical Chemistry B* **1997,** *101* (14), 2632-2636.

139. Lin, W.; Han, H.; Frei, H., CO2 Splitting by H2O to CO and O2 under UV Light in TiMCM-41 Silicate Sieve. *The Journal of Physical Chemistry B* **2004,** *108* (47), 18269-18273.

140. Inoue, T.; Fujishima, A.; Konishi, S.; Honda, K., Photoelectrocatalytic reduction of carbon dioxide in aqueous suspensions of semiconductor powders. *Nature* **1979,** *277* (5698), 637-638.

141. Werner, H.-J.; Manby, F. R.; Knowles, P. J., Fast linear scaling second-order Møller-Plesset perturbation theory (MP2) using local and density fitting approximations. *The Journal of chemical physics* **2003,** *118* (18), 8149-8160.

142. Over, H.; Wasserfall, J.; Ranke, W.; Ambiatello, C.; Sawitzki, R.; Wolf, D.; Moritz, W., Surface atomic geometry of Si (001)-(2× 1): A low-energy electron-diffraction structure analysis. *Physical Review B* **1997,** *55* (7), 4731.

143. Tkatchenko, A.; Scheffler, M., Accurate molecular van der Waals interactions from ground-state electron density and free-atom reference data. *Physical review letters* **2009,** *102* (7), 073005.

144. Gell-Mann, M.; Brueckner, K. A., Correlation energy of an electron gas at high density. *Physical Review* **1957,** *106* (2), 364.

145. Bohm, D.; Pines, D., A collective description of electron interactions: III. Coulomb interactions in a degenerate electron gas. *Physical Review* **1953,** *92* (3), 609.

146. Ren, X.; Rinke, P.; Scuseria, G. E.; Scheffler, M., Renormalized second-order perturbation theory for the electron correlation energy: Concept, implementation, and benchmarks. *Physical Review B* **2013,** *88* (3), 035120.

147. Khaliullin, R. Z.; Cobar, E. A.; Lochan, R. C.; Bell, A. T.; Head-Gordon, M., Unravelling the Origin of Intermolecular Interactions Using Absolutely Localized Molecular Orbitals. *The Journal of Physical Chemistry A* **2007,** *111* (36), 8753-8765.

148. Falcetta, M.; Jordan, K. D.

149. Werner, H.-J.; Knowles, P. J.; Knizia, G.; Manby, F. R.; Schütz, M., Molpro: a general-purpose quantum chemistry program package. *Wiley Interdisciplinary Reviews: Computational Molecular Science* **2012,** *2* (2), 242-253.

150. Dunning Jr, T. H., Gaussian basis sets for use in correlated molecular calculations. I. The atoms boron through neon and hydrogen. *The Journal of chemical physics* **1989,** *90* (2), 1007-1023.

151. Peterson, K. A.; Woon, D. E.; Dunning Jr, T. H., Benchmark calculations with correlated molecular wave functions. IV. The classical barrier height of the H+ H2→ H2+ H reaction. *The Journal of chemical physics* **1994,** *100* (10), 7410-7415.

152. Boys, S. F.; Bernardi, F. d., The calculation of small molecular interactions by the differences of separate total energies. Some procedures with reduced errors. *Mol. Phys.* **1970,** *19* (4), 553-566.

153. Blum, V.; Gehrke, R.; Hanke, F.; Havu, P.; Havu, V.; Ren, X.; Reuter, K.; Scheffler, M., < i> Ab initio</i> molecular simulations with numeric atom-centered orbitals. *Computer Physics Communications* **2009,** *180* (11), 2175-2196.

154. Toulouse, J.; Gerber, I. C.; Jansen, G.; Savin, A.; Ángyán, J. G., Adiabatic-connection fluctuation-dissipation density-functional theory based on range separation. *Physical review letters* **2009,** *102* (9), 096404.

155. Olsen, T.; Thygesen, K. S., Extending the random-phase approximation for electronic correlation energies: The renormalized adiabatic local density approximation. *Physical Review B* **2012,** *86* (8), 081103.

156. Eshuis, H.; Furche, F., A Parameter-Free Density Functional That Works for Noncovalent Interactions. *The Journal of Physical Chemistry Letters* **2011,** *2* (9), 983-989.

157. Yan, Z.; Perdew, J. P.; Kurth, S., Density functional for short-range correlation: Accuracy of the random-phase approximation for isoelectronic energy changes. *Physical Review B* **2000,** *61* (24), 16430.

158. Sorescu, D. C.; Lee, J.; Al-Saidi, W. A.; Jordan, K. D., CO2 adsorption on TiO2(110) rutile: insight from dispersion-corrected density functional theory calculations and scanning tunneling microscopy experiments. *The Journal of chemical physics* **2011,** *134* (10), 104707.

159. Sorescu, D. C.; Lee, J.; Al-Saidi, W. A.; Jordan, K. D., Coadsorption properties of CO2 and H2O on TiO2 rutile (110): A dispersion-corrected DFT study. *The Journal of chemical physics* **2012,** *137* (7), -.

160. Hirshfeld, F. L., Bonded-atom fragments for describing molecular charge densities. *Theoret. Chim. Acta* **1977,** *44* (2), 129-138.

161. Shao, Y.; Molnar, L. F.; Jung, Y.; Kussmann, J.; Ochsenfeld, C.; Brown, S. T.; Gilbert, A. T. B.; Slipchenko, L. V.; Levchenko, S. V.; O'Neill, D. P.; DiStasio Jr, R. A.; Lochan, R. C.;

Wang, T.; Beran, G. J. O.; Besley, N. A.; Herbert, J. M.; Yeh Lin, C.; Van Voorhis, T.; Hung Chien, S.; Sodt, A.; Steele, R. P.; Rassolov, V. A.; Maslen, P. E.; Korambath, P. P.; Adamson, R. D.; Austin, B.; Baker, J.; Byrd, E. F. C.; Dachsel, H.; Doerksen, R. J.; Dreuw, A.; Dunietz, B. D.; Dutoi, A. D.; Furlani, T. R.; Gwaltney, S. R.; Heyden, A.; Hirata, S.; Hsu, C.-P.; Kedziora, G.; Khalliulin, R. Z.; Klunzinger, P.; Lee, A. M.; Lee, M. S.; Liang, W.; Lotan, I.; Nair, N.; Peters, B.; Proynov, E. I.; Pieniazek, P. A.; Min Rhee, Y.; Ritchie, J.; Rosta, E.; David Sherrill, C.; Simmonett, A. C.; Subotnik, J. E.; Lee Woodcock Iii, H.; Zhang, W.; Bell, A. T.; Chakraborty, A. K.; Chipman, D. M.; Keil, F. J.; Warshel, A.; Hehre, W. J.; Schaefer Iii, H. F.; Kong, J.; Krylov, A. I.; Gill, P. M. W.; Head-Gordon, M., Advances in methods and algorithms in a modern quantum chemistry program package. *Physical Chemistry Chemical Physics* **2006,** *8* (27), 3172-3191.

162. Kong, J.; White, C. A.; Krylov, A. I.; Sherrill, D.; Adamson, R. D.; Furlani, T. R.; Lee, M. S.; Lee, A. M.; Gwaltney, S. R.; Adams, T. R.; Ochsenfeld, C.; Gilbert, A. T. B.; Kedziora, G. S.; Rassolov, V. A.; Maurice, D. R.; Nair, N.; Shao, Y.; Besley, N. A.; Maslen, P. E.; Dombroski, J. P.; Daschel, H.; Zhang, W.; Korambath, P. P.; Baker, J.; Byrd, E. F. C.; Van Voorhis, T.; Oumi, M.; Hirata, S.; Hsu, C.-P.; Ishikawa, N.; Florian, J.; Warshel, A.; Johnson, B. G.; Gill, P. M. W.; Head–Gordon, M.; Pople, J. A., Q-Chem 2.0: a high-performance ab initio electronic structure program package. *Journal of Computational Chemistry* **2000,** *21* (16), 1532-1548.

163. Miller, W. H.; Schaefer, H. F.; Berne, B. J.; Segal, G. A., *Modern Theoretical Chemistry*. Plenum Press: 1976.

164. Hay, P. J.; Wadt, W. R., Ab initio effective core potentials for molecular calculations. Potentials for K to Au including the outermost core orbitals. *The Journal of chemical physics* **1985,** *82* (1), 299-310.

165. Wadt, W. R.; Hay, P. J., Ab initio effective core potentials for molecular calculations. Potentials for main group elements Na to Bi. *The Journal of chemical physics* **1985,** *82* (1), 284-298.

166. Kendall, R. A.; Dunning Jr, T. H.; Harrison, R. J., Electron affinities of the first-row atoms revisited. Systematic basis sets and wave functions. *The Journal of chemical physics* **1992,** *96*, 6796-6806.

167. He, H.; Zapol, P.; Curtiss, L. A., A Theoretical study of CO2 anions on anatase (101) surface. *The Journal of Physical Chemistry C* **2010,** *114* (49), 21474-21481.

168. Sorescu, D. C.; Al-Saidi, W. A.; Jordan, K. D., CO2 adsorption on TiO2(101) anatase: A dispersion-corrected density functional theory study. *The Journal of chemical physics* **2011,** *135* (12), -.

169. Cheng, H.; Selloni, A., Energetics and diffusion of intrinsic surface and subsurface defects on anatase TiO2 (101). *The Journal of chemical physics* **2009,** *131* (5), 054703.

170. Wu, X.; Selloni, A.; Nayak, S. K., First principles study of CO oxidation on TiO2(110): The role of surface oxygen vacancies. *The Journal of chemical physics* **2004,** *120* (9), 4512-4516.